

CRANFIELD UNIVERSITY

ANATOLE VERHAEGEN

**ACTIVE DAMPING OF MISSILE  
BENDING VIBRATIONS**

SCHOOL OF AEROSPACE,  
TRANSPORT AND MANUFACTURING  
MSc Autonomous Vehicle Dynamics and Control

MSc THESIS  
Academic Year 2014 - 2015

Supervisor: Dr R. W. Żbikowski

August 2015



CRAINFIELD UNIVERSITY

SCHOOL OF AEROSPACE, TRANSPORT AND MANUFACTURING  
MSc Autonomous Vehicle Dynamics and Control

MSc THESIS

Academic Year 2014 - 2015

Anatole Verhaegen

ACTIVE DAMPING OF MISSILE BENDING VIBRATIONS

Supervisor: Dr R. Żbikowski

August 2015

This thesis is submitted in partial fulfillment of the  
requirements for the degree of Master of Science.

©Cranfield University 2015. All rights reserved. No part of this publication  
may be reproduced without the written permission of the copyright owner.



# Declaration of Authorship

I, Anatole Verhaegen, declare that this thesis titled, "Active Damping of Missile Bending Vibrations" and the work presented in it are my own. I confirm that:

- This work was done wholly or mainly while in candidature for a degree at this University.
- Where any part of this thesis has previously been submitted for a degree or any other qualification at this University or any other institution, this has been clearly stated.
- Where I have consulted the published work of others, this is always clearly attributed.
- Where I have quoted from the work of others, the source is always given. With the exception of such quotations, this thesis is entirely my own work.
- I have acknowledged all main sources of help.
- Where the thesis is based on work done by myself jointly with others, I have made clear exactly what was done by others and what I have contributed myself.

Signed:

Date:



# Abstract

This master's thesis investigates active structural damping for tactical missiles. The study is based on the case of ASTER 30 - a defense missile - in longitudinal bending. The aim is to replace the structural filter of the autopilot by an active damping loop to reduce the bending oscillations, the seeker noise and the parasitic actuations.

The body of research for active damping is very weak concerning missiles. In this work, a new servo-aeroelastic model is derived based on an hybrid actuated airframe comprising thrust vectoring and fins. The structural model is derived on an original bending Euler Bernoulli beam discretised in the free-free case. The flexible-body modes are extracted and integrated into the longitudinal rigid-body flight dynamics model. A strain gauge, gyroscopes and accelerometers are optimally placed on the airframe with an adapted method. Finally, three active damping and latax controllers are designed with a  $H_\infty$  structured tuning to replace the structural filter. The active damping is performed using the additional sensors and the central fins. The work concludes on the feasibility of active damping based on tracking, actuators demand, vibrations damping, parasitic actuations and stress alleviation.

*Keywords:* servo-aeroelasticity, sensors placement, flexible structures control



# Acknowledgments

This master's thesis was sponsored by MBDA UK. I wish to thank my supervisor Prof. R. W. Żbikowski for his generous advice. I would also like to express my sincere gratitude to Mr G. Wallis for his belief in this work and support. I am indebted to Mr S. Hodgson for providing me precious knowledge. Credit must also be given to Mr J. P. Harcaut and his team for their helpful discussion. Finally I wish to record my appreciation for MBDA UK and MBDA France for giving me the opportunity to work on this inspiring topic.



# Contents

<b>Nomenclature</b>	<b>xiii</b>
<b>List of Figures</b>	<b>xvii</b>
<b>List of Tables</b>	<b>xix</b>
<b>1 Introduction</b>	<b>1</b>
1.1 Motivations for Active Damping . . . . .	1
1.2 Contributions to Knowledge . . . . .	2
1.3 Thesis Structure . . . . .	3
<b>2 Literature Review and Preliminary Study</b>	<b>5</b>
2.1 Literature Review . . . . .	5
2.1.1 Structure Active Damping . . . . .	5
2.1.2 Sensors for Structure Monitoring . . . . .	8
2.1.3 Actuators of ASTER . . . . .	9
2.2 Preliminary Study . . . . .	10
<b>3 Flexible Missile Modeling</b>	<b>15</b>
3.1 Characteristics . . . . .	15
3.2 Flight Dynamics . . . . .	17
3.2.1 Frames . . . . .	17
3.2.2 Mass Properties . . . . .	18
3.2.3 Aerodynamics . . . . .	19
3.2.3.1 Standard Atmosphere . . . . .	19
3.2.3.2 Main Body Aerodynamics . . . . .	19
3.2.3.3 Fins Aerodynamics . . . . .	20
3.2.4 External Efforts . . . . .	20
3.2.4.1 Gravity . . . . .	22
3.2.4.2 Aerodynamic Efforts . . . . .	22
3.2.4.3 Propulsion Efforts . . . . .	22
3.2.5 Equations of Motion . . . . .	22
3.2.5.1 Linear Acceleration . . . . .	23
3.2.5.2 Pitching Moment Equation . . . . .	23

## CONTENTS

---

3.2.6	Trim . . . . .	24
3.2.7	State Space System . . . . .	25
3.2.7.1	State Equation . . . . .	26
3.2.7.2	Output Equation . . . . .	27
3.2.8	Short Period Pitch Oscillations . . . . .	29
3.3	Actuators Dynamics . . . . .	30
3.4	Structural Model . . . . .	30
3.4.1	From continuous to discrete . . . . .	30
3.4.2	Second-Order Structural Model . . . . .	33
3.4.2.1	Nodal Model . . . . .	33
3.4.2.2	Modal Model . . . . .	38
3.4.2.3	Output equation . . . . .	41
3.4.3	Rigid-body Modes Elimination . . . . .	43
3.4.4	State Space Model . . . . .	45
3.4.4.1	From Second-Order Model to State Space Model	45
3.4.4.2	Formulation in State Space Modal Form 2 . . . . .	46
3.4.5	Model Reduction . . . . .	48
3.5	Actuators & Sensors Placement . . . . .	50
3.5.1	Actuators Selection . . . . .	50
3.5.2	Sensors Placement . . . . .	50
3.5.2.1	Placement Indices . . . . .	50
3.5.2.2	Strain Gauges Placement . . . . .	51
3.5.2.3	Gyroscopes Placement . . . . .	52
3.5.2.4	Accelerometers Placement . . . . .	53
3.5.2.5	Outputs Selection . . . . .	55
3.6	Flexible Missile Model . . . . .	55
3.6.1	Structural and Flight Dynamics Interactions . . . . .	56
3.6.2	Servo-aeroelastic Model Inputs and Outputs . . . . .	56
3.6.3	Simulations . . . . .	57
<b>4</b>	<b>Active Damping Autopilots</b>	<b>61</b>
4.1	Missile Control Inputs and Outputs . . . . .	61
4.1.1	Actuators . . . . .	61
4.1.2	Sensors . . . . .	62
4.2	Lateral Acceleration Control . . . . .	62
4.3	Vibrations Alleviation . . . . .	63
4.3.1	Notch Filtering . . . . .	64
4.3.2	Active Structural Damping . . . . .	65
4.3.2.1	Requirements . . . . .	67
4.3.2.2	Strain Feedback . . . . .	68
4.3.2.3	Gyroscope Feedback . . . . .	69
4.3.2.4	Accelerometer Feedback . . . . .	72
4.4	$H_\infty$ Fixed-Structure Tuning . . . . .	74

4.5	Controllers Assessment and Comparison . . . . .	79
4.5.1	Robustness to Uncertainty . . . . .	79
4.5.2	Tracking . . . . .	79
4.5.3	Actuators Demand . . . . .	82
4.5.3.1	Demand for Lateral Acceleration . . . . .	82
4.5.3.2	Parasitic Effects . . . . .	83
4.5.4	Bending Reduction . . . . .	83
4.5.4.1	Vibrations Alleviation . . . . .	84
4.5.4.2	Dynamic Stress Alleviation . . . . .	84
<b>5</b>	<b>Results and Discussions</b>	<b>87</b>
<b>6</b>	<b>Conclusions and Further Developments</b>	<b>91</b>
6.1	Conclusions . . . . .	91
6.2	Further Developments . . . . .	91
<b>A</b>	<b>Software Development - MATLAB</b>	<b>93</b>
A.1	Flexible Missile Modeling . . . . .	93
A.1.1	Servo-aeroelastic Model Generation . . . . .	93
A.1.2	Rigid-body State-space System Generation . . . . .	94
A.1.3	Flexible-body Modeling . . . . .	95
A.2	Control Design . . . . .	96
A.2.1	Controllers Initialisation . . . . .	96
A.2.2	$H_\infty$ Tuning . . . . .	97
	<b>References</b>	<b>99</b>



# Abbreviations

<b>AC</b>	aerodynamic center
<b>AFW</b>	Active Flexible Wing
<b>AoA</b>	angle of attack
<b>CG</b>	center of gravity
<b>DOF</b>	degrees of freedom
<b>IMU</b>	inertial measurement unit
<b>ISA</b>	International Standard Atmosphere
<b>ISS</b>	International Space Station
<b>latax</b>	lateral acceleration
<b>MEMS</b>	micro electromechanical system
<b>MIMO</b>	multiple inputs/multiple outputs
<b>NASA</b>	National Aeronautics and Space Administration
<b>SISO</b>	single input/single output
<b>SPPO</b>	short period pitch oscillation
<b>SS</b>	state-space
<b>TMD</b>	tuned-mass damper
<b>UAV</b>	unmanned aerial vehicle



# Nomenclature

$\alpha$	AoA
$\bar{\lambda}$	deviation of $\lambda$ from $\lambda_0$ ( $\lambda - \lambda_0$ )
$\delta_F$	fins deflection
$\gamma$	flight path
$\lambda_0$	trim value of $\lambda$
$\lambda_i$	value of $\lambda$ at node $i$
$\lambda_m$	modal formulation of $\lambda$
$\lambda_{fb}$	flexible-body component of $\lambda$
$\lambda_{rb}$	rigid-body component of $\lambda$
$\omega$	frequency
$\rho$	air density
$\rho_m$	linear mass density
$\theta$	pitch angle
$\theta_T$	thrust orientation
$\vec{\Omega}_{\mathcal{R}_1/\mathcal{R}_2}$	angular speed velocity of $\mathcal{R}_1$ w.r.t. $\mathcal{R}_2$
$\zeta$	damping ratio
$a_z$	lateral inertial acceleration
$C_D$	drag coefficient
$C_m$	pitching moment coefficient
$C_{D0}$	zero lift drag coefficient

$C_{L0}$	zero AoA lift coefficient
$C_{L\alpha}$	lift coefficient slope
$C_{L\alpha}$	pitching moment coefficient slope
$C_{L\delta F}$	fins lift coefficient slope
$C_L$	lift coefficient
$C_{m0}$	zero AoA pitching moment coefficient
$C_{m\delta F}$	fins pitching moment coefficient slope
$E$	Young modulus
$F_i$	external force along z-axis applied on node $i$
$G$	center of gravity
$g$	standard gravity
$I$	second moment of area
$I_{G,y,i}$ or $I_i$	second moment of area of beam $i$
$J_y$	rotational inertia about y-axis at CG
$k_D$	drag coefficient slope
$L$	missile length
$l$	beam element length
$l$	length of an element beam
$L_{ref}$	reference length (booster diameter)
$m$	mass
$m$	missile mass
$m_i$	mass of node $i$
$M_{y,i}$	external moment along y-axis applied on node $i$
$n$	number of nodes
$q$	pitch rate
$r$	air specific gas constant

$S_{ref}$	reference surface (booster cross-section)
$T$	thrust or temperature
$V$	airspeed
$E$	longitudinal Young modulus of the missile



# List of Figures

1.1	Bending Effects . . . . .	2
2.1	Taipei 101 . . . . .	6
2.2	TMD system of Taipei 101 . . . . .	6
2.3	The International Space Station . . . . .	7
2.4	Active Flutter Suppression on AFW [1] . . . . .	8
2.5	Nanolike Strain Gauge . . . . .	9
2.6	InvenSense IMU . . . . .	10
2.7	PIF concept . . . . .	11
2.8	Two Part Model . . . . .	12
2.9	Bending Link Geometry . . . . .	12
3.1	ASTER 30 Launch . . . . .	16
3.2	Origin of Abscissa Convention . . . . .	17
3.3	Frames Definition . . . . .	18
3.4	Flared Missile Lift and Pitching Moment Coefficients [2] . . . . .	20
3.5	Overview of External Efforts . . . . .	21
3.6	Impulse response of $\frac{\alpha}{\theta_T}(s)$ . . . . .	29
3.7	ASTER 30 Dimensions . . . . .	31
3.8	Lumped Element Model (5 nodes) . . . . .	31
3.9	Computed First Bending Mode Natural Frequency . . . . .	32
3.10	Summary of Structural Parameters for 20 Nodes . . . . .	33
3.11	Elementary Cases for Two Nodes . . . . .	35
3.12	Modes Shape of ASTER 30 . . . . .	39
3.13	Bode plot of $F_1$ to $a_{z,75}$ . . . . .	46
3.14	Hankel Singular Values Decomposition - Strain Gauges Output . .	48
3.15	Hankel Singular Values Decomposition - Gyroscopes Output . .	49
3.16	Hankel Singular Values Decomposition - Accelerometers Output .	49
3.17	Placement Indices - Strain Gages . . . . .	52
3.18	Placements Indices - Gyroscopes . . . . .	53
3.19	Placement Indices - Accelerometers . . . . .	54
3.20	Sensors Locations - Strain gauges $\varepsilon$ , Gyroscopes $q$ and Accelerometers $a_z$ . . . . .	55

## LIST OF FIGURES

---

3.21	Flexible Missile Model	58
3.22	Step ( $1^\circ$ ) Response of $\frac{a_{z83}}{\theta_{Tref}}(s)$ (10 s)	59
3.23	Step ( $1^\circ$ ) Response of $\frac{a_{z83}}{\theta_{Tref}}(s)$ (3 s)	59
4.1	Latax Control Architecture	62
4.2	Root Locus of Pitch Rate Feedback	63
4.3	Root Locus of $\frac{q_{83}}{\theta_{Tref}}$	64
4.4	Bode Diagram of the Notch Filter	65
4.5	Bode Diagram of $\frac{q_{83}(s)}{\theta_{Tref}(s)}$	66
4.6	Closed-Loop with Notch Filter	66
4.7	Bode Diagram of $\frac{\theta_T(s)}{\theta_{Tref}(s)}$	67
4.8	Bode Diagram of $\frac{\delta_F(s)}{\delta_{Fref}(s)}$	68
4.9	Block Diagram of Derivative Strain Feedback	69
4.10	Root Locus of $\frac{\varepsilon_{46}}{\delta_{Fref}}(s)$	70
4.11	Bode of $\frac{q_{83}}{\theta_{Tref}}(s)$ With and Without Strain Feedback	71
4.12	Feedback Architecture with Strain Gages	71
4.13	Root Locus of $\frac{\Delta q}{\delta_{Fref}}(s)$	72
4.14	Bode of $\frac{q_{83}}{\theta_{Tref}}(s)$ With and Without $\Delta q$ Feedback	73
4.15	Feedback Architecture with Gyroscopes	73
4.16	Root Locus of $\frac{1}{s} \frac{\sum a_z}{\delta_{Fref}}(s)$	75
4.17	Bode of $\frac{q_{83}}{\theta_{Tref}}(s)$ With and Without $\sum a_z$ Feedback	76
4.18	Feedback Architecture with Accelerometers	76
4.19	Weighted Form for $H_\infty$ -tuning	77
4.20	Singular Values of $1/W_{err}(s)$	78
4.21	Poles of Closed Loop 1 to 4 Subject to Uncertainty	80
4.22	Step Response of $a_{zref}$ to $(a_{zref} - a_{zCG})$	81
4.23	Sigma Plot of $a_{zref}$ to $(a_{zref} - a_{zCG})$	81
4.24	Singular Values of $a_{zref}$ to $\theta_T$	82
4.25	Singular Values of $a_{zref}$ to $\delta_F$	83
4.26	Singular Values of $\theta_{Tpert}$ to $\theta_T$	84
4.27	Singular Values of $\theta_{Tpert}$ to $a_{z83v}$ (left) and $q_{83v}$ (right)	85
4.28	Singular Values of $\theta_{Tpert}$ to $\varepsilon_{46}$	85
A.1	Calling Tree - Flexible Missile Modeling	94
A.2	Calling Tree - Control Design	96

# List of Tables

2.1	2-rods Model Parameters . . . . .	13
3.1	Mass Properties . . . . .	19
3.2	Aerodynamic Coefficients . . . . .	21
3.3	Flight Parameters . . . . .	24
3.4	Trim Parameters . . . . .	25
3.5	Natural Frequencies and Damping Ratios of Modes . . . . .	40
4.1	$H_\infty$ -tuned Controllers Parameters . . . . .	78
4.2	Parameters Uncertainty . . . . .	79
5.1	Summary of Controllers Performance . . . . .	89



# Chapter 1

## Introduction

### 1.1 Motivations for Active Damping

As aerial threats capabilities improve, countermeasure technology must develop at a faster pace to ensure national safety. This encourages missile manufacturers to design defense missiles with a miss distance always smaller and faster interceptions. New missiles concepts require hypersonic speeds - more thrust and less drag - needing multistage rocket engines and a reduced cross-section. These extremely slender shapes encounter low frequency vibrations created by bending oscillations. The structure and flight dynamics interaction is a source of noise for the seeker and other critical sensors. This noise also propagates through the system and creates parasitic actuations as illustrated on Figure 1.1. These parasitic actuations waste energy and affects stability.

To deal with these issues, structural filters are usually used to remove structural noise from the sensors measurements and to avoid parasitic actuation. However this add a significant phase loss for the control and it curbs the missile fastest dynamics by cutting off high frequency signals. These structural filters do not remove the dynamic structural deformations neither.

Another solution which is not used yet is active damping. With recent sensors and actuators technology enhancement, this technique has become attractive. Sensors industries have made a great step in miniaturisation accompanied with a fast reduction of costs. Micro electromechanical gyroscopes and accelerometers offer a satisfactory accuracy at reduced sizes and affordable prices. Active damping requires several sensors and their intrusiveness must be limited. In the mean time, actuators used to control missiles have now larger bandwidths but are often curbed by structural filters. The extra bandwidth gained by removing the filters could be used to actively damp the structural vibrations. Active damping has also the advantage of directly reducing the bending oscillations which can remove constraints on the airframe structural stiffness.

This thesis investigates how active damping can be conducted on an existing anti-missile missile. The airframe dynamics will be modeled and several sensors

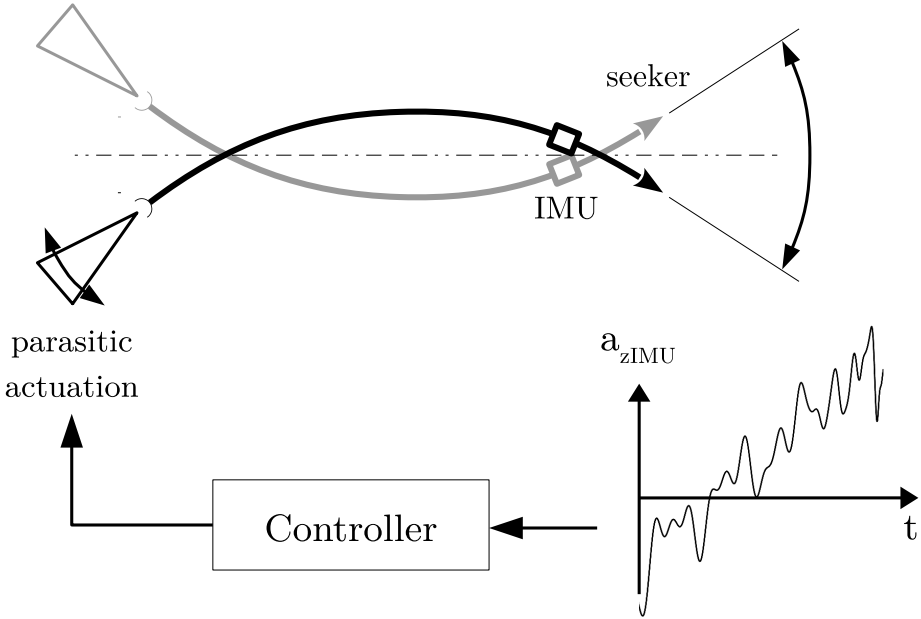


Figure 1.1: Bending Effects

will be placed in order to design and assess active damping controllers.

## 1.2 Contributions to Knowledge

The study contributes to knowledge in active damping on different points listed as follows:

- Elaboration of a servo-aeroelastic model for slender missiles
- discretised Euler-Bernoulli beam dynamics model for the free-free case with variable cross-section
- Multiple sensors placement applied to missiles for bending sensitivity
- Design of three active damping and latax controllers

The servo-aeroelastic model is derived using a linear time invariant longitudinal aerodynamic model having interactions with a dynamic bending beam model of the missile. The flight dynamics consider only the longitudinal short period pitch oscillations (SPPO) mode since other modes like the phugoid have a time scale which belongs to the navigation dynamics. The servo-aeroelastic model can thus be used to simulate lateral acceleration generation with bending oscillations for slender missiles.

The discretised Euler-Bernoulli beam dynamics model is based on the work of [3] and applied to a frame which extremities are free. The bending stiffness and

linear mass density is non uniform along the beam. This structural dynamic model has the advantage of being simple and computationally efficient for bending.

Sensors placement is investigated using the method from [4] and adapted to strain gauges, gyroscopes and accelerometers for the first bending mode. From a set of possible locations for a sensor, the method consists in finding optimal locations to sense the first bending mode state using the  $H_\infty$  norm.

Based on the results of the previous points, three controllers have been designed to both damp bending vibrations and control lateral acceleration in the mean time. These controllers use simple SISO feedbacks with an  $H_\infty$  structured tuning. They are then assessed with several criterion like robustness, tracking, actuators demand and parasitic propagation of vibrations.

### 1.3 Thesis Structure

The thesis is divided in four main Chapters.

Chapter 2 gives an insight to the problem of active damping in structures with a literature survey followed by a preliminary study on a simple 2-part missile model. Chapter 3 explains the modeling process in details to obtain the servo-aeroelastic model which will be used in Chapter 4 where several autopilots are designed and assessed. Chapter 5 summarizes the findings and discuss further the assumptions made and the results obtained. Finally Chapter 6 gives conclusions on the feasibility of active damping for missile systems and presents further studies arising from this thesis.

It is advised to read the first Section of Chapter 3 to understand the missile on which this study is based. However, a reader familiar with flight dynamics can skip the section dealing with them which is detailed and tutorial. The three last Sections of Chapter 3 gives important assumptions on which the model is based. Chapters 4, 5 and 6 mainly deal with the control part of active damping that is the main concern of this study.



# Chapter 2

## Literature Review and Preliminary Study

### 2.1 Literature Review

Active damping of structures involves different fields from flight dynamics, structure dynamics but also sensors and actuators technology for missiles and optimal sensors and actuators placement. A literature survey will be made to give an insight in these domains.

#### 2.1.1 Structure Active Damping

Large structures often present issues with oscillations. The main structural modes have very low damping ratio and the oscillation energy do not dissipate fast enough. In some cases, it is preferable to damp actively these oscillations using actuators instead of passive damping using dampers. Indeed active damping can turn to be light than passive damping and to adapt throughout the structure life whereas passive dampers might be heavy and inefficient if the mass or stiffness of the structure change.

Active damping is encountered in civil engineering for tall skyscrapers. These structures are exceptionally slender and excited by winds and sometimes earthquakes. The elastic and kinetic energy stored must be dissipated with active systems. Civil engineers use tuned mass dampers (TMD) - huge masses mounted on cylinders - to counter oscillations. Kourakis conducts a study on the particular case of Taipei 101 in [5], the fourth tallest tower in the world at the time of writing of this thesis. The mass used is 730 tons and decreases the building oscillations magnitude by 40%. Taipei 101 and its TMD system appear on Figures 2.1 and 2.2.

Large space structures with similar scales have the same issue. On Earth, air in which structures evolve like Taipei 101 is a major actor in damping however in space vacuum, large satellites lattice like the ISS on Figure 2.3 are very lightly

## 2.1. LITERATURE REVIEW

---

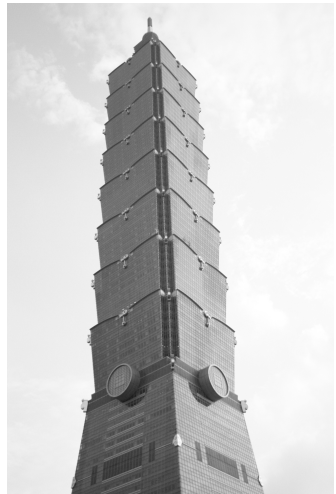


Figure 2.1: Taipei 101

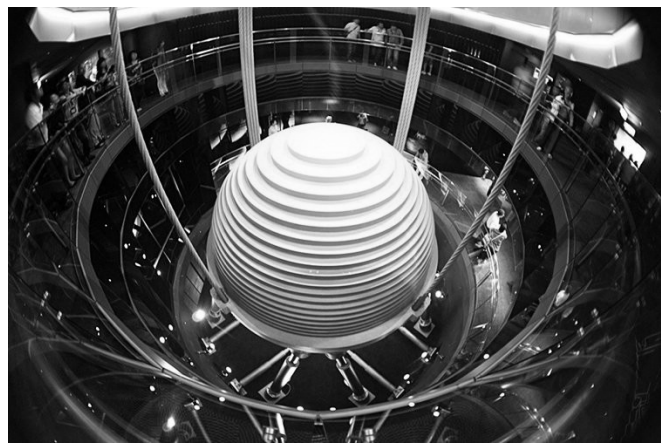


Figure 2.2: TMD system of Taipei 101

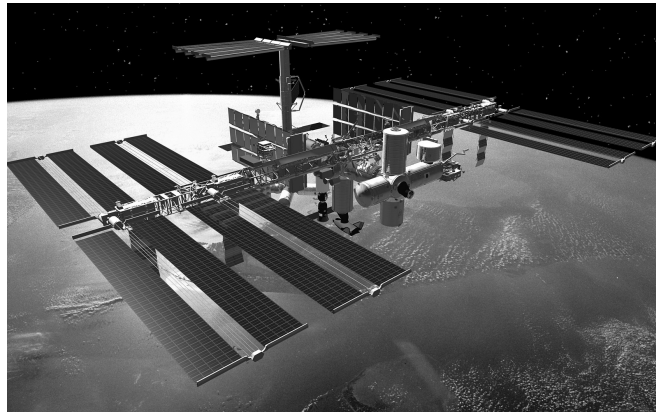


Figure 2.3: The International Space Station

damped. The source of excitation in this case is not the environment but the system itself. The attitude control creates structural deformations and oscillations that must be damped. For such structures, [6] considers the spacecraft attitude control and structural damping as a whole. Indeed structural modes and rigid-body modes are highly coupled and must be controlled in the same MIMO loop. The method consists in establishing a state space model that comprises both rigid-body modes and flexible modes. For smaller systems like defense missiles, the interaction between the structure and the attitude is also probable but at a higher speed.

Active damping for satellites is commonplace because the flexible-body dynamics are slow and thus easy to control but it is a different story for smaller flying structures. Structural dynamic instabilities are encountered by fixed-wing aircrafts at high speeds. This happens when the airflow interacts with the first bending mode and the first twisting mode of the wings. This interaction called flutter is often unstable and leads to the destruction of the airframe. In [1] an active flutter suppression technique is investigated. This study has been published in 1992 and demonstrates the possibility of active damping with a few accelerometers using the trailing edge control surfaces on the Active Flexible Wing at NASA Langley Research Center. The concept is illustrated in Figure 2.4. And allowed the AFW to perform an aggressive roll at a dynamic pressure 10% over flutter dynamic pressure.

This previous study designed two independent controllers, one to generate the roll and another one to suppress flutter. However these controllers might interact and spoil each others performance. In this context, Meirovitch derives a model for a UAV executing time-dependent manoeuvres in [7]. The model is divided in two submodels where the first one is a classical non linear flight dynamics model along a preset trajectory for a conventional aircraft while the second one receiving inputs from the first contains small perturbations from the nominal trajectory in which structural deformations are accounted. This yields a very complex time-varying

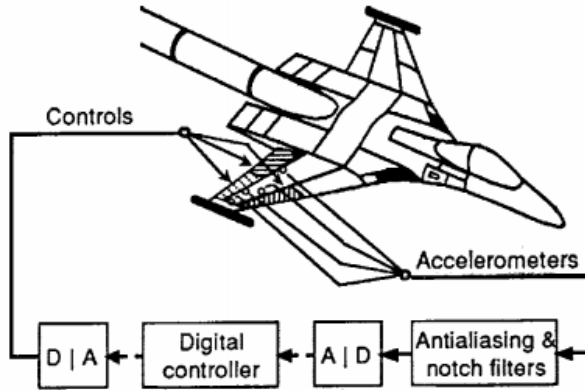


Figure 2.4: Active Flutter Suppression on AFW [1]

model.

[8] gives a complete method to derive an active damping controller from a structural model. This model can be obtained from an FEM model or from an empirical identification process explained in [9]. In [8], active damping controllers are designed on two different examples: a telescope and a flexible airplane. In [10], the issue of bending vibrations for missiles is investigated but Nesline does not design an active damping controller, just a phase and a gain filter to avoid structural instability.

If space structures active damping, building tuned-mass damper and flutter suppression have been thoroughly studied, applications of active damping for missiles or rockets are very limited in the public domain. Manufacturers are used to design airframes very stiff and use a structural filter to remove parasitic actuations due to vibrations. These constraints lead to heavy structures and the controller fastest speed is limited by the structural filter which cuts every high frequency signals off.

### 2.1.2 Sensors for Structure Monitoring

The first step in active damping is sensing the vibrations. Appropriate sensors must be chosen for this function. They should be non intrusive to ease their integration in the airframe and possibly low cost. In this context four types of sensors will be presented: strain gauges, gyroscopes, accelerometers and more recently distributed strain sensors.

Strain gauge is a widespread device to measure local strains on the surface of a structure. This sensor is a long resistor stuck on the surface. When it is stretched or compressed, its electrical resistance changes. This electrical resistance variation is measured using a Wheatstone bridge and gives information on the local strain. With this strain measurement and a reasonably accurate model of the structure,

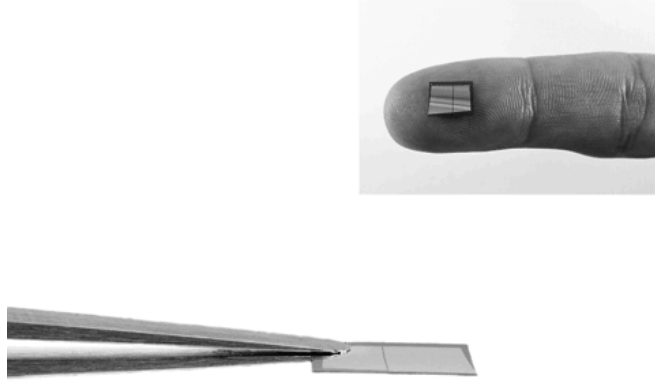


Figure 2.5: Nanolike Strain Gauge

one can infer on the global structure shape. Last generations of these sensors can be very tiny as shown on Figure 2.5. This strain gauge is manufactured by Nanolike using gold nanoparticles. Strain gauges can also be distributed over large areas giving more information on the structure shape as presented in [11].

Gyroscopes and accelerometers are also very widespread and exist under a large variety. In this study, a gyroscope is considered as a sensor give a rotation rate and not an attitude angle. This distinction is important to make when a controller will be derived. The smallest and cheapest gyroscopes and accelerometers use micro electromechanical systems (MEMS). A 6 degrees of freedom (DOF) inertial measurement unit (IMU) can measure rotation rates and inertial accelerations in all 3 axes and is not bigger than a centimetre squared. It consists of 3 chips as shown in Figure 2.6. One is a single axis gyroscope, one is a dual-axis gyroscope and the third one is a 3-axis accelerometer.

To sense the missile bending state, the sensors must be fixed at appropriate locations. The goal is to minimize the signal to noise ratio by placing the sensors where the physical quantity they measure is maximum. [4] describes a method to chose appropriate locations to place the sensors. This method is based on three different norms: the  $H_2$ -norm, the  $H_\infty$ -norm or the Hankel norm. Indices are created for each potential location for all structural modes considered. For each mode, a few locations with the biggest index are selected. Finally, only some of these locations are kept to minimize the correlation between measurements.

### 2.1.3 Actuators of ASTER

ASTER is featured with three types of propulsion mechanisms. During the acceleration phase, the booster controls the trajectory using thrust vectoring. After

## 2.2. PRELIMINARY STUDY

---

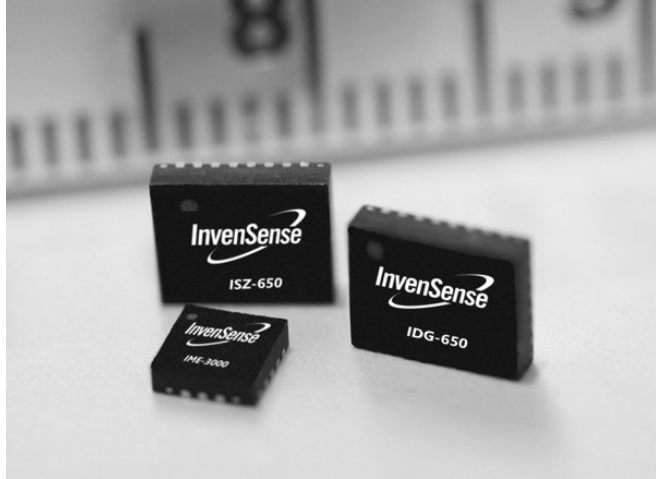


Figure 2.6: InvenSense IMU

the separation, an hybrid system called PIF PAF takes over.

The thrust vectoring is a propulsion and control technique using thrust to accelerate but also to steer. The nozzles from which the flames arise are orientable with cylinders. The deflection of the flames can generate pitching moments, yaw moments and roll moments. [12] gives a summary of advantages and disadvantages of thrust vectoring for all kind of manned aircraft. For missiles flying at 30 km of altitude, thrust vectoring becomes indispensable because the dynamic pressure is too weak for conventional control surfaces. The advantage of thrust vectoring is also the possibility of high angle of attack manoeuvres. The main disadvantages however are the slowness of this actuator, its weight, its complexity and also its inaccuracy in magnitude and orientation. Indeed [13] estimates the thrust misalignment of about 0.25 deg.

The PIF PAF system consists of two control actuators as explained in [14] published in 1984. The PIF part means in French “Pilotage en Force” (forced steering) and consists in a lateral force generator next to the center of gravity. This force is created by impulsions of hot gas as shown in Figure 2.7. This system is very powerful and can generate several dozens of g's. However its accuracy is poor. The aerodynamic flow is fully described in [15]. The attitude correction is done with the PAF system (“Pilotage Aerodynamique Fort” - strong aerodynamic steering) using the fins. [16] explains more precisely the mechanism of PIF-PAF.

## 2.2 Preliminary Study

A preliminary model of a two stage rocket has been derived to understand the mechanisms of interaction between the structure, the aerodynamics and the actuators.

The stages of the rocket are represented by two rigid uniform rods of masses

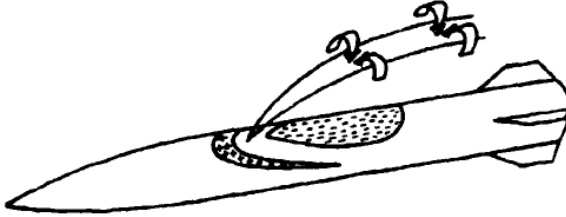


Figure 2.7: PIF concept

$m_1$  and  $m_2$ , of lengths  $l_1$  and  $l_2$  and of rotational inertia at CG  $J_{y1}$  and  $J_{y2}$ . These rods are linked with a torsion spring of stiffness  $k$  determined from a portion of Euler Bernoulli beam. The aerodynamics are considered linear and global thus the rods have the lift coefficients  $C_{L\alpha 1}$  and  $C_{L\alpha 2}$ . The aerodynamic center of each rod is located at their centers of gravity. The model is illustrated in Figure 2.8.

The spring stiffness is calculated using a Euler Bernoulli beam model. The link between the two parts of the missile is assimilated to a pipe of diameter  $0.18\text{ m}$ , of a thickness  $2.5\text{ mm}$  and of length  $l_{link} = 0.5\text{ m}$  giving a second moment of area about the y-axis of  $I = 5.5 \cdot 10^{-6}\text{ m}^4$ . The geometry of this link is illustrated in Figure 2.9. The material is assumed to be carbon fibre of Young modulus  $E = 170\text{ GPa}$ .

For such a part, the bending stiffness is

$$k = \frac{EI}{l_{link}} = 2 \cdot 10^6 \text{ N.m.rad}^{-1}$$

Based on ASTER 30, the parameters chosen are summarized in Table 2.1.

This model has provided information about the amplitude of deformation of the missile. The angles  $\alpha_1$  and  $\alpha_2$  stay very close. The bending deflection is less than a millimeter. This will be useful to make assumptions on the magnitude of deformation and interactions between the aerodynamics and the structure. In particular, it will be assumed that the aerodynamics do not have to take account of the deformation of the missile and the structure is not deformed by aerodynamic forces along the body but only by the lateral forces generated using the thrust vectoring or the fins. This preliminary study of extreme simplicity only accounts for one bending mode. The 2<sup>nd</sup> and 3<sup>rd</sup> bending mode perturbation cannot be seen. The structural model that will be elaborated will consider the missile as a bending beam to encounter higher order modes.

## 2.2. PRELIMINARY STUDY

---

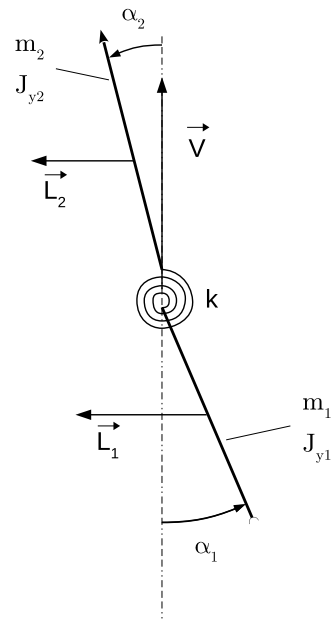


Figure 2.8: Two Part Model

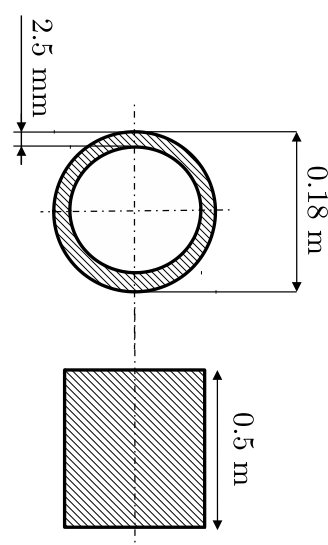


Figure 2.9: Bending Link Geometry

Parameter	Value
$m_1$	$310 \text{ kg}$
$m_2$	$140 \text{ kg}$
$l_1$	$2.2 \text{ m}$
$l_2$	$2.7 \text{ m}$
$J_{y1}$	$375 \text{ kg.m}^2$
$J_{y2}$	$255 \text{ kg.m}^2$
$k$	$2 \cdot 10^6 \text{ N.m.rad}^{-1}$
$C_{L\alpha 1}$	$25 \text{ rad}^{-1}$
$C_{L\alpha 2}$	$6 \text{ rad}^{-1}$

Table 2.1: 2-rods Model Parameters



# Chapter 3

## Flexible Missile Modeling

The Chapter aims at modeling a flexible missile in longitudinal flight. Flight dynamics, structures and actuators and sensors systems will be discussed. These models will eventually be fused to create a servo-aeroelastic model suitable for control design.

### 3.1 Characteristics

ASTER is the name of a family of surface-to-air missiles designed by Eurosam, a consortium between MBDA France, MBDA Italy and Thales Group. The family comprises ASTER 15 for short to medium range and ASTER 30 for short to long range in service since 2001. These missiles are composed of two parts: the booster and the terminal dart. Very shortly after the launch, the missile steer severely with a high angle of attack which create big bending moments as shown on Figure 3.1.

The booster will bring the missile to the final altitude and close to the final speed of Mach 4.5 for ASTER 30, this phase is called the acceleration phase. When the solid propellant of the booster is completely burnt, the two stages separate and the dart will continue its way to the target.

ASTER 30 weights  $450\text{ kg}$  for  $4.9\text{ m}$ . The longitudinal acceleration is about  $15\text{ g}$ . It can reach an altitude of  $30\text{ km}$  and fly to up to Mach 4.5.

These missiles can generate lateral forces with two elements. The first being the thrust vectoring at the tail. Two nozzles are actuated with hydraulic cylinders and can orientate the thrust to generate pitching and yawing moments. The second element are fins at the tail of the dart. Although these control surfaces are generally not used during the acceleration phase, they will be considered in this thesis for active damping purposes. The deflection of the fins can create a lateral force or a rolling moment. They also create little pitching and yawing moments because of their distance from the centre of gravity.

The defense missile is equipped with several sensors for tracking and control.

### 3.1. CHARACTERISTICS

---



Figure 3.1: ASTER 30 Launch

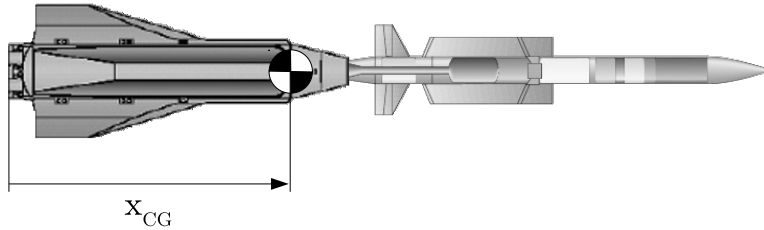


Figure 3.2: Origin of Abscissa Convention

In particular it has a seeker in the nose and is featured with accelerometers and gyroimeters not far from the nose.

ASTER 30 is exceptionally slender and subject to bending. The link that binds the booster and the dart is thus very stiff and complex in order to maintain the two parts together under extreme bending moments. The vibrations due to its slenderness are a major source of noise for the seeker and for the inertial measurement unit.

## 3.2 Flight Dynamics

A flight dynamic model of ASTER 30 will be established. After defining the sign and frames conventions, the mass properties and aerodynamics will be estimated with limited information available in the public domain. Finally the equations of motion will be derived adapted from [17]. This part is particularly detailed to show all the conventions chosen.

### 3.2.1 Frames

First of all, a location of a point on the airframe will be defined with its abscissa  $x$ . The convention chosen for the origin of abscissa is the tail and positive forward. This convention is illustrated on Figure 3.2 for the center of gravity.

There are four frames to define. They all have the axis  $\vec{y}_0 = \vec{y}$  in common because the dynamics considered are only in the xz-plane.

The first one is the Earth's frame  $(\vec{z}_0, \vec{x}_0)$  where  $\vec{z}_0$  is vertical and oriented downward.  $\vec{x}_0$  is oriented forward.

The second one is the aerodynamic frame  $(\vec{z}_a, \vec{x}_a)$  with  $\vec{x}_a$  along the speed vector of the missile and  $\vec{z}_a$  normal to  $\vec{x}_a$  and oriented downward. The flight path frame is obtained by rotating the Earth's frame of an angle of  $\gamma$  the flight path angle around  $\vec{y}$ .

The third one is the body frame  $(\vec{z}_b, \vec{x}_b)$  where  $\vec{x}_b$  is along the body axis and  $\vec{z}_b$  normal to  $\vec{x}_b$  and oriented downward. The body frame is obtained by rotating the aerodynamic frame of an angle of  $\alpha$  the angle of attack around  $\vec{y}$ . The pitch angle is  $\theta = \alpha + \gamma$ .

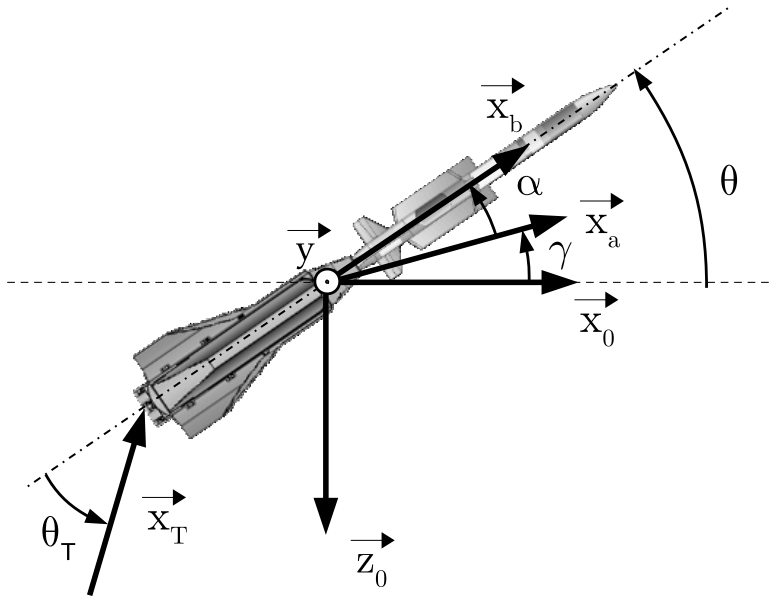


Figure 3.3: Frames Definition

The last one is the propulsion frame  $(\vec{x}_T, \vec{z}_T)$  where  $\vec{x}_T$  is along the thrust vector and  $\vec{z}_T$  is normal to it and oriented downward. This last frame is obtained by rotating the body frame by an angle of  $\theta_T$  - the nozzle angle - around  $\vec{y}$ .

These frames are summarized in Figure 3.3.

### 3.2.2 Mass Properties

ASTER 30 has two parts. The booster weights  $m_{booster} = 310 \text{ kg}$  and will lose mass along the acceleration phase. However, its mass is considered as constant and equal to  $310 \text{ kg}$  to simplify the model. The dart weights  $m_{dart} = 140 \text{ kg}$  during the complete flight. The total mass of the missile is then  $m = 450 \text{ kg}$ . The mass linear density is assumed to be uniform in the booster and in the dart. The length of the booster is  $L_{booster} = 2.2 \text{ m}$  and the dart is lightly longer with  $L_{dart} = 2.7 \text{ m}$

The center of gravity ( $CG$ ) position is at  $x_{CG} = \frac{\int x dm}{m}$ . With uniform mass distribution,

$$x_{CG} = \frac{\frac{1}{2} L_{booster} m_{booster} + (L_{booster} + \frac{1}{2} L_{dart}) m_{dart}}{m}$$

that yields  $x_{CG} = 1.86 \text{ m}$ .

Parameter	Value
Total mass $m$	450 kg
Rotational Inertia $J_y$	789 kg.m <sup>2</sup>
Total length $L$	4.9 m
CG position $x_{CG}$	1.86 m

Table 3.1: Mass Properties

The rotational inertia at the center of gravity and about the y-axis is  $J_y = \int(x - x_{CG})^2 dm$  giving

$$J_y = \frac{1}{3} \frac{m_{booster}}{L_{booster}} [(L_{booster} - x_{CG})^3 + x_{CG}^3] + \frac{1}{3} \frac{m_{dart}}{L_{dart}} [(L_{dart} + L_{booster} - x_{CG})^3 - (L_{booster} - x_{CG})^3]$$

Finally  $J_y = 789 \text{ kg.m}^2$ . All mass properties are summarized in Table 3.1.

### 3.2.3 Aerodynamics

An aerodynamic model is needed to derive the equations of motion. Slender bodies aerodynamics are usually highly non linear but this model will be considered as linear for simplicity and will be valid only for little angle of attacks. The atmosphere and the variation of air density will first be defined, then the main body aerodynamics will be described ending with the fins aerodynamics.

#### 3.2.3.1 Standard Atmosphere

For the atmosphere model, the International Standard Atmosphere is considered. We consider the missile flying at sea level. Thus the air density is  $\rho = 1.21 \text{ kg.m}^{-3}$  and the temperature is  $T = 15^\circ\text{C} = 298.15 \text{ K}$ .

#### 3.2.3.2 Main Body Aerodynamics

The reference surface for this type of airframe is the cross-section of the missile. The biggest cross-section is located at the booster and will be taken as reference surface. Thus  $S_{ref} = \pi D_{booster}^2 / 4$ . The length reference will be the largest diameter  $L_{ref} = D_{booster}$ .

ASTER 30 has a body which is very similar to the flared frame studied in [2]. Some of its aerodynamic data are in Figure 3.4. In this figure, the x-axis is oriented from nose to tail contrary to this thesis.

The lift coefficient slope in this paper is  $C_{L\alpha} = 22 \text{ rad}^{-1}$ . Since the airframe is symmetric about its xy-plane,  $C_{L0} = 0 \text{ rad}^{-1}$ . Similarly, the zero angle of attack pitching moment coefficient  $C_{m0} = 0 \text{ rad}^{-1}$ . In [2], the pitching moment

### 3.2. FLIGHT DYNAMICS

---

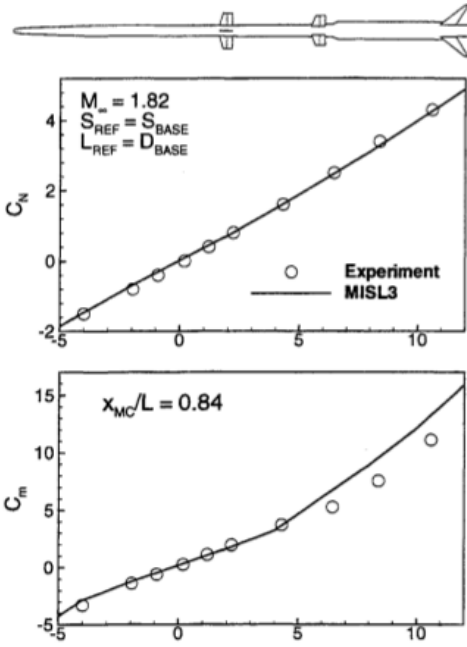


Figure 3.4: Flared Missile Lift and Pitching Moment Coefficients [2]

coefficient slope is  $C_{m\alpha} = 45 \text{ rad}^{-1}$  at  $x_{CM} = 0.78 \text{ m}$ . This coefficient places the aerodynamic center at  $x_{AC} = \frac{L_{ref}C_{m\alpha}}{C_{L\alpha}} + x_{CM} = 1.52 \text{ m}$ . The aerodynamic center in this paper is too fore compared to the center of gravity at  $x_{CG} = 1.86 \text{ m}$  for a thrust vectoring missile. Indeed the accuracy of about  $\pm 0.25^\circ$  of the thrust orientation is too poor. The aerodynamic center will be placed 80 cm aft of the center of gravity at  $x_{AC} = 1.06 \text{ m}$ . This yields a pitching moment coefficient slope of  $C_{m\alpha} = -49 \text{ rad}^{-1}$  **at the center of gravity**.

The drag coefficient for such a missile is given in [18]. The zero-lift drag is  $C_{D0} = 0.95$  and the drag slope is estimated to be  $k_D = 1$ .

#### 3.2.3.3 Fins Aerodynamics

The fins aerodynamic center is located at  $x_F = 2.50 \text{ m}$ . The lift coefficient slope at Mach 2 is estimated to be  $C_{L\delta_F} = 3.1 \text{ rad}^{-1}$ . The pitching moment coefficient slope is  $C_{m\delta_F} = 5.49 \text{ rad}^{-1}$ .

All the aerodynamic coefficients are summarized in Table 3.2.

#### 3.2.4 External Efforts

Several external efforts act on the missile airframe. These forces are due to gravity, aerodynamics and propulsion. Figure 3.5 gives an overview of all external efforts applied on the airframe.

Parameter	Value
Aerodynamic Center $x_{AC}$	1.06 m
Body Lift Coefficient Slope $C_{L\alpha}$	22 rad <sup>-1</sup>
Fins Lift Coefficient Slope $C_{L\delta_F}$	3.1 rad <sup>-1</sup>
Zero Angle of Attack Lift Coefficient $C_{L0}$	0 rad <sup>-1</sup>
Pitching Moment Coefficient Slope at CG $C_{m\alpha}$	-49 rad <sup>-1</sup>
Fins Pitching Moment Coefficient at CG $C_{m\delta_F}$	5.49 rad <sup>-1</sup>
Zero Angle of Attack Pitching Moment Coefficient at CG $C_{m0}$	0 rad <sup>-1</sup>

Table 3.2: Aerodynamic Coefficients

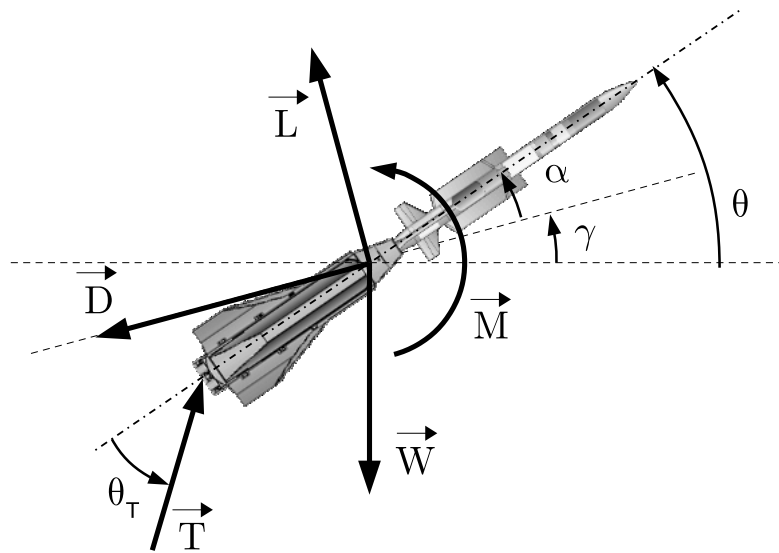


Figure 3.5: Overview of External Efforts

### 3.2.4.1 Gravity

The gravity is assumed to be uniform all along the flight trajectory and equal to the standard gravity value  $g = 9.81 \text{ m.s}^{-2}$ . The weight is denoted  $\vec{W}$ , it acts at  $x_{CG}$  and is oriented downward along  $\vec{z}_0$ :

$$\vec{W} = m g \vec{z}_0$$

### 3.2.4.2 Aerodynamic Efforts

The aerodynamic efforts can be divided into a lift force, a drag force and a pitching moment. The pitching moment is calculated at the center of gravity.

**Lift** The lift is acting normal to the flight path along  $\vec{z}_a$  of amplitude  $L$ :

$$L = \frac{1}{2} \rho S_{ref} V^2 C_L$$

where  $C_L = C_{L0} + C_{L\alpha}\alpha + C_{L\delta_F}\delta_F$ .

**Drag** The drag is acting along the flight path  $\vec{x}_a$  and oriented opposite to the speed vector and of amplitude  $D$ .

$$D = \frac{1}{2} \rho S_{ref} V^2 C_D$$

with  $C_D = C_{D0} + k_D C_L^2$ .

**Pitching Moment** The pitching moment at the center of gravity is acting along the y-axis with an amplitude of  $M$ :

$$M = \frac{1}{2} \rho S_{ref} V^2 D_{ref} C_m$$

with  $C_m = C_{m0} + C_{m\alpha}\alpha + C_{m\delta_F}\delta_F$ .

### 3.2.4.3 Propulsion Efforts

The thrust is oriented along  $\vec{x}_T$  thanks to the orientable nozzle. The propulsion force is then

$$\vec{T} = T \vec{x}_T$$

## 3.2.5 Equations of Motion

The Equations of Motion are projected in the aerodynamic frame  $(\vec{z}_a, \vec{x}_a, \vec{y})$ . This gives three equations: the propulsion equation, the lift equation and the pitching moment equation.

### 3.2.5.1 Linear Acceleration

The linear acceleration of the center of gravity in an inertial frame of reference  $\mathcal{R}_e$  is linked to the sum of external forces by the mass of the airframe:

$$m \vec{a}_{CG/\mathcal{R}_e} = \sum \vec{F}_{external} \quad (3.1)$$

The acceleration in  $\mathcal{R}_e$  is

$$\vec{a}_{CG/\mathcal{R}_e} = \left[ \frac{d\vec{V}}{dt} \right]_{\mathcal{R}_e}$$

The speed vector  $\vec{V}$  must be differentiated in the aerodynamic frame which is not an inertial frame of reference to link the acceleration with the aerodynamic parameters. The vector  $\vec{V}$  differentiated in the moving frame  $\mathcal{R}_a$  relative to the frame  $\mathcal{R}_e$  follows the following formula:

$$\left[ \frac{d\vec{V}}{dt} \right]_{\mathcal{R}_e} = \left[ \frac{d\vec{V}}{dt} \right]_{\mathcal{R}_a} + \vec{\Omega}_{\mathcal{R}_a/\mathcal{R}_e} \wedge \vec{V}$$

thus

$$\left[ \frac{d\vec{V}}{dt} \right]_{\mathcal{R}_e} = \dot{V} \vec{x}_a - \dot{\gamma} V \vec{z}_a$$

Equation 3.1 is then projected in the aerodynamic frame  $(\vec{z}_a, \vec{x}_a)$ :

$$\begin{cases} m \dot{V} &= \sum \vec{F}_{external} \cdot \vec{x}_a \\ -m V \dot{\gamma} &= \sum \vec{F}_{external} \cdot \vec{z}_a \end{cases}$$

Finally, developing the sum of forces the first equation gives the propulsion equation:

$$m \dot{V} = -D + T \cos(\theta_T + \alpha) - W \sin(\gamma) \quad (3.2)$$

The second equation gives the lift equation:

$$-m V \dot{\gamma} = -L - T \sin(\theta_T + \alpha) + W \cos(\gamma) \quad (3.3)$$

### 3.2.5.2 Pitching Moment Equation

The pitching moment equation at the center of gravity along the y-axis is

$$J_y \dot{q} = \sum \vec{M}_{external}$$

Thus developing the pitching moment yields

### 3.2. FLIGHT DYNAMICS

---

Parameter	Value
Altitude	0 ft
Speed	680 m.s <sup>-1</sup> (Mach 2)
Temperature	298.15 K
Air Density	1.21 kg.m <sup>-3</sup>

Table 3.3: Flight Parameters

$$J_y \dot{q} = M - T \sin(\theta_T) x_{CG} \quad (3.4)$$

#### 3.2.6 Trim

At the trim state, the altitude is constant so  $\gamma = \gamma_0 = 0 \text{ rad}$ .

The speed of the missile is chosen to be Mach 2 at sea level and standard temperature, hence  $V = V_0 = Ma$ . The speed of sound is

$$a = \sqrt{\gamma r T} = \sqrt{1.4 \cdot 287 \cdot (273.15 + 15)} = 340 \text{ m.s}^{-1}$$

Thus  $V_0 = 680 \text{ m.s}^{-1}$  ( $= 1322 \text{ kts}$ ).

The acceleration of the missile is said to be about 15g which corresponds to  $\dot{V}_0 = 147 \text{ m.s}^{-2}$ .

The other derivatives  $\dot{\gamma}_0$ ,  $\dot{q}_0$ ,  $\dot{q}_0$  are zero.

Using the relation  $\theta = \alpha + \gamma$ , the only unknowns at trim state in the Equations 3.2, 3.3 and 3.4 are  $\alpha_0$ ,  $T_0$  and  $\theta_{T0}$ . Solving this system of equation gives the following result:

$$\begin{cases} \alpha_0 &= 37 \cdot 10^{-3} \text{ rad} = 2.1^\circ \\ T_0 &= 72.2 \text{ kN} \\ \theta_{T0} &= -18 \cdot 10^{-3} \text{ rad} = -1.0^\circ \end{cases}$$

At this trim state, the lift is only  $L = 3.0 \text{ kN}$  and the weight of the missile is  $W = 4.4 \text{ kN}$  thus thrust vertical component accounts for one third of the lifting forces. Thrust vertical component is  $T_0 \sin(\theta_{T0} + \alpha_0) = 1.4 \text{ kN}$ . The drag is only  $D = 11.6 \text{ kN}$  which corresponds to 16% of the thrust. The majority of the thrust is generated to accelerate. This gives an insight on the efforts magnitude applied on the airframe.

The flight parameters and the trim state is summarized in Tables 3.3 and 3.4.

Parameter	Value
Thrust $T_0$	72.2 kN
Thrust orientation $\theta_{T0}$	$-1.0^\circ$
Angle of attack $\alpha_0$	$2.1^\circ$
Flight path $\gamma_0$	$0^\circ$

Table 3.4: Trim Parameters

### 3.2.7 State Space System

The state vector considered for the state-space model is

$$x = \begin{bmatrix} \bar{\alpha} \\ q \end{bmatrix}$$

where  $q$  is the pitch rate and  $\bar{\alpha}$  is the deviation of  $\alpha$  from the trim value  $\alpha_0$ :

$$\bar{\alpha} = \alpha - \alpha_0$$

The state vector is only of dimension 2 because  $\gamma$ ,  $\dot{\gamma}$ ,  $V$  or  $\rho$  are navigation variables and have very slow dynamics. Indeed this study is interested about lateral acceleration generation, which happens faster.

The input vector here is  $u = \begin{bmatrix} \bar{\theta}_T \\ \delta_F \end{bmatrix}$  where  $\bar{\theta}_T$  is the deviation of  $\theta_T$  from  $\theta_{T0}$

and  $\delta_F$  is the fins deflection.

The output vector is

$$y = \begin{bmatrix} q \\ a_{zaCG} \\ a_{zb10}^- \\ a_{zb54}^- \\ a_{zb83}^- \\ a_{zb92}^- \end{bmatrix}$$

where  $a_{zaCG}$  is the inertial acceleration normal to the speed vector at the center of gravity,  $a_{zb^i}$  is the inertial acceleration normal to the body at  $x = \frac{i-1}{99}L$ . This notation will make more sense when nodes will be defined in Section 3.4 on page 30.  $a_{zb^i}^-$  is the deviation of  $a_{zb^i}$  from the trim value  $a_{zb^{i0}}$ . Indeed,  $a_{zb^{i0}}$  is not zero. The missile is in constant acceleration at about  $15g$  and has a trim angle of attack of

## 3.2. FLIGHT DYNAMICS

---

$\alpha_0 = 37 \cdot 10^{-3} \text{ rad}$ , thus  $a_{z_b i 0} = 15 \cdot 0.037 = 0.55 g$ . Moreover  $a_{z_b i}$  will vary with a change in angle of attack because of the forward acceleration projected normally to the body. The missile inboard computer is able to subtract this component on the lateral acceleration. Signal processing is not the purpose of this study thus it will be assumed that  $a_{z_b i}^- = a_{z_a i}$ . This means that an accelerometer fixed on the body is assumed to measure the inertial acceleration normal to the speed vector.  $a_{z_a i}$  will now be simply denoted  $a_{z_i}$ . Thus

$$y = \begin{bmatrix} q \\ a_{zCG} \\ a_{z10} \\ a_{z54} \\ a_{z83} \\ a_{z92} \end{bmatrix}$$

The pitch rate  $q$  and acceleration  $a_{z83}$  are measured to control the rigid-body states of the missile. These measurements are already integrated in the current version of ASTER 30. The acceleration measurements at nodes 10, 54 and 92 will be used to measure the vibrations due to bending oscillations. The vibration components of these accelerations will be added later. The lateral acceleration of the center of gravity is an output to assess the system. Indeed, the controller will make this output equal to the reference acceleration.

### 3.2.7.1 State Equation

The two equations that governs the dynamic of this state-space system are Equations 3.3 and 3.4. Equation 3.3 can be rearrange using  $\dot{\gamma} = q - \dot{\alpha}$  to give

$$\dot{\alpha} = \frac{1}{mV} \left( -\frac{1}{2} \rho S_{ref} V^2 (C_{L0} + C_{L\alpha} \alpha + C_{L\delta_F} \delta_F) - T \sin(\theta_T + \alpha) + W \cos(\gamma) \right) + q \quad (3.5)$$

Equation 3.4 yields

$$\dot{q} = \frac{1}{J_y} \left( \frac{1}{2} \rho S_{ref} V^2 L_{ref} (C_{m0} + C_{m\alpha} \alpha + C_{m\delta_F} \delta_F) - T \sin(\theta_T) x_{CG} \right) \quad (3.6)$$

The linearization of the two last Equations 3.5 and 3.6 about the trim state where  $[\alpha, V, \rho, \theta_T, T, \gamma] = [\alpha_0, V_0, \rho_0, \theta_{T0}, T_0, \gamma_0]$ . This brings the following matrix equation:

$$\begin{bmatrix} \dot{\bar{\alpha}} \\ \dot{q} \end{bmatrix} = A \begin{bmatrix} \bar{\alpha} \\ q \end{bmatrix} + B \begin{bmatrix} \theta_T^- \\ \delta_F \end{bmatrix}$$

where

$$A = \begin{bmatrix} A_{11} & A_{12} \\ A_{21} & A_{22} \end{bmatrix}$$

$$\begin{cases} A_{11} = -\frac{1}{mV_0} \left( \frac{1}{2} \rho_0 S_{ref} V_0^2 C_{L\alpha} + T_0 \cos(\theta_{T0} + \alpha_0) \right) \\ A_{12} = 1 \\ A_{21} = \frac{1}{J_y} \frac{1}{2} \rho_0 S_{ref} V_0^2 L_{ref} C_{m\alpha} \\ A_{22} = 0 \end{cases}$$

and

$$B = \begin{bmatrix} -\frac{T_0 \cos(\theta_{T0} + \alpha_0)}{mV_0} & -\frac{\rho_0 S_{ref} V_0 C_{L\delta_F}}{2m} \\ -\frac{T_0 \cos(\theta_{T0}) x_{CG}}{J_y} & \frac{\rho_0 S_{ref} V_0^2 L_{ref} C_{m\delta_F}}{2J_y} \end{bmatrix}$$

A numerical computation gives the following results:

$$A = \begin{bmatrix} -0.501 & 1 \\ -82.5 & 0 \end{bmatrix}, \quad B = \begin{bmatrix} -0.236 & -0.0374 \\ -170 & 9.26 \end{bmatrix}$$

### 3.2.7.2 Output Equation

The pitch rate  $q$  is already a state so adding this signal to the output is done easily.

The inertial acceleration  $a_{zCG}$  is normal to the speed vector and has been derived in Subsection 3.2.5.1 on page 23:

$$a_{zCG} = \frac{1}{m} (-L - T \sin(\theta_T + \alpha) + W \cos(\gamma))$$

Thus when linearized

$$a_{zCG} = -\frac{1}{m} \left( \frac{1}{2} \rho_0 S_{ref} V_0^2 C_{L\alpha} + T_0 \cos(\theta_{T0} + \alpha_0) \right) \bar{\alpha} - \frac{T_0 \cos(\theta_{T0} + \alpha_0)}{m} \theta_T^- - \frac{1}{2m} \rho_0 S_{ref} V_0^2 C_{L\delta_F} \delta_F$$

Given  $x$  the abscissa of a point on the missile, the lateral acceleration measured at this point will be

$$a_{z,x} = a_{z,CG} + (x_{CG} - x) \dot{q}$$

### 3.2. FLIGHT DYNAMICS

---

Hence using Equation 3.4 and linearizing

$$a_{z,x} = a_{z,CG} + \frac{1}{J_y} (x_{CG} - x) \left( \frac{1}{2} \rho_0 S_{ref} V_0^2 L_{ref} C_{m\alpha} \bar{\alpha} - T_0 \cos(\theta_{T0}) x_{CG} \bar{\theta}_T + \frac{1}{2} \rho_0 S_{ref} V_0^2 L_{ref} C_{m\delta_F} \delta_F \right)$$

For a node  $i$ ,  $x_i = (i - 1) l$ .

This yields the output equation

$$y = C \begin{bmatrix} \bar{\alpha} \\ q \end{bmatrix} + D \begin{bmatrix} \bar{\theta}_T \\ \delta_F \end{bmatrix}$$

The matrices  $C$  and  $D$  are

$$C = \begin{bmatrix} 0 & 1 \\ C_\alpha & 0 \\ C_\alpha + (x_{CG} - 9l) C_{\Delta x} & 0 \\ C_\alpha + (x_{CG} - 52l) C_{\Delta x} & 0 \\ C_\alpha + (x_{CG} - 82l) C_{\Delta x} & 0 \\ C_\alpha + (x_{CG} - 91l) C_{\Delta x} & 0 \end{bmatrix}$$

where

$$\begin{cases} C_\alpha &= -\frac{1}{m} \left( \frac{1}{2} \rho_0 S_{ref} V_0^2 C_{L\alpha} + T_0 \cos(\theta_{T0} + \alpha_0) \right) \\ C_{\Delta x} &= \frac{1}{2 J_y} \rho_0 S_{ref} V_0^2 L_{ref} C_{m\alpha} \end{cases}$$

and

$$D = \begin{bmatrix} 0 & 0 \\ D_{\theta_T} & \\ D_{\theta_T} + (x_{CG} - 9l) D_{\Delta x \theta_T} & D_{\delta_F} + (x_{CG} - 9l) D_{\Delta x \delta_F} \\ D_{\theta_T} + (x_{CG} - 52l) D_{\Delta x \theta_T} & D_{\delta_F} + (x_{CG} - 52l) D_{\Delta x \delta_F} \\ D_{\theta_T} + (x_{CG} - 82l) D_{\Delta x \theta_T} & D_{\delta_F} + (x_{CG} - 82l) D_{\Delta x \delta_F} \\ D_{\theta_T} + (x_{CG} - 91l) D_{\Delta x \theta_T} & D_{\delta_F} + (x_{CG} - 91l) D_{\Delta x \delta_F} \end{bmatrix}$$

where

$$\begin{cases} D_{\theta_T} &= -\frac{1}{m} T_0 \cos(\theta_{T0} + \alpha_0) \\ D_{\Delta x \theta_T} &= -\frac{1}{J_y} T_0 \cos(\theta_{T0}) x_{CG} \\ D_{\delta_F} &= -\frac{1}{2m} \rho_0 S_{ref} V_0^2 C_{L\delta_F} \\ D_{\Delta x \delta_F} &= \frac{1}{2 J_y} \rho_0 S_{ref} V_0^2 L_{ref} C_{m\delta_F} \end{cases}$$

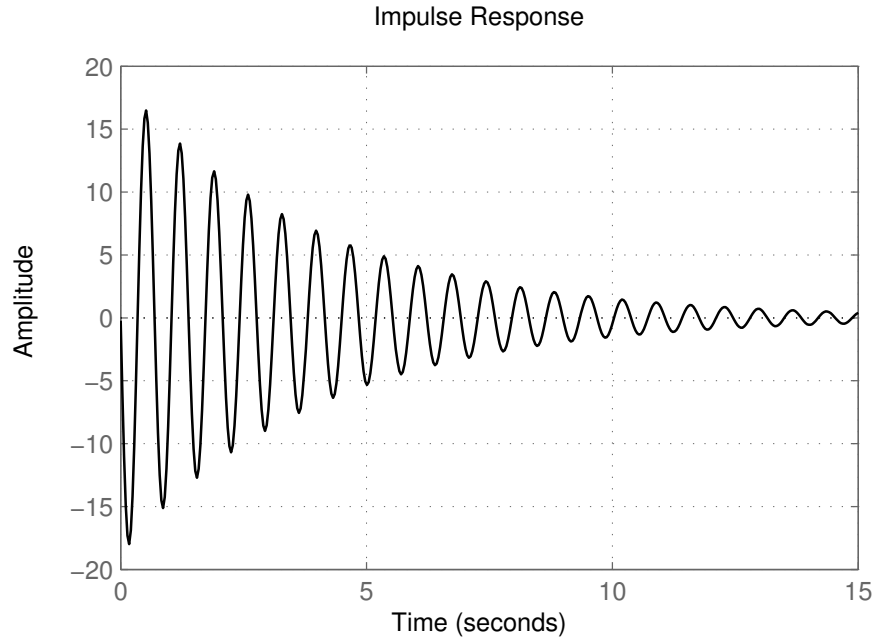


Figure 3.6: Impulse response of  $\frac{\alpha}{\theta_T}(s)$

Numerically this gives

$$C = \begin{bmatrix} 0 & 1 \\ -341 & 0 \\ -458 & 0 \\ -278 & 0 \\ -160 & 0 \\ -123 & 0 \end{bmatrix} \quad D = \begin{bmatrix} 0 & 0 \\ -160 & -25.5 \\ -402 & -12.3 \\ -30.7 & -32.5 \\ 213 & -45.8 \\ 289 & -49.9 \end{bmatrix}$$

### 3.2.8 Short Period Pitch Oscillations

The state-space system obtained has two complex conjugate poles corresponding to the SPPO. Its natural frequency is  $9.1 \text{ rad.s}^{-1}$  and the damping is 2.8%. This weak damping is a classical issue with such missiles. On Figure 3.6 the angle of attack response to an impulse on the thrust orientation is plotted.

### 3.3 Actuators Dynamics

The missile is directed with thrust vectoring. The two nozzles at the tail of the missile are mounted with hydraulic cylinders. The nozzles can be oriented to create a lateral component of thrust that will generate a moment at the center of gravity. This moment will change the angle of attack of the missile to create a lateral acceleration.

Its bandwidth is estimated to be up to  $25\text{ Hz}$ . The actuator dynamic is thus represented with a second order transfer function of cutoff frequency of  $25\text{ Hz}$  and a damping ratio of 0.7:

$$H_{nozzles}(s) = \frac{1}{40.5 \cdot 10^{-6}s^2 + 9.00 \cdot 10^{-3}s + 1}$$

The fins, located in the middle of the missile, is faster with a bandwidth of  $50\text{ Hz}$ . Its dynamics are model by a second order transfer function of cutoff frequency of  $50\text{ Hz}$  and a damping ratio of 0.7:

$$H_{fins}(s) = \frac{1}{10.1 \cdot 10^{-6}s^2 + 4.50 \cdot 10^{-3}s + 1}$$

### 3.4 Structural Model

#### 3.4.1 From continuous to discrete

ASTER 30 length is 4.9 m and the largest diameter is 0.36 m on the booster hence the missile can be considered as a beam with variable cross section. Euler-Bernoulli beam theory is suitable here because higher order models like Timoshenko beam theory would bring additive complexity and precision that are not needed for this study. Therefore sections rotational inertia and shear deformation are neglected. For the purpose of this study, only bending along y-axis is considered so deformations of the missile are contained in the zx-plane.

During the acceleration phase, ASTER 30 is composed of two parts: the booster and the dart. Both of them can be modeled as cylindrical pipes. The booster section has a diameter of 36 cm and the dart is 18 cm wide. The skin thickness<sup>1</sup> of the missile is 2.5 mm. These dimensions are illustrated in Figure 3.7.

The material used for the missile is assumed to be 30% carbon fibres composites and unidirectional along the longitudinal axis. The Young modulus along the x-axis is  $E = 180\text{ GPa}$  for this material. The second moment of area at the neutral axis along y-axis for a cylindrical section is:

$$I_{O,y} = \pi \frac{D^4 - (D - 2e)^4}{64}$$

---

<sup>1</sup>Estimated from the natural frequency of the 1st bending mode at 20Hz

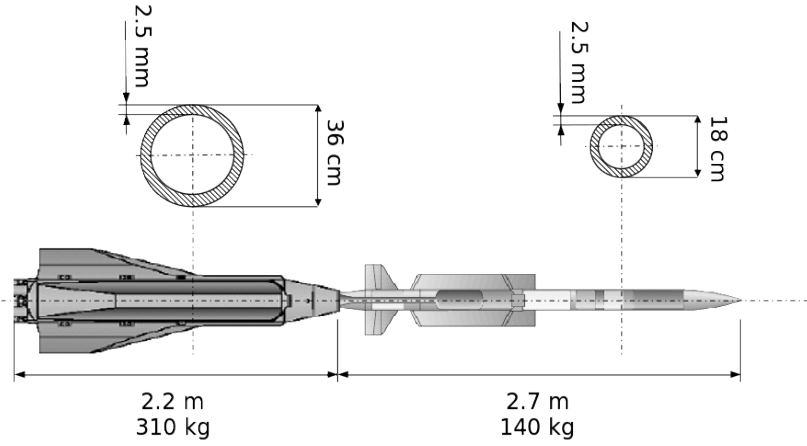


Figure 3.7: ASTER 30 Dimensions

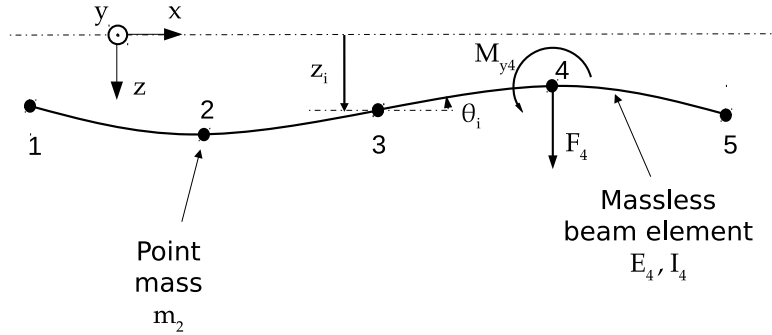


Figure 3.8: Lumped Element Model (5 nodes)

with  $D$  and  $e$  the external diameter and thickness of the pipe. Thus, the second moment of area for the booster and the dart are :

$$\begin{cases} I_{O,y_{booster}} &= 4.49 \cdot 10^{-5} m^4 \\ I_{O,y_{dart}} &= 5.49 \cdot 10^{-6} m^4 \end{cases}$$

It is assumed that the missile mass is equally distributed in the dart and in the booster therefore the linear mass density  $\rho_m$  is uniform in the booster, and uniform in the dart:

$$\begin{cases} \rho_{m_{booster}} &= 140.9 \text{ kg.m}^{-1} \\ \rho_{m_{dart}} &= 51.9 \text{ kg.m}^{-1} \end{cases}$$

It is necessary to discretise the body in order to be able to conduct a state-space representation and simulations. To reach this goal, the mathematical model of the structure is designed using a lumped element model illustrated in Figure 3.8.

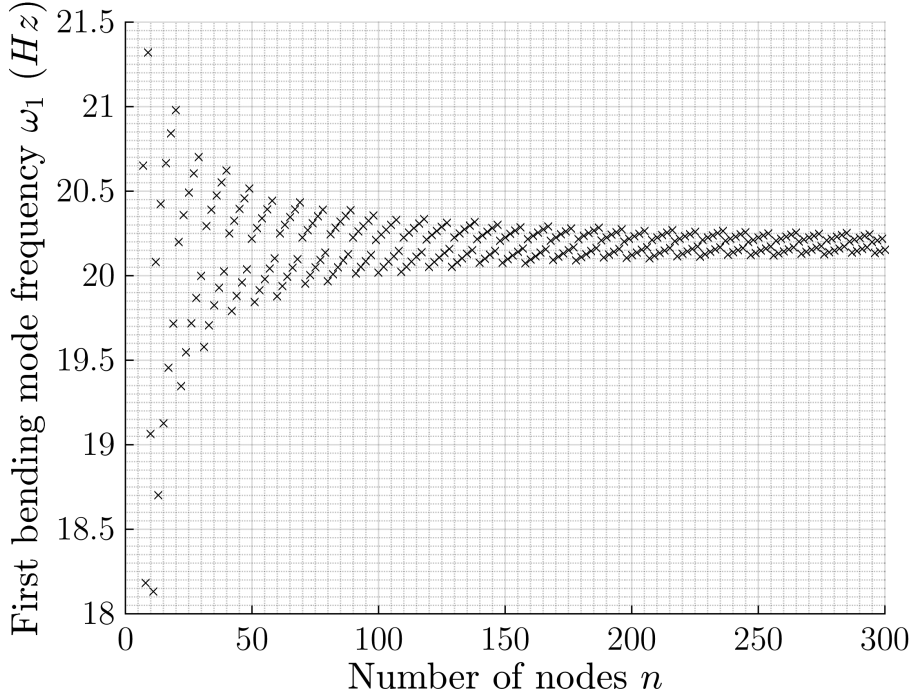


Figure 3.9: Computed First Bending Mode Natural Frequency

**Geometry** The missile is longitudinally discretised in  $n$  nodes evenly spaced by the beams length  $l = \frac{L}{n-1}$ . The nodes  $i$  and  $i+1$  are linked together by a massless Euler-Bernoulli beam  $i$ . Let  $z_i$ ,  $\dot{z}_i$  and  $\ddot{z}_i$  be respectively the displacement, speed and acceleration of node  $i$  along the z-axis.  $\theta_i$ ,  $\dot{\theta}_i$  and  $\ddot{\theta}_i$  are respectively the pitch angle, pitch rate and pitch acceleration of the beams at the junction node  $i$ .

To determine the number of nodes needed, one can consider looking at the natural frequencies of the beam converging as  $n$  grows. On Figure 3.9, first structural mode frequencies have been computed<sup>2</sup> for  $n$  varying between 7 and 300. The frequency converges when  $n$  increases. Eventually  $n = 100$  is a good choice to minimize the number of nodes for computational efficiency and having an acceptable accuracy on natural frequencies. Indeed, at about  $n = 100$ , the frequency oscillates between 20.02 Hz and 20.36 Hz which corresponds to 1.7 % of variation. It is worth noting that the uncertainty on the real first mode frequency is 5 to 10 % so with  $n = 100$ , the first mode frequency can be said as converged.

**Mass and stiffness** Each node  $i \in \llbracket 1, n \rrbracket$  has a point mass  $m_i$  that is the mass of the section from  $x = (i - \frac{3}{2})l$  to  $x = (i - \frac{1}{2})l$ . Thus the mass is conserved during the discretization :  $\sum_{i=1}^n m_i = m$ . The Euler-Bernoulli beam  $i$  has a Young modulus

<sup>2</sup>The method to do so will be explained later.

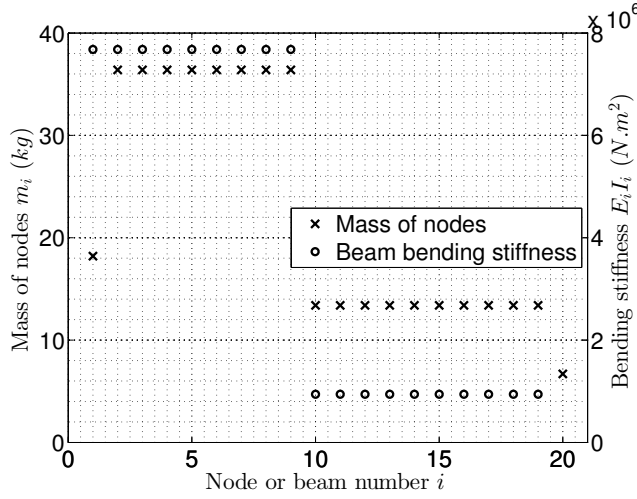


Figure 3.10: Summary of Structural Parameters for 20 Nodes

denoted  $E_i$  and the second moment of area at neutral axis passing through  $G$  and along  $y$ -axis named  $I_{G,y,i}$ . For readability purposes,  $I_{G,y,i}$  will be noted  $I_i$  but the reader must be careful not to confuse it with a rotational inertia, generally noted  $J$  in this thesis.

The different structural parameters of the body are summarized in Figure 3.10 for  $n = 100$ . It is clear that the booster is stiffer and heavier than the dart.

**External efforts** On each node  $i$ , an external force  $F_i$  along the  $z$ -axis and an external moment  $M_{y,i}$  along the  $y$ -axis are applied.

This lumped element model will be used to obtain the bending dynamics of ASTER 30.

### 3.4.2 Second-Order Structural Model

#### 3.4.2.1 Nodal Model

To generate a second-order structural model, Prentis and Leckie's method [3] will be used. This finite element model can be fully characterized by the following second-order structural equation:

$$M' \ddot{u} + D' \dot{u} + K' u = F' \quad (3.7)$$

### 3.4. STRUCTURAL MODEL

---

- $u = \begin{bmatrix} z_1 \\ \vdots \\ z_n \\ \theta_1 \\ \vdots \\ \theta_n \end{bmatrix}$  is the displacement vector

- $F' = \begin{bmatrix} F_1 \\ \vdots \\ F_n \\ M_{y,1} \\ \vdots \\ M_{y,n} \end{bmatrix}$  is the external efforts matrix

- $M'$  is the mass matrix of this system :  $M' = \begin{bmatrix} M & 0_{n \times n} \\ 0_{n \times n} & J_y \end{bmatrix}$ .  $M$  and  $J_y$  are diagonal matrices containing nodes masses and rotational inertias about the y-axis.
- $K'$  and  $D'$  are the stiffness and damping matrices of this system.

$K'$  can be divided in four sub-matrices  $K' = \begin{bmatrix} K_{11} & K_{12} \\ K_{21} & K_{22} \end{bmatrix}$ . In a static situation where  $\ddot{u}$  and  $\dot{u}$  are zero, the equation 3.7 becomes :

$$K' u = F'$$

Thus

$$\begin{bmatrix} K_{11} & K_{12} \\ K_{21} & K_{22} \end{bmatrix} \begin{bmatrix} z \\ \theta \end{bmatrix} = \begin{bmatrix} F \\ M_y \end{bmatrix} \quad (3.8)$$

To derive  $K'$  this matrix, one can **consider only two nodes  $i$  and  $i + 1$**  linked with the beam  $i$ . Equation 3.8 is simplified to:

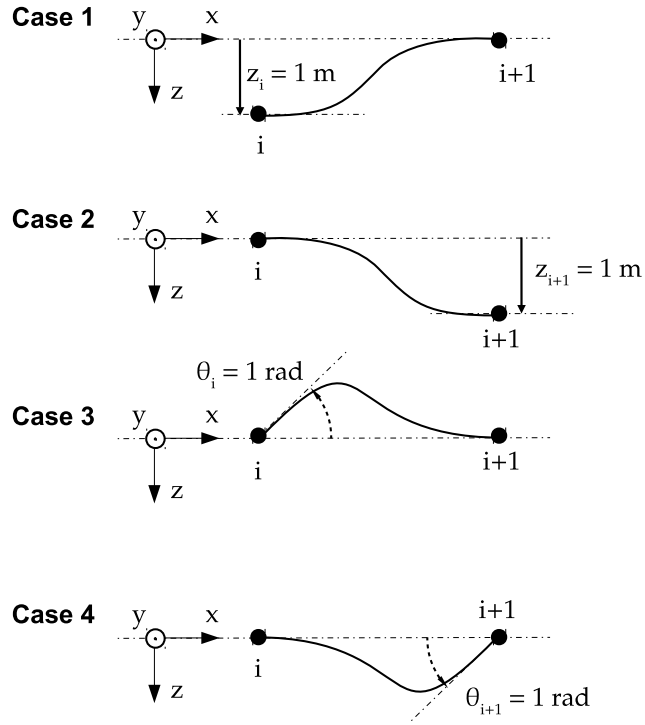


Figure 3.11: Elementary Cases for Two Nodes

$$\begin{bmatrix} K_{11,i} & K_{12,i} \\ K_{21,i} & K_{22,i} \end{bmatrix} \begin{bmatrix} z_i \\ z_{i+1} \\ \theta_i \\ \theta_{i+1} \end{bmatrix} = \begin{bmatrix} F_i \\ F_{i+1} \\ M_{y,i} \\ M_{y,i+1} \end{bmatrix}$$

Four cases are considered and illustrated in Figure 3.11:

	$z_i$	$z_{i+1}$	$\theta_i$	$\theta_{i+1}$
Case 1	1	0	0	0
Case 2	0	1	0	0
Case 3	0	0	1	0
Case 4	0	0	0	1

The forces and moments applied to the beam are  $F_i$ ,  $F_{i+1}$ ,  $M_{y,i}$  and  $M_{y,i+1}$ . The equilibrium between external efforts on the beam gives the two equations (forces and moments at node  $i$ ):

### 3.4. STRUCTURAL MODEL

---

$$F_i + F_{i+1} = 0 \quad (3.9)$$

$$M_{y,i} + M_{y,i+1} - l \cdot F_{i+1} = 0$$

Using beam theory, the deformation and efforts are linked with the equation

$$E_i I_i \frac{\partial^2 z}{\partial x^2}(x) = -M_y(x) \quad (3.10)$$

where and  $M_y(x) = M_{y,i+1} - (l - x) F_{i+1}$  are local young modulus, second moment of area and pitching moment at abscissa  $x$ <sup>3</sup>. For readability purposes,  $E_i I_i$  will now be noted  $EI_i$ . This yields after integration and double integration

$$EI_i \theta(x) = -\frac{1}{2}x^2 F_{i+1} + x (-M_{y,i+1} + l F_{i+1}) + A \quad (3.11)$$

$$EI_i z(x) = -\frac{1}{6}x^3 F_{i+1} + \frac{1}{2}x^2 (-M_{y,i+1} + l F_{i+1}) + A x + B \quad (3.12)$$

with A and B integration constants.

The boundary conditions are

$$\begin{cases} \theta(0) = \theta_i \\ \theta(l) = \theta_{i+1} \\ z(0) = z_i \\ z(l) = z_i \end{cases} \quad (3.13)$$

Thus, the system of equations 3.9, ??, 3.11 and 3.12 with the boundary conditions 3.13 for each case 1 to 4 yields :

	Case 1	Case 2	Case 3	Case 4
$F_i$	$12 EI_i/l^3$	$-12 EI_i/l^3$	$-6 EI_i/l^2$	$-6 EI_i/l^2$
$F_{i+1}$	$-12 EI_i/l^3$	$12 EI_i/l^3$	$6 EI_i/l^2$	$6 EI_i/l^2$
$M_{y,i}$	$-6 EI_i/l^2$	$6 EI_i/l^2$	$4 EI_i/l$	$2 EI_i/l$
$M_{y,i+1}$	$-6 EI_i/l^2$	$6 EI_i/l^2$	$2 EI_i/l$	$4 EI_i/l$

thus  $k_{11,i}$ ,  $k_{12,i}$ ,  $k_{21,i}$  and  $k_{22,i}$  derived from the table above are

---

<sup>3</sup> $x = 0$  at node  $i$  and  $x = l$  and node  $i + 1$

$$\begin{cases} K_{11,i} & = \frac{12EI_i}{l^3} \begin{bmatrix} 1 & -1 \\ -1 & 1 \end{bmatrix} \\ K_{12,i} = K_{21,i}^T & = \frac{6EI_i}{l^2} \begin{bmatrix} -1 & -1 \\ 1 & 1 \end{bmatrix} \\ K_{22,i} & = \frac{2EI_i}{l} \begin{bmatrix} 2 & 1 \\ 1 & 2 \end{bmatrix} \end{cases}$$

Now considering the complete missile, as the element beams are linked in series, the matrices  $K_{11}$ ,  $K_{12}$ ,  $K_{21}$ , and  $K_{22}$  can be calculated by summing the matrices  $K_{11,i}$ ,  $K_{12,i}$ ,  $K_{21,i}$  and  $K_{22,i}$  on the diagonal as shown below for  $K_{11}$ :

$$K_{11} = \begin{bmatrix} k_{11,1} & & & & & & & & \\ & k_{11,2} & & & & & & & \\ & & k_{11,3} & & & & & & \\ & & & k_{11,\dots} & & & & & \\ & & & & k_{11,n-1} & & & & \\ & & & & & & & & \\ & & & & & & & & \\ & & & & & & & & \\ & & & & & & & & \end{bmatrix} \quad \begin{matrix} 0 \\ 0 \end{matrix}$$

Thus, these matrices are

$$K_{11} = \frac{12}{l^3} \begin{bmatrix} EI_1 & -EI_1 & 0 & \cdots & 0 \\ -EI_1 & EI_1 + EI_2 & \ddots & \ddots & \vdots \\ 0 & \ddots & \ddots & \ddots & 0 \\ \vdots & \ddots & \ddots & EI_{n-2} + EI_{n-1} & -EI_{n-1} \\ 0 & \cdots & 0 & -EI_{n-1} & EI_{n-1} \end{bmatrix}$$

$$K_{12} = K_{21}^T = \frac{6}{l^2} \begin{bmatrix} -EI_1 & -EI_1 & 0 & \cdots & 0 \\ EI_1 & EI_1 - EI_2 & \ddots & \ddots & \vdots \\ 0 & \ddots & \ddots & \ddots & 0 \\ \vdots & \ddots & \ddots & EI_{n-2} - EI_{n-1} & -EI_{n-1} \\ 0 & \cdots & 0 & EI_{n-1} & EI_{n-1} \end{bmatrix}$$

$$K_{22} = \frac{2}{l} \begin{bmatrix} 2EI_1 & EI_1 & 0 & \cdots & 0 \\ EI_1 & 2EI_1 + 2EI_2 & \ddots & \ddots & \vdots \\ 0 & \ddots & \ddots & \ddots & 0 \\ \vdots & \ddots & \ddots & 2EI_{n-2} + 2EI_{n-1} & EI_{n-1} \\ 0 & \cdots & 0 & EI_{n-1} & 2EI_{n-1} \end{bmatrix}$$

It is worth noting that  $K' = K'^T$  that can be explained by Maxwell-Betti reciprocal work theorem.

**Simplified second-order structural model** In this study, we assume that the pure external moments  $M_{y,i}$  are negligible when compared to moments created by the forces  $F_i$ . The missile is modeled as an Euler-Bernoulli beam, thus the local rotational inertias  $I_i$  are zero. The damping  $D'$  is very few for such flexible structures so it can be neglected for the next trick. With these hypotheses, the lower part of Equation 3.7 concerning rotational accelerations becomes :

$$0_{n \times 1} \ddot{\theta} + 0_{n \times 1} \dot{\theta} + K_{21}z + K_{22}\theta = 0_{n \times 1}$$

$K_{22}$  is a symmetric tridiagonal matrix which invertibility can be proven by LU decomposition [19]. This leads to the important relation between  $z$  and  $\theta$ :

$$\theta = -K_{22}^{-1} K_{21}z \quad (3.14)$$

This equation mean that the second part of  $u$  can be entirely determined from its first part. The upper part of the Equation 3.7 fully describes the structural system:

$$M \ddot{z} + D \dot{z} + (K_{11} - K_{12}K_{22}^{-1}K_{21})z = F$$

The stiffness matrix is then  $K = K_{11} - K_{12}K_{22}^{-1}K_{21}$ . One can verify that  $K^T = K$ .

The damping matrix is chosen proportional to  $K$  and set to damp the first structural mode to 1%. This gives  $D = K/6000$ . The second-order structural equation is as follows:

$$M \ddot{z} + D \dot{z} + K z = F \quad (3.15)$$

### 3.4.2.2 Modal Model

The triplet  $(M, D, K)$  is the nodal realization of the second-order structural model. A modal realization must be found to extract the flexible body modes from the

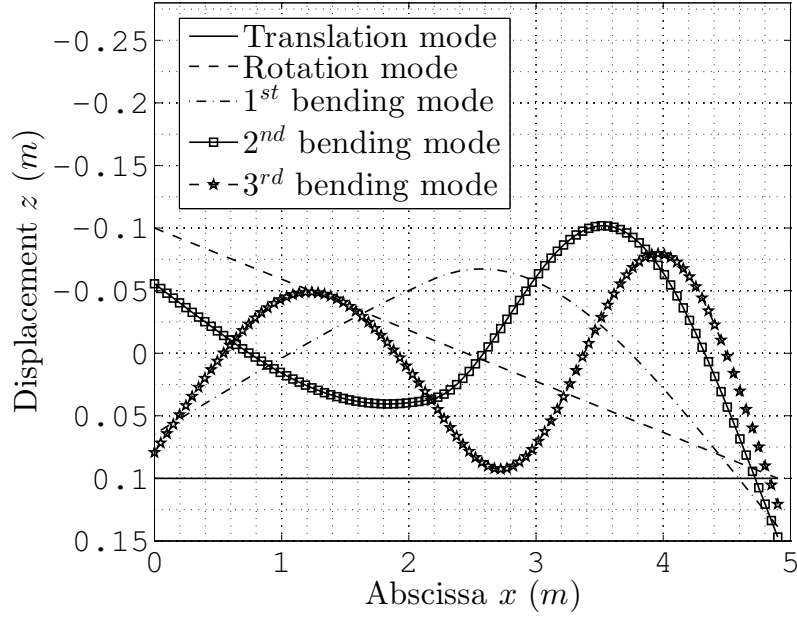


Figure 3.12: Modes Shape of ASTER 30

structural model. The transformation of the nodal model is described in [4] and can be derived as follows.

Considering free vibrations without damping, the system being linear, the displacement vector will be  $z = \phi e^{j\omega t}$  with  $\phi$  constant thus  $\ddot{z} = -\omega^2 \phi e^{j\omega t}$  and Equation 3.15 becomes:

$$(-\omega^2 M + K) \phi = 0 \quad (3.16)$$

Non-trivial solutions to Equation 3.16 (i.e.  $\phi \neq 0$ ) exist if and only if

$$\det(-\omega^2 M + K) = 0$$

The solutions are the generalized eigen values  $(\omega_1^2, \omega_2^2, \dots, \omega_n^2)$  of the matrices  $K$  and  $M$ .  $(\omega_1, \omega_2, \dots, \omega_n)$  are the natural frequencies of the structure and the eigen vectors  $(\phi_1, \phi_2, \dots, \phi_n)$  are the natural modes also called modes shape.

In this particular study, the structure extremities are free hence the two first natural frequencies are 0 Hz and the two first natural modes correspond to the rigid-body modes: z-axis translation and y-axis rotation. The natural frequencies and modes shape are renamed  $(0, 0, \omega_1, \omega_2, \dots, \omega_{n-2})$  and  $(\phi_{0,1}, \phi_{0,2}, \phi_1, \phi_2, \dots, \phi_{n-2})$ .

The modes shape of the rigid-body and the first three bending modes are plotted in Figure 3.12. This figure shows that the dart is likely to bend more than the booster. Indeed, the front part of the missile is more flexible so it will bend more.

The natural frequencies for the first modes are summarized in Table 3.5.

### 3.4. STRUCTURAL MODEL

---

Mode	Natural Frequency		Damping Ratio
	(Hz)	(rad.s <sup>-1</sup> )	
z translation mode	0	0	0
y rotation mode	0	0	0
1 <sup>st</sup> bending mode	20.0	125	1.0%
2 <sup>nd</sup> bending mode	67.7	425	3.5%
3 <sup>rd</sup> bending mode	139.7	877	7.3%
4 <sup>th</sup> bending mode	213.9	1344	11%
5 <sup>th</sup> bending mode	335.1	2106	17%

Table 3.5: Natural Frequencies and Damping Ratios of Modes

Let  $\Phi = [\phi_{0,1} \ \phi_{0,2} \ \phi_1 \ \phi_2 \ \dots \ \phi_{n-2}]$  be the modal matrix and

$$\Omega = \begin{bmatrix} 0 & & & & \\ & 0 & & & 0 \\ & & \omega_1 & & \\ & & & \ddots & \\ 0 & & & & \omega_{n-2} \end{bmatrix}$$

be the matrix of natural frequencies.

Let  $z_m$  be the displacement vector of modes defined by  $z = \Phi z_m$ . The modal matrices of mass  $M_m$ , damping  $D_m$  and stiffness  $K_m$  are obtained as follows

$$M_m = \Phi^T M \Phi$$

$$D_m = \Phi^T D \Phi$$

$$K_m = \Phi^T K \Phi$$

The triplet  $(M_m, D_m, K_m)$  defines the second-order structural modal model of the missile. The equation 3.15 becomes:

$$M_m \ddot{z}_m + D_m \dot{z}_m + K_m z_m = \Phi^T F \quad (3.17)$$

### 3.4.2.3 Output equation

Three types of sensors are investigated in this paper to measure vibrations: strain gauges, gyroscopes and accelerometers. Their measurements can be represented by the output equation:

$$y = C_{oz}z + C_{ov}\dot{z} + D_oF \quad (3.18)$$

where  $y$  is a vector containing the measurement of all sensors.

It means that the signal measured by the sensors are a linear combination of the displacement of the nodes (matrix  $C_{oz}$ ), their speed (matrix  $C_{ov}$ ) and also a feedforward term  $D_o$  on the external forces applied on the nodes.

**Gyroscope** A gyroscope on node  $i$  measures  $\dot{\theta}_i$ , thus  $n$  gyroscopes can be placed. Since  $q$  is often used to represent the pitch rate, this letter will be used for gyroscope output matrices. According to Equation 3.14,  $\theta = -K_{22}^{-1}K_{21}z$ , therefore  $\dot{\theta}_i = -K_{22}^{-1}K_{21}\dot{z}$ . This yields the output matrices

$$C_{ozq} = 0_{n \times n} \quad C_{ovq} = -K_{22}^{-1}K_{21} \quad \text{and} \quad D_{oq} = 0_{n \times n}$$

**Accelerometer** An accelerometer on node  $i$  measures  $\ddot{z}_i$ . The letter assigned to acceleration measurement will be  $a$  like “acceleration” and the measurement will be called  $a_z$ . With an accelerometer on each node, there are  $n$  accelerometers. In Equation 3.18,  $\ddot{z}$  does not appear. But using the second-order structural equation 3.15:

$$\ddot{z} = -M^{-1}Kz - M^{-1}D\dot{z} + F$$

thus

$$C_{oza} = -M^{-1}K \quad C_{ova} = -M^{-1}D \quad \text{and} \quad D_{oa} = Id_n$$

**Strain gauge** For a strain gauge, a first order Taylor development to approximate the spatial derivative of  $\theta(x)$  at node  $i$  will be conducted. This approximation cannot be made on nodes 1 and  $n$  therefore, only  $n - 2$  strain gauges are considered. The letter used for this sensor is  $\varepsilon$  which is often assigned to strains.

The Euler-Bernoulli beam theory assumes that each section stays perpendicular to the neutral axis. The strain gauges are placed on the upper side of the missile therefore, the local deformation at the surface is

$$\varepsilon(x) = -\frac{\partial\theta}{\partial x} \frac{D(x)}{2}$$

where  $D(x)$  is the local missile diameter. It is worth noting that  $\varepsilon(x)$  is positive when the strain gauge is stretched and negative when it is compressed.

### 3.4. STRUCTURAL MODEL

---

The partial derivative of  $\theta$  with respect to  $x$  is approximated using a first order Taylor development at node  $i \in [2, n - 1]$ :

$$\frac{\partial \theta}{\partial x}(x_i) \simeq \frac{\theta_{i+1} - \theta_{i-1}}{2l}$$

thus

$$\varepsilon_i = \frac{-\theta_{i+1} + \theta_{i-1}}{2l} \frac{D_i}{2}$$

Let  $\varepsilon = (\varepsilon_i)_{i \in [2, n-1]}$ , then the previous equation yields

$$\varepsilon = T_\varepsilon \theta$$

with

$$T_\varepsilon = \frac{1}{4l} \begin{bmatrix} D_2 & 0 & -D_2 & & & 0 \\ & D_3 & 0 & -D_3 & & \\ & & D_4 & 0 & -D_4 & \\ & & & \ddots & \ddots & \ddots \\ & & & & D_{n-2} & 0 & -D_{n-2} \\ 0 & & & & D_{n-1} & 0 & -D_{n-1} \end{bmatrix}$$

Finally, using Equation 3.14, the relation becomes

$$\varepsilon = -T_\varepsilon K_{22}^{-1} K_{21} z$$

hence

$$C_{oz\varepsilon} = -T_\varepsilon K_{22}^{-1} K_{21} \quad C_{ov\varepsilon} = 0_{(n-2) \times n} \quad \text{and} \quad D_{o\varepsilon} = 0_{(n-2) \times n}$$

**Concatenation** The output vector corresponding to the concatenation of all

measurements is  $y = \begin{bmatrix} \varepsilon \\ q \\ a_z \end{bmatrix}$ . Therefore

$$C_{oz} = \begin{bmatrix} C_{oz\varepsilon} \\ C_{ozq} \\ C_{oza} \end{bmatrix} \quad C_{ov} = \begin{bmatrix} C_{ov\varepsilon} \\ C_{ovq} \\ C_{ova} \end{bmatrix} \quad \text{and} \quad D_o = \begin{bmatrix} D_{o\varepsilon} \\ D_{oq} \\ D_{oa} \end{bmatrix}$$

**Modal output matrix** The Output Equation 3.18 will finally be

$$y = C_{oz}\Phi z_m + C_{ov}\Phi \dot{z}_m + D_o F$$

defining the modal equivalent of the output matrices :

$$y = C_{mz}z_m + C_{mv}\Phi \dot{z}_m + D_o F$$

with

$$\begin{cases} C_{mz} &= C_{oz}\Phi \\ C_{mv} &= C_{ov}\Phi \end{cases}$$

### 3.4.3 Rigid-body Modes Elimination

The second-order structural model and its output equation in there modal forms have been derived. However, the two rigid-body modes - translation and rotation - must be eliminated. Indeed, this Chapter aims at modeling only vibrations during the flight. The rigid-body dynamics modeled have been derived isolated from gravity and air and do not reflect flight dynamics hence they must be suppressed to keep only vibrations dynamics.

The matrices  $M_m$ ,  $D_m$  and  $K_m$  are diagonal meaning that there is no interaction between modes in Equation 3.17. The rigid-body modes are eliminated by erasing the two first rows of  $\Phi$ . Hence it is now  $\Phi = [\phi_1 \phi_2 \dots \phi_{n-2}]$  and  $z_m$  only contains structural modes displacement. By doing so, modal mass, damping and stiffness matrices size is now  $(n - 2) \times (n - 2)$ .

Looking at the output Equation 3.18, truncating the rigid-body modes will remove rigid-body pitch rate and strain measurement is not influenced by rigid-body modes. However, great care must be taken for the acceleration measurement as  $D_{oa} \neq 0$ . To compute the acceleration measurements only due to the vibrations, the acceleration measurements due to the rigid-body modes will be calculated considering a rigid structure.

If the missile is considered as a solid, the equation of lateral acceleration at the center of gravity is:

$$a_{z,CG} = \frac{1}{m} F_z$$

and the equation of rotational acceleration is

$$\ddot{\theta} = \frac{1}{J_{y,CG}} M_{y,CG}$$

where  $F_z$  is the sum of external forces along the z-axis,  $M_{y,CG}$  is the sum of moments applied at the center of gravity along the y-axis,  $m$  and  $J_y$  are the mass

### 3.4. STRUCTURAL MODEL

---

and rotational inertia about the center of gravity along the y-axis. The force and moments are:

$$F_z = \sum_{j=1}^n F_j$$

$$M_{y,CG} = \sum_{j=1}^n (x_{CG} - x_j) F_j$$

The rigid-body acceleration at each node  $i$  is

$$a_{z,rb,i} = a_{z,CG} + (x_{CG} - x_i) \ddot{\theta}$$

Hence, it yields

$$a_{z,rb,i} = \frac{1}{m} \sum_{j=1}^n F_j + (x_{CG} - x_i) \frac{1}{J_y} \sum_{j=1}^n (x_{CG} - x_j) F_j$$

In matrix formulation,

$$a_{z,rb} = D_{oa,rb} F$$

where

$$D_{oa,rb} = \frac{1}{m} Id_n + \frac{1}{J_y} \begin{bmatrix} x_{CG} \\ x_{CG} - l \\ \vdots \\ x_{CG} - (n-2)l \\ x_{CG} - (n-1)l \end{bmatrix} \begin{bmatrix} x_{CG} & x_{CG} - l & \dots & x_{CG} - (n-2)l & x_{CG} - (n-1)l \end{bmatrix}$$

Finally, the output matrix  $D_{oa,rb}$  is subtracted from  $D_{oa}$  to obtain the output matrix from vibrations only :

$$D_{oa,fb} = D_{oa} - D_{oa,rb}$$

However, this is not completely correct. Indeed, the rigid-body dynamics are different when the missile is considered as flexible. Therefore the rigid-body component in  $D_{oa}$  is not  $D_{oa,rb}$ . Looking at the Bode plot of the transfer function<sup>4</sup> from  $F_1$  to  $a_{z,75}$  on Figure 3.13, with this first rigid-body subtraction technique, at  $\omega = 0$ ,  $a_{z,75}(\omega)$  is not zero (curve “a\_z,fb imperfect”). This is incorrect because at  $\omega = 0$ , the vibrations are not excited and should be nonexistent and  $a_{z,75} = 0$ . Once the state space representation will be established, the good correction will be applied in 3.4.4.1.

---

<sup>4</sup>Established later

### 3.4.4 State Space Model

Previously, the second-order structural model in its modal form without the rigid-body modes has been derived. This representation is not convenient for control design. Therefore a state-space representation of this system will be created.

#### 3.4.4.1 From Second-Order Model to State Space Model

The system must firstly be translated into a state space representation.

Now that the rigid-body modes are eliminated,  $K_m$  is positive-definite and we can define

$$\Omega = M_m^{-1/2} K_m^{1/2}$$

$$Z = \frac{1}{2} M_m^{-1} D_m \Omega^{-1}$$

$Z$  is a diagonal matrix containing the modes damping ratios. For instant  $Z_{3,3} = \zeta_3$  is the damping ratio of the third bending mode.

The state vector is defined as  $x = \begin{bmatrix} z_m \\ \dot{z}_m \end{bmatrix}$ . The input vector is  $u = F$ . The output vector is  $y = \begin{bmatrix} \varepsilon \\ q \\ a_z \end{bmatrix}$ . Thus

$$\dot{x} = Ax + Bu$$

$$y = Cx + Du$$

with

$$A = \begin{bmatrix} 0_{(n-2) \times (n-2)} & Id_{n-2} \\ -\Omega^2 & -2Z\Omega \end{bmatrix}$$

$$B = \begin{bmatrix} 0_{(n-2) \times n} \\ \Phi^T \end{bmatrix}$$

$$C = \begin{bmatrix} C_{mz} & C_{mv} \end{bmatrix}$$

$$D = D_o = \begin{bmatrix} 0_{(n-2) \times n} \\ 0_{n \times n} \\ D_{oa,fb} \end{bmatrix}$$

### 3.4. STRUCTURAL MODEL

---

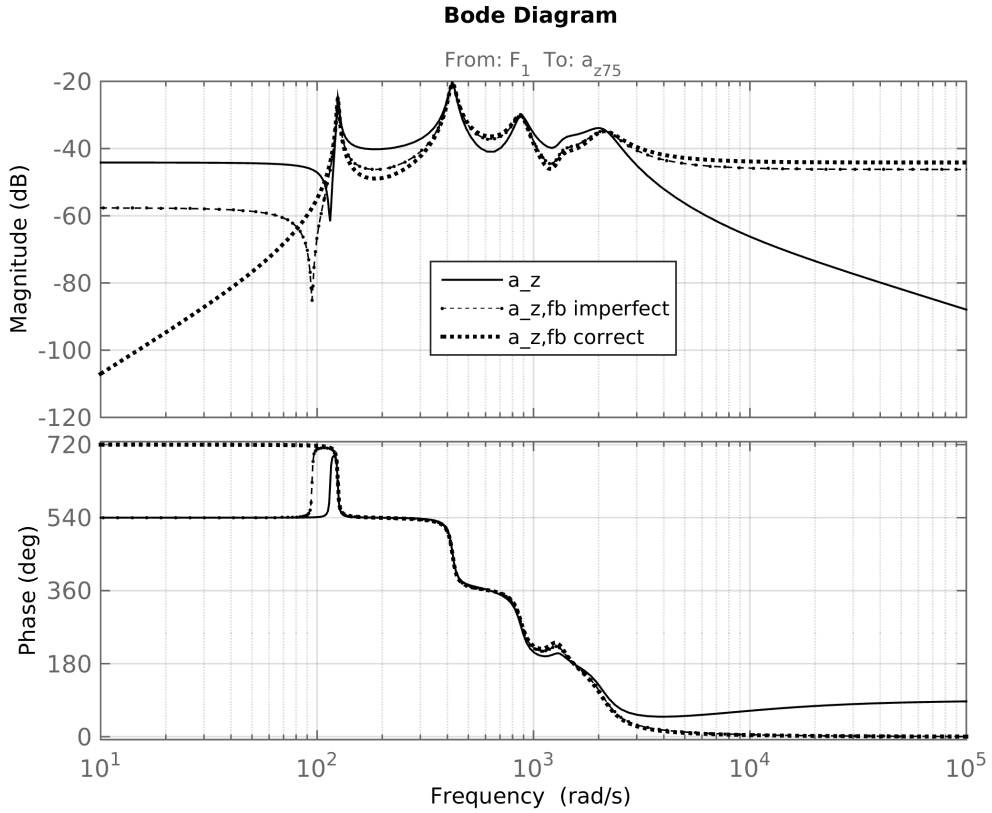


Figure 3.13: Bode plot of  $F_1$  to  $a_{z,75}$

In the previous part,  $D_{oa,fb}$  has not been clearly defined. To eliminate properly rigid-body dynamics measured by acceleration sensors, the following technique can be used. The acceleration due to rigid-body dynamics is composed of a feedforward term  $D_{oa,rb}$  only. In the transfer function, this is a static gain. Thus, one can just remove this static value :

$$a_{z,fb}(j\omega) = -C_{ma}(A - j\omega Id)^{-1}B + D_{oa,fb}$$

where  $C_{ma} = \begin{bmatrix} C_{mza} & C_{mva} \end{bmatrix}$ . At  $\omega = 0$ ,  $a_z = 0$  so  $D_{oa,fb} = C_{ma}A^{-1}B$ .

Thanks to this,  $a_{z,fb}$  is 0 at low frequency as shown in Figure 3.13 (curve "a\_z,fb correct").

#### 3.4.4.2 Formulation in State Space Modal Form 2

Gawronski [4] gives a convenient state space formulation of the structural system. It is the modal form 2. In this form, the state vector is

$$x_m = \begin{bmatrix} z_{m,1} \\ z_{mo,1} \\ z_{m,2} \\ z_{mo,2} \\ \vdots \\ z_{m,(n-2)} \\ z_{mo,(n-2)} \end{bmatrix}$$

where  $z_{mo,i} = \zeta_i z_{m,i} + \dot{z}_{m,i}/\omega_i$ . In this form, the modal state matrix  $A_m$  has the particular form:

$$A_m = \begin{bmatrix} A_{m1} & & & \\ & A_{m2} & & \\ & & \ddots & \\ & & & A_{m(n-2)} \end{bmatrix}$$

$$\text{with } A_m = \begin{bmatrix} -\zeta_i \omega_i & \omega_i \\ \omega_i & -\zeta_i \omega_i \end{bmatrix}.$$

The transformation matrix  $V_m$  defined as  $x = V_m x_m$  for 4 modes is

$$V_m = \begin{bmatrix} 1 & 0 & & & \\ & 1 & 0 & & \\ & & 1 & 0 & \\ & & & 1 & 0 \\ -\omega_1/\zeta_1 & \omega_1 & & & \\ & -\omega_2/\zeta_2 & \omega_2 & & \\ & & -\omega_3/\zeta_3 & \omega_3 & \\ & & & -\omega_4/\zeta_4 & \omega_4 \end{bmatrix}$$

Hence,  $B_m = BV_m$ ,  $C_m = CV_m$  and  $D_m = D$ .

This final state-space realization  $(A_m, B_m, C_m, D_m)$  is the modal state-space model of the bending vibrations of the missile with outputs  $y$  containing  $n - 2$  strain measurements  $\varepsilon_i$ ,  $n$  gyroscope measurements  $q_i$  and  $n$  accelerometers  $a_{zi}$ . This vibrations model will then be added to the flight dynamics model.

### 3.4. STRUCTURAL MODEL

---

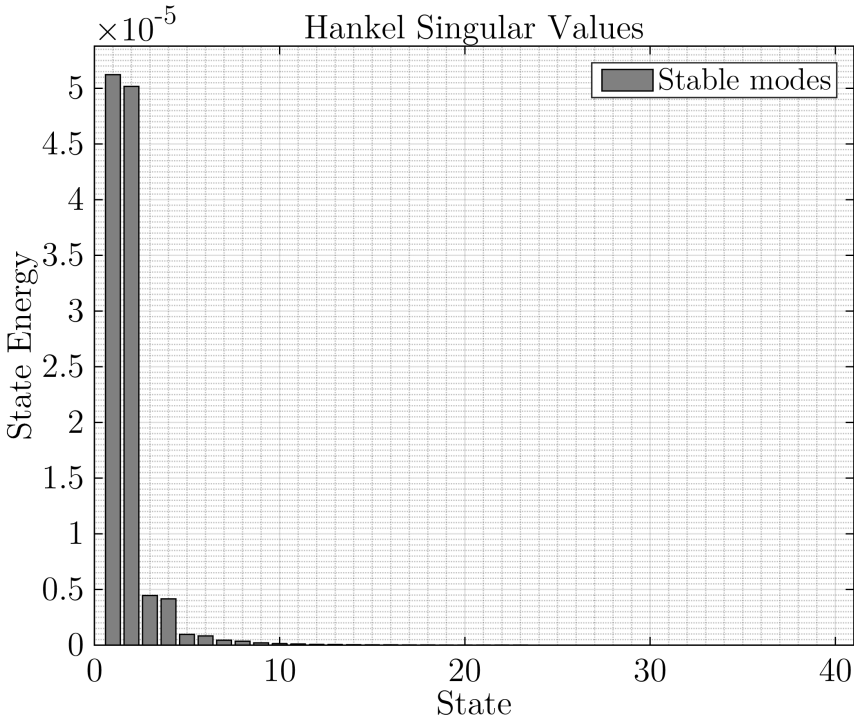


Figure 3.14: Hankel Singular Values Decomposition - Strain Gauges Output

#### 3.4.5 Model Reduction

Currently, the structural model has  $n - 2$  bending modes. The number of nodes chosen is 100 so 98 modes are considered. Most of the high frequency modes are inaccurate because of the Euler-Bernoulli model which is only suitable for low frequency dynamics. Fortunately, these high frequency modes do not contribute much to the system dynamics. A way to compare every mode contribution is to use the Hankel singular values decomposition of the system. On Figures 3.14, 3.15, 3.16, the state contribution in the Hankel singular values have been plotted

for the three different types of sensor. The state vector is  $x_m = \begin{bmatrix} q_{mi} \\ q_{moi} \end{bmatrix}_i$ . The first five bending modes will be kept, the others are truncated. Indeed, on these bar plots, the contribution of the 6<sup>th</sup> bending mode (bar 11 and 12) and higher (13 and above) is negligible. These modes correspond to less than 0.5% of the singular value of the 1<sup>st</sup> mode for the strain gauges, less than 1% for the gyroscopes and 5% for the accelerometers.

To reduce the model to the five first modes, the new state space model is  $(A_m^5, B_m^5, C_m^5, D_m^5)$ .  $A_m^5$  is the  $10 \times 10$  upper left corner of  $A_m$ ,  $B_m^5$  is the 10 first rows of  $B_m$ ,  $C_m^5$  is the 10 first columns of  $C_m$  and  $D_m^5$  is equal to  $D_m$ .

From now on,  $(A_m^5, B_m^5, C_m^5, D_m^5)$  will be simply named  $(A, B, C, D)$ .

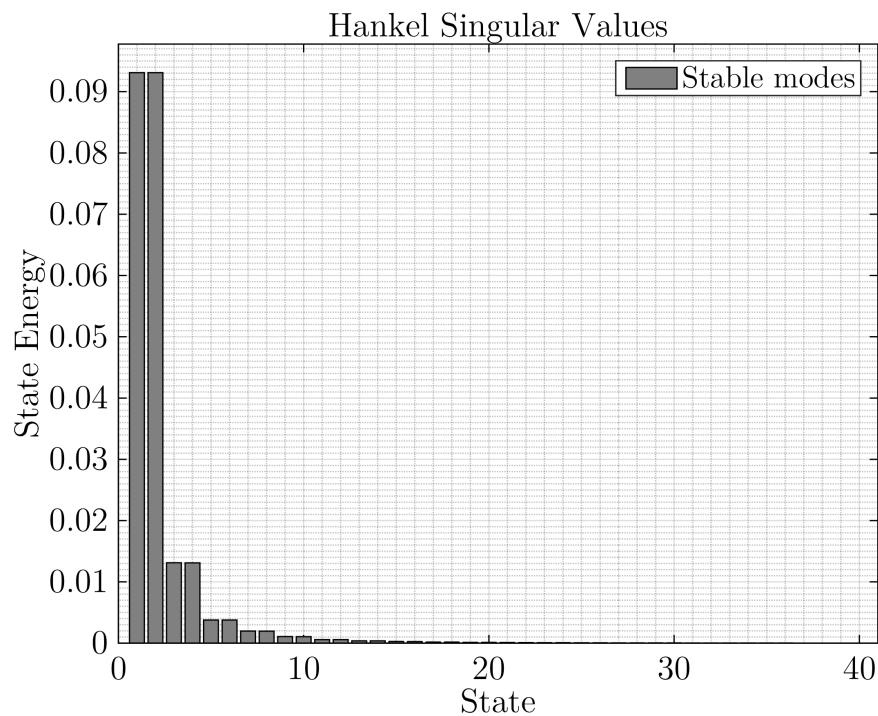


Figure 3.15: Hankel Singular Values Decomposition - Gyroscopes Output

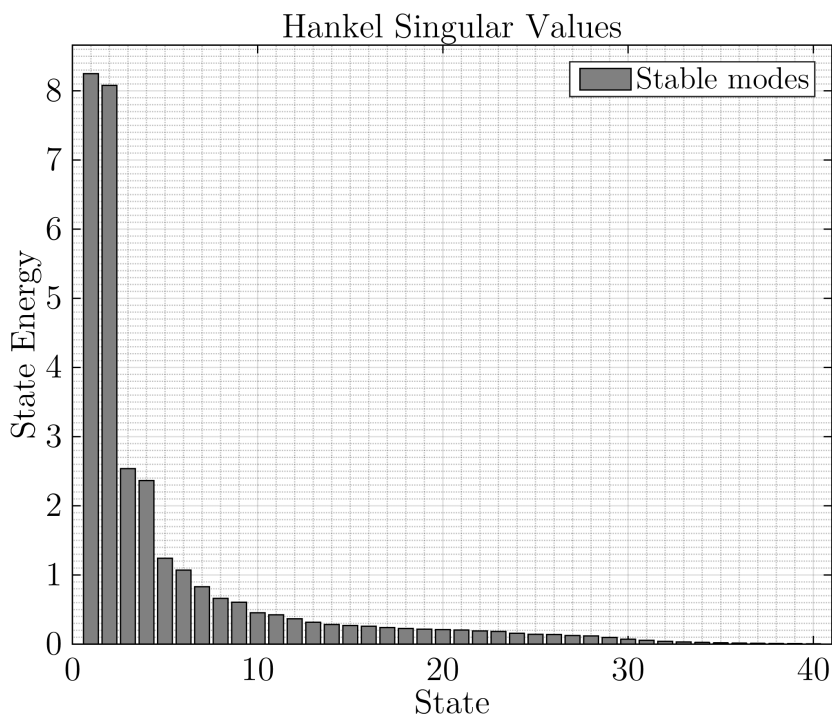


Figure 3.16: Hankel Singular Values Decomposition - Accelerometers Output

## 3.5 Actuators & Sensors Placement

### 3.5.1 Actuators Selection

The goal of this paper is to enhance the performance of ASTER 30 by adding sensors. No actuator will be added from the original ASTER 30 design. Indeed adding actuators to an existing missile already in service can be very cumbersome and costly. The only actuators available are the thrust vectoring by nozzle orientation at the very rear of the missile and the fins at the tail of the dart. The position of these two actuators on the airframe are  $x_{nozzle} = 0\text{ m}$  and  $x_{fins} = 2.4\text{ m}$ . These positions corresponds to the nodes 1 and 50.

It is assumed that the vibrations are mainly excited by the lateral forces generated by these two actuators. The aerodynamic forces are too distributed and weak compared to the rocket motor lateral thrust at the rear of the booster to create significant bending.

The only inputs to the vibration system are thus lateral forces at nodes 1 and 50. The previous system ( $A, B, C, D$ ) is modified<sup>5</sup> to keep only the inputs  $F_1$  and  $F_{50}$ .

### 3.5.2 Sensors Placement

The state space model developed in the previous section outputs three different types of sensors : strain gages, gyroscopes and accelerometers on all possible nodes<sup>6</sup>. However, only some of these sensors need to be kept. For each of these types of sensor, the minimum number required to control the structure will be computed and the optimal locations will be determined using a technique of placement.

#### 3.5.2.1 Placement Indices

Gawronski gives a method to quantitatively assess the location of a sensor given its type [4]. He proposes three different norms : the  $H_2$  Norm, the  $H_\infty$  Norm and the Hankel Norm. Here, the placement will rely on  $H_\infty$  Norm. The sensors will be placed only considering the 1<sup>st</sup> bending mode. The higher modes have high natural frequencies that cannot be actively damped. Indeed Table 3.5 gives natural frequencies for the 2<sup>nd</sup> mode and higher above 50Hz which is the cutoff frequency of the fins actuator. Moreover the first bending mode is the most critical to damp because it generates great vibrations at low frequency and spoil sensors and seeker measurements.

The first step is to select a set of possible locations for a type of sensor. Let be  $S = \{i_1, i_2, \dots, i_s\}$  this set with  $s$  the number of possible locations. At each of

---

<sup>5</sup>Only columns 1 and 50 of  $B$  and  $D$  are kept.

<sup>6</sup> $n - 2$  for the strain gauges and  $n$  for the gyroscopes and the accelerometers.

these locations, an index is calculated which represents the ability of the sensor to sense the 1<sup>st</sup> bending mode at this place. This index is called  $\sigma_i$  for the node  $i$ . A simple way to define it is

$$\sigma_i = \|G_{1i}\|_\infty$$

where  $G_{1i}$  is the transfer function of  $[F_1, F_{50}]$  to the sensor considered at node  $i$  considering only the 1<sup>st</sup> mode.

The damping ratio of the 1<sup>st</sup> bending mode is only 1% so the following approximation can be made for the strain gauge and the gyroscopes:

$$\|G_{1i}\|_\infty \simeq \frac{\|B_1\|_2 \|C_{i1}\|_2}{2\zeta_1 \omega_1}$$

The matrices  $B_1$  and  $C_{i1}$  are the input and output matrices at node  $i$  for the sensor considered and the 1<sup>st</sup> bending mode.  $B_1$  is the first two rows of  $B$  and  $C_{i1}$  is the first two columns of the part of  $C$  corresponding to the type of sensor

$$\text{considered knowing that } C = \begin{bmatrix} C_\varepsilon \\ C_q \\ C_{a_z} \end{bmatrix}.$$

For instance for a gyroscope at node  $i$ ,  $C_{i1}$  is  $C_q(i, 1..2)$ .

For the accelerometers, the feedforward matrix  $D$  is none zero thus a little modification needs to be done:

$$\|G_{1i}\|_\infty \simeq \omega_1 \frac{\|B_1\|_2 \|C_{i1}\|_2}{2\zeta_1 \omega_1}$$

The bigger is  $\sigma_i$  the greater is the amplitude of the signal measured by the sensor at node  $i$ . Thanks to this method, the locations can be ranked to determine the optimal position to place the sensors. For each type of sensor - strain gages, gyroscopes and accelerometers - this technique will be used.

### 3.5.2.2 Strain Gauges Placement

A strain gauge is a long resistor fixed on the skin of the structure. When the skin is stretched or compressed, the strain gauge is deformed and the electrical resistance changes. These variations of electrical resistance can be precisely measured with a Weathstone bridge. The great advantage of this sensor is its insensitivity to the rigid-body dynamics of the system. This kind of sensor measures only deformation. Thus, only one of these sensors appropriately placed can determine the flexure of the missile. However, it will be shown later that the signal of this sensor needs to be derivated to damp the 1<sup>st</sup> mode bending. This derivation is likely to increase noise propagation. Another disadvantage is its great sensitivity to temperature variation. The booster part of the missile is greatly heated by the

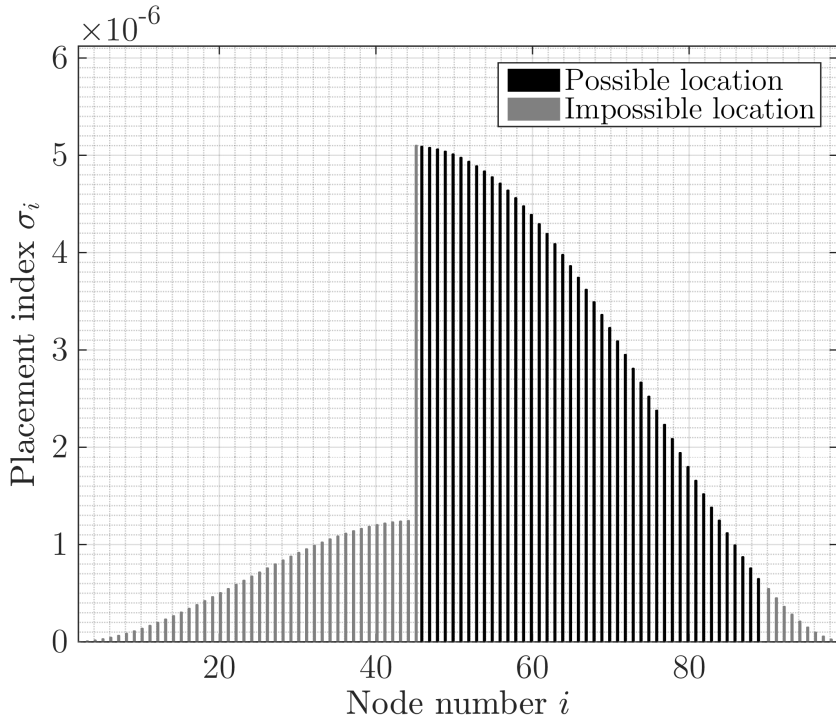


Figure 3.17: Placement Indices - Strain Gages

rocket engine and the head of the dart is aerodynamically heated. The possible locations are  $x \in [2.2m, 4.4m]$  that corresponds to the set of nodes  $S = \llbracket 46, 89 \rrbracket$ .

The placement indices have been computed at all locations  $i \in \llbracket 2, n - 1 \rrbracket$  even if the set of location is  $S = \llbracket 46, 89 \rrbracket$  to show entirely how these indices vary. They appear on Figure 3.17.

On the bar plot, the placement indices of locations on the booster are very low compared to those on the dart. Indeed the booster is very stiff so it bends very few compared to the dart. The best location for a strain gauge is at node 46 behind the fins at  $x = 2.23 m$  shown in Figure 3.20. This location corresponds to the strain anti-node of the 1<sup>st</sup> bending mode where the flexure is maximum.

### 3.5.2.3 Gyroscopes Placement

A gyroscope will measure not only the pitch rate due to the vibrations but also the pitch rate of the rigid-body. For instant, at node  $i$ , a gyroscope will measure

$$q_i = q_{i,fb} + q$$

To isolate the vibrations pitch rate, one needs the measurements of two gyroscopes placed at different locations. Hence, the pitch rate of the rigid-body can be removed by subtraction to keep only the vibrations measurement:

$$q_i - q_j = q_{i,fb} - q_{j,fb}$$

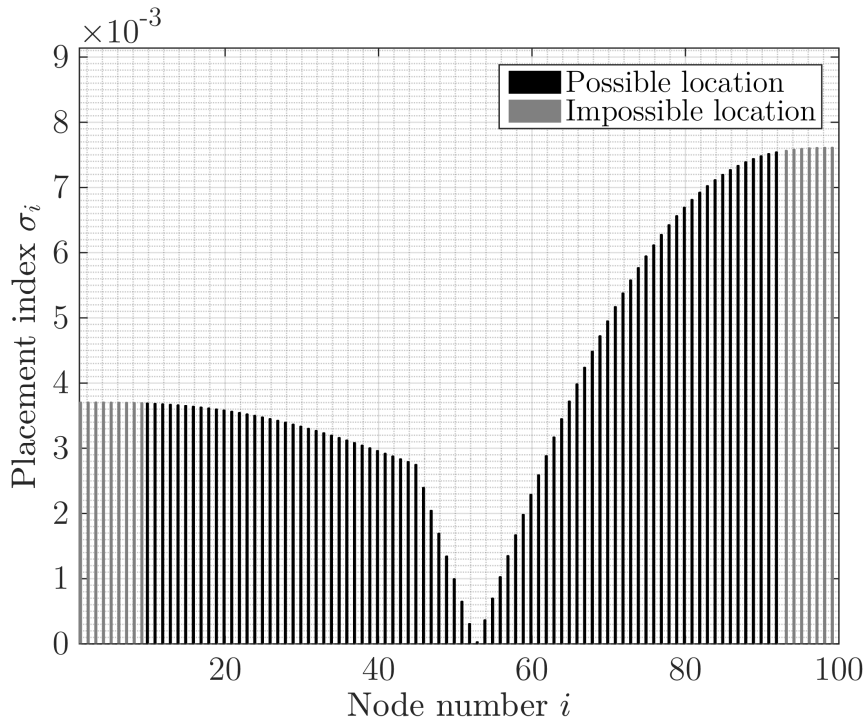


Figure 3.18: Placements Indices - Gyroscopes

At least two gyroscopes must be used.

A gyroscope is less sensitive to variations of temperature than a strain gauge and can be placed on the booster. However a margin is kept with the two extremities of the missile because the tail is heated by the engine flame and the nose contains the seeker. For the gyroscopes, the set of locations available is then  $S = [10, 92]$  corresponding to  $x = [0.45m, 4.40m]$ .

Figure 3.18 shows the placement indices for gyroscopes.

The nose is a place where the gyroscope would be very sensitive to the 1<sup>st</sup> bending mode. Actually, there is already a gyroscope in the sensor pack at  $x$  somewhere between 3.9 m and 4.3 m that correspond approximately to node 83. The second gyroscope must be placed at the other side of the zero pitch rate node 53. The second best position is then node 10. These locations are shown on Figure 3.20.

### 3.5.2.4 Accelerometers Placement

Accelerometers measure the lateral acceleration due to vibrations but also the lateral acceleration of the rigid-body. Moreover, the acceleration on the rigid-body depends of where the sensor is placed. At node  $i$ , an accelerometer will measure:

### 3.5. ACTUATORS & SENSORS PLACEMENT

---

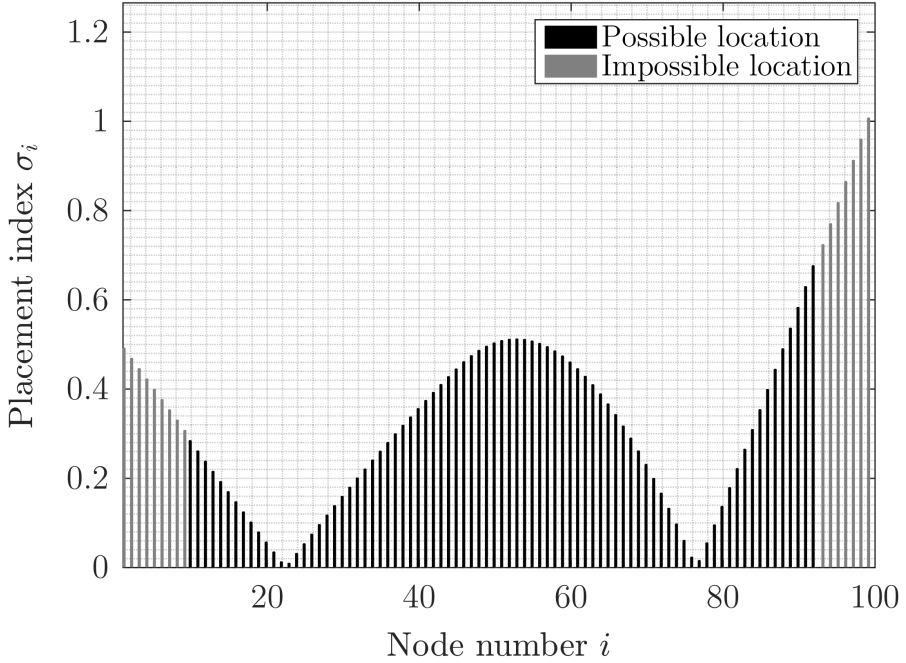


Figure 3.19: Placement Indices - Accelerometers

$$a_{z,i} = a_{z,rb,CG} + (x_{CG} - x_i) \dot{q} + a_{z,fb,i}$$

thus such a measurement contains three unknowns :  $a_{z,rb,CG}$ ,  $\dot{q}$  and  $a_{z,fb,i}$ . Therefore a minimum number of three accelerometers are needed at different locations to eliminate the acceleration of the center of gravity and the additional term due to pitch acceleration. It will be shown in 4.3.2.4 on page 72 that the abscissa of the center of gravity does not need to be known to extract the acceleration due to the vibrations. This is a relief since the position of the center of gravity moves during the flight.

Like a gyroscope, an accelerometer is not as sensible to temperature variations as a strain gage. Thus it can be placed within  $x = [0.45m, 4.40m]$  corresponding to the set  $S = [10, 92]$ . Once again, the placement indices are calculated all over the body in Figure 3.19.

The sensor pack of the missile already contains an accelerometer along the z-axis at node 83. This position is not very sensible to the first bending mode lateral accelerations as its placement index is very low. The sensor pack seems to be placed somewhere next to the vibration acceleration node. Hence this accelerometer cannot be used for bending vibration control.

The three best locations that have a great placement index and are uncorrelated are at nodes 10, 53 and 92. They are shown in Figure 3.20.

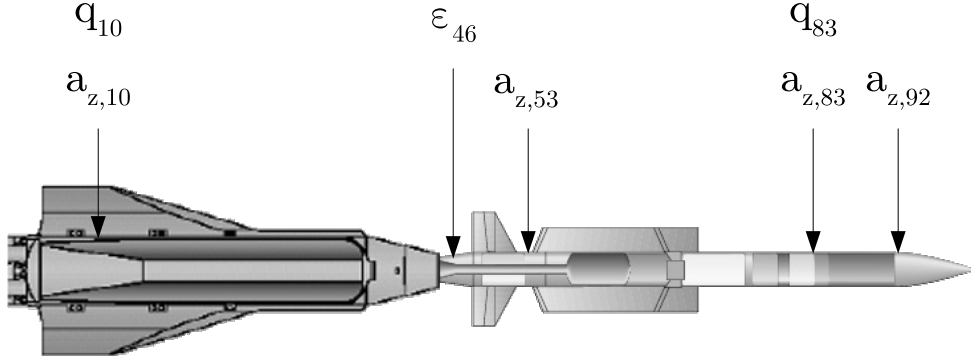


Figure 3.20: Sensors Locations - Strain gauges  $\varepsilon$ , Gyroscopes  $q$  and Accelerometers  $a_z$

### 3.5.2.5 Outputs Selection

Finally, from the model established in the previous Section, only a few outputs are kept. These outputs are:

- The gyroscope and the accelerometer from the sensor pack at node 83
- The added strain gauge at node 46
- The added gyroscope at node 10
- The added accelerometers at nodes 10, 53 and 92

This flexible body model has outputs that will be added to the rigid-body dynamics outputs previously derived in 3.2 on page 17. The fusion of these models is described in the next Section.

All of these sensors are summarized in Figure 3.20.

## 3.6 Flexible Missile Model

Now that the flight dynamics and the structural model have been derived, they need to be fused into a servo-aeroelastic model where actuators, flight dynamics and structure interact. Servo-aeroelastic models can be very complicated to establish therefore assumptions will be made on the interactions between the structure and the flight dynamics. These assumptions being made, the models will be put together and inputs and outputs will be defined.

### 3.6.1 Structural and Flight Dynamics Interactions

In Subsection 3.2.6 on page 24, it has been shown that lift and drag magnitude are each less than 17% of the thrust. The rocket engine thrust produces the greatest force. Thus, it is assumed that the aerodynamics will not create any structural deformation. Since only bending is considered only the lateral component of the thrust is kept for the structural model input. Indeed, the longitudinal component of the thrust will create local bending moments only when the beam is bent and since the bending deflection is only about a few millimeters, this component is neglected. The lateral component of the thrust is applied at the tail, on node 1 of the structural model.

The second input to the structural model is the lateral force generated by the fins deflection. Later, the fins will be used to generate an active damping of the bending modes. The lateral force generated by these fins is inserted at node 50 of the structural model. The lift they generate is

$$L_{fins} = \frac{1}{2}\rho SV_0^2 C_{L\delta_F} \delta_F$$

The lift generated by the angle of attack  $\alpha$  is not considered since it is assumed that the body aerodynamics do not generate bending.

The inputs to the flight dynamics are the thrust vectoring and the fins deflection. These two angles are controlled by second-order actuators of bandwidth of 25Hz and 50Hz before the flight dynamics block.

The last assumption is that the bending will not change the aerodynamic of the missile. Indeed the deformation is very little. The bending deflection is about a few millimeters that will not change the aerodynamic coefficients significantly. Therefore the structural model outputs will not be inputs of the flight dynamics.

### 3.6.2 Servo-aeroelastic Model Inputs and Outputs

The flexible missile inputs and outputs can be classified of 5 types:

- **Control inputs:** These inputs will be used by the controller to generate a lateral acceleration or to damp the bending modes. There are two: the thrust vectoring reference orientation  $\theta_{Tref}$  which commands the orientation of the nozzles with a second-order actuator and the fins reference deflection  $\delta_{Fref}$  that is the input of a second-order actuator controlling the fins.
- **Sensors outputs:** There are several sensors providing information on the system. They can be accelerometers, gyroscopes or a strain gauge. The accelerometers and gyroscopes have a component from the flight dynamics model also called the rigid-body component and another from the structural model called the flexible-body component or vibration component. The strain gauge only measures the strain at node 46 from the structural model.

- **Perturbation inputs:** Some signals are perturbed by inputs. These inputs can either be sensor noise like for the accelerometers or gyroscopes or perturbation forces from the rocket engine or on the fins.
- **Reference acceleration:** This input signal is generated by the navigation manager that often follow a proportional navigation. This is the reference to follow for the lateral acceleration controller.
- **Performance outputs:** They are additional outputs like the acceleration at centre of gravity, the nozzles and fins angle or the vibration components of sensors that cannot be measured but will be used to design or assess the controllers.

The fusion of the models is represented by a block diagram on Figure 3.21.  
This is on this model that the controllers will be designed.

### 3.6.3 Simulations

On Figures 3.22 and 3.23, a simulation shows how the missile reacts to a step input of  $1^\circ$  on  $\theta_{Tref}$ . The acceleration measured at node 83 is noisy because of the bending vibrations. They eventually disappear after 3 seconds.

### 3.6. FLEXIBLE MISSILE MODEL

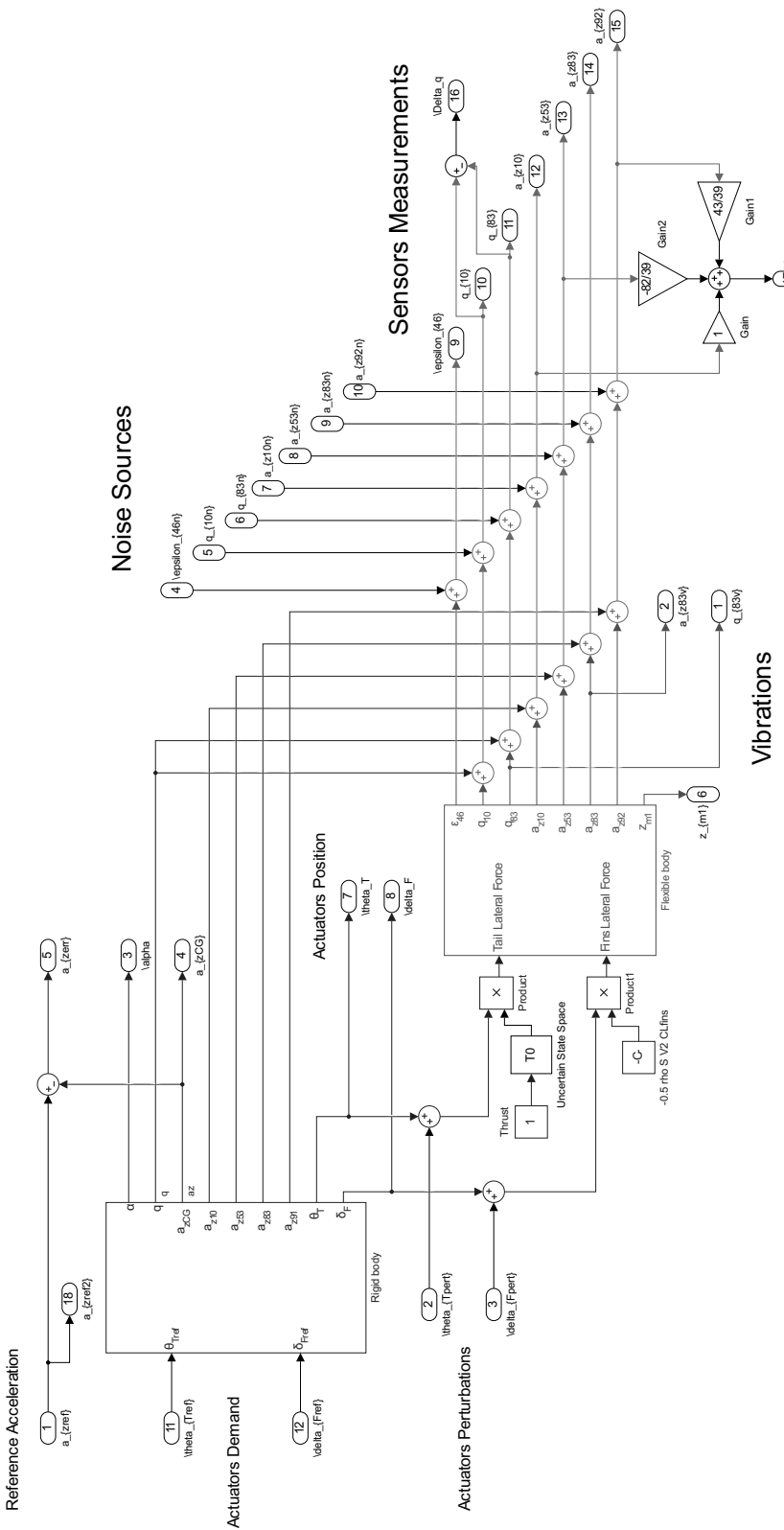


Figure 3.21: Flexible Missile Model

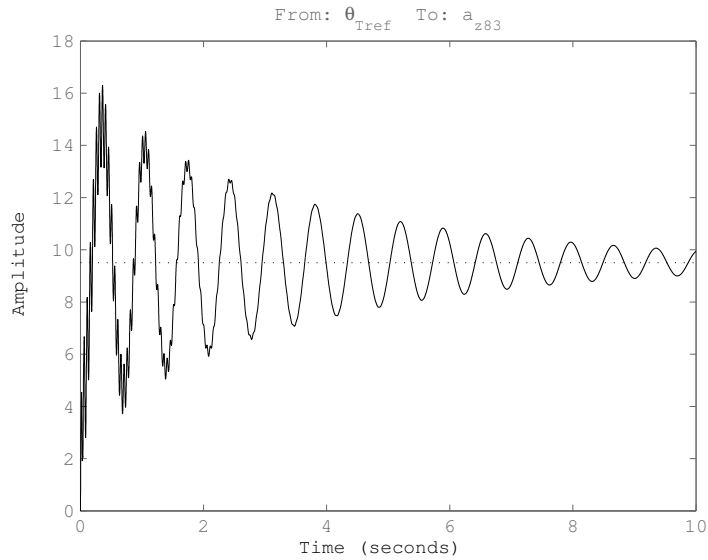


Figure 3.22: Step ( $1^\circ$ ) Response of  $\frac{a_{z83}}{\theta_{Tref}}(s)$  (10 s)

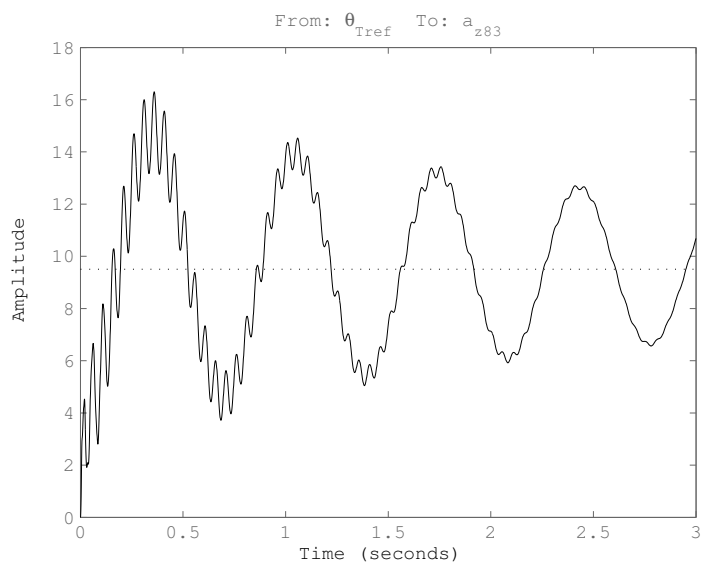


Figure 3.23: Step ( $1^\circ$ ) Response of  $\frac{a_{z83}}{\theta_{Tref}}(s)$  (3 s)



# Chapter 4

## Active Damping Autopilots

A flexible missile model has been established in the previous chapter. Based on this model, several active damping autopilots will be designed and compared to the conventional non damping autopilot.

### 4.1 Missile Control Inputs and Outputs

To control the flexible missile, several inputs and outputs are available. This Section discuss about those which will be used for the lateral acceleration control and others for the active damping.

#### 4.1.1 Actuators

The original ASTER 30 uses the orientable nozzles to control the missile lateral acceleration. The nozzles are actuated with hydraulic cylinders. The thrust deflection creates a lateral force on the tail of the missile creating a pitching moment at the missile centre of gravity. This will change its angle of attack and generate a lateral acceleration. Because of the hydraulic system and the great force required to actuate the nozzles, this actuator is relatively slow. Its bandwidth is about 25Hz which is fast enough to control the lateral acceleration and will be used for the lateral acceleration control.

The thrust vectoring might be too slow for actively damp the first bending mode. Thus, the dart fins will be used. Indeed, these fins are actuated by electric power and the efforts on these control surfaces is lower hence there bandwidth is about 50Hz. The first bending mode frequency is at 20Hz so the fins are fast enough to perform an active damping. Moreover, the fins deflection generate a lateral force at the missile centre. On the first bending mode shape, this is approximatively were the lateral displacement is maximum. The fins actuator has a great influence on the first bending mode. These reasons justify the use of fins to damp the bending vibrations.

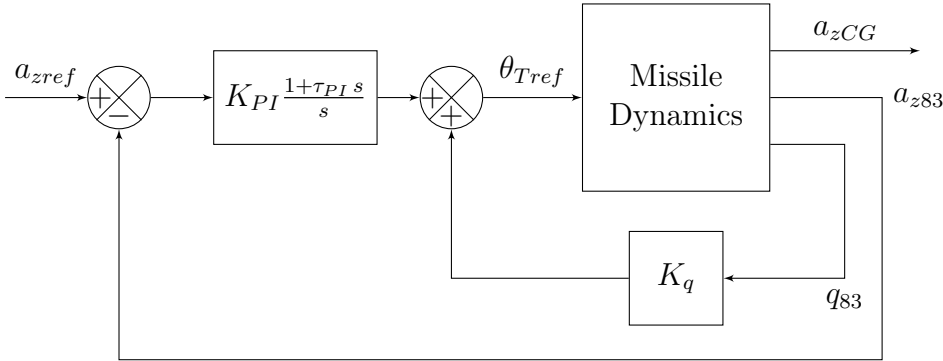


Figure 4.1: Latax Control Architecture

#### 4.1.2 Sensors

The sensors pack included in the original version of ASTER 30 contains an accelerometer and a gyroscope close to the nose. These sensors are the only two needed for the lateral acceleration control. With the missile modification presented in 3.5.2, several sensors have been added including a strain gauge, gyroscopes and accelerometers. They provide information on the bending state of the missile and will be used for the structural active damping.

## 4.2 Lateral Acceleration Control

A common feedback architecture to control the lateral acceleration generation uses a pitch rate feedback plus a proportional integral controller on the lateral acceleration. In the case of a simple rigid missile, the bending is not considered. To control the lateral acceleration, the closed-loop architecture is described on Figure 4.1.

The pitch rate feedback gain  $K_q$  is chosen to damp the short period pitch oscillation (SPPO). On Figure 4.2 is shown the root locus of this feedback. It proves that the SPPO mode changes in damping ratio and very few in natural frequency. This inner loop must be as fast as possible thus a damping ratio of 0.7 might be appropriate. For a rigid ASTER 30, it yields a pitch rate feedback gain  $K_q$  of 0.074.

The proportional integral corrector on the lateral acceleration  $PI(s) = K_{PI} \frac{1+\tau_{PI}s}{s}$  is set to make the system as fast as possible with reasonable gain and phase margins. For instance, a good compromise is

$$PI(s) = 0.009 \frac{1 + 0.1s}{s}$$

giving a phase margin of  $74^\circ$  for a rigid ASTER 30. The proportional integral corrector will only make the SPPO natural frequency lower. Thus, this double

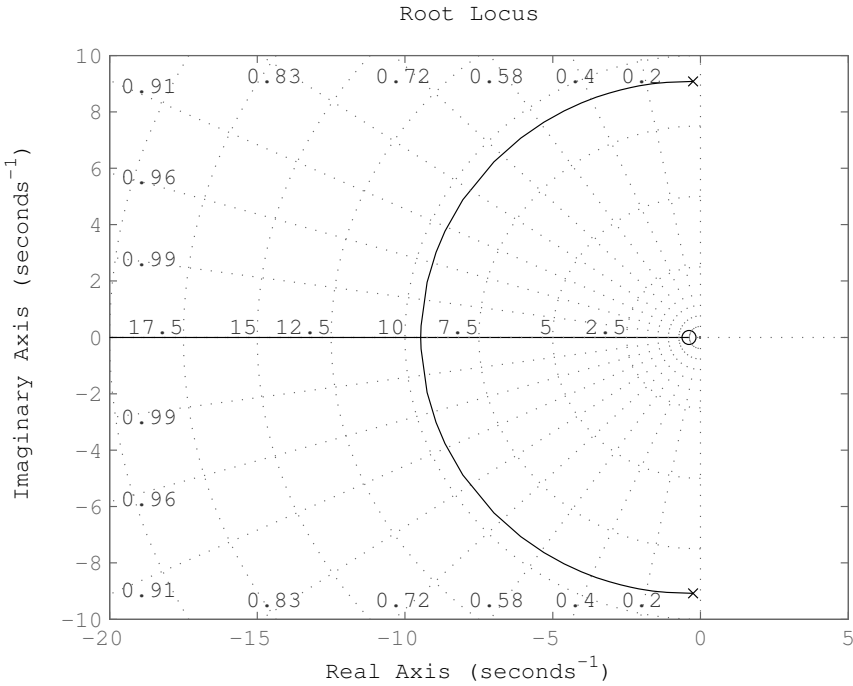


Figure 4.2: Root Locus of Pitch Rate Feedback

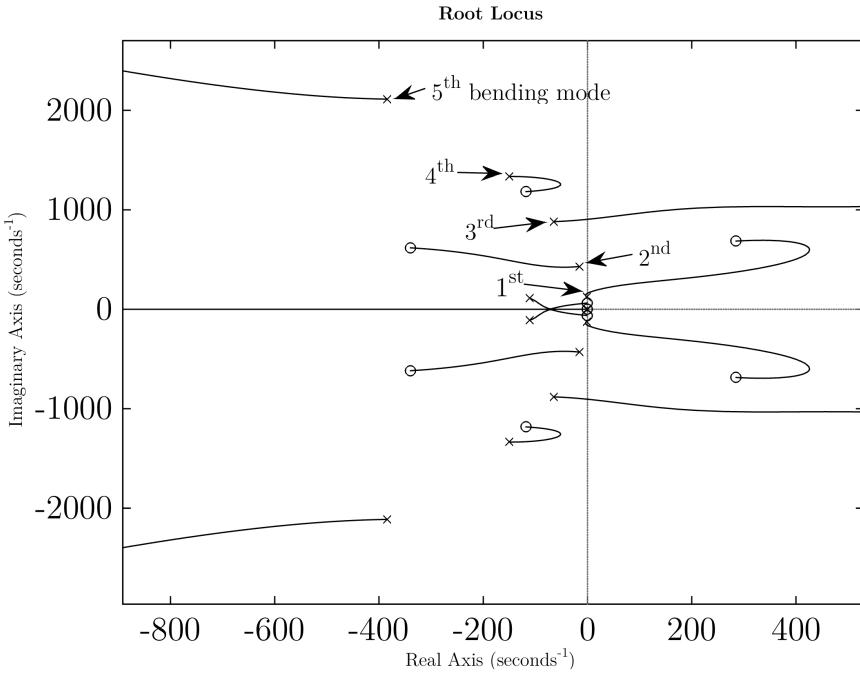
loop architecture cannot control the lateral acceleration faster than the SPPO. The SPPO is the limit to the lateral acceleration generation.

### 4.3 Vibrations Alleviation

For agile missiles such as ASTER, the actuators bandwidths are wide. Thus, if the command signal generated has a non zero component at the bending frequency, the structural mode will start to oscillate. This oscillation is measured by the sensors and fed through the controller which could amplify it. On Figure 4.3 is drawn the root locus for the system open loop from the nozzle orientation reference  $\theta_{Tref}$  to the pitch rate  $q_{83}$  measured at the sensor pack location, on node 83. The 1<sup>st</sup> and the 3<sup>rd</sup> bending mode can become unstable with this feedback which is supposed to damp the short period pitch oscillation (SPPO) if the gain is too big.

Even if the feedback gains are kept little to avoid a structural instability, the vibrations created by the rocket engine are amplified through the structure and measured by the sensors. This amplified signal will generate parasitic actuations of the thrust vectoring.

There are several strategies to deal with the bending oscillation. The first one is currently used by missile manufacturers and consists in filtering the input command to the actuator using a notch filter. This technique will be developed


 Figure 4.3: Root Locus of  $\frac{q_{83}}{\theta_{Tref}}$ 

further in the next subsection. Now that new sensors have been added on the airframe, the measurements they provide can be used to actively damp the bending oscillations. Feedback architectures based on the strain measurement, on pitch rate measurements and on the accelerometer measurements will be investigated in the following subsections.

#### 4.3.1 Notch Filtering

A notch filter is applied to the command of the thrust vectoring. This filter will remove any signal of the bending mode frequency. The first step is to choose an appropriate type of filter. A Chebyshev Type II filter suits the problem because there is no ripple in the bandwidth that could create gain distortion and affect performance at low frequency. However, this type of filter requires a high order denominator to ensure a sharp gain loss. The filter center frequency is set to 20Hz with a stop-band bandwidth of  $\pm 10\%$ . Indeed, the uncertainty on the first bending mode frequency is about  $\pm 10\%$ . The gain loss is set to 40 dB. The order of the filter is 4. With these criterion, the corresponding Chebyshev Type II filter is

$$N(s) = \frac{s^4 + (3.19 \cdot 10^4) s^2 + 2.49 \cdot 10^8}{s^4 + 239.0 s^3 + (6.04 \cdot 10^4) s^2 + (3.77 \cdot 10^6) s + 2.49 \cdot 10^8}$$

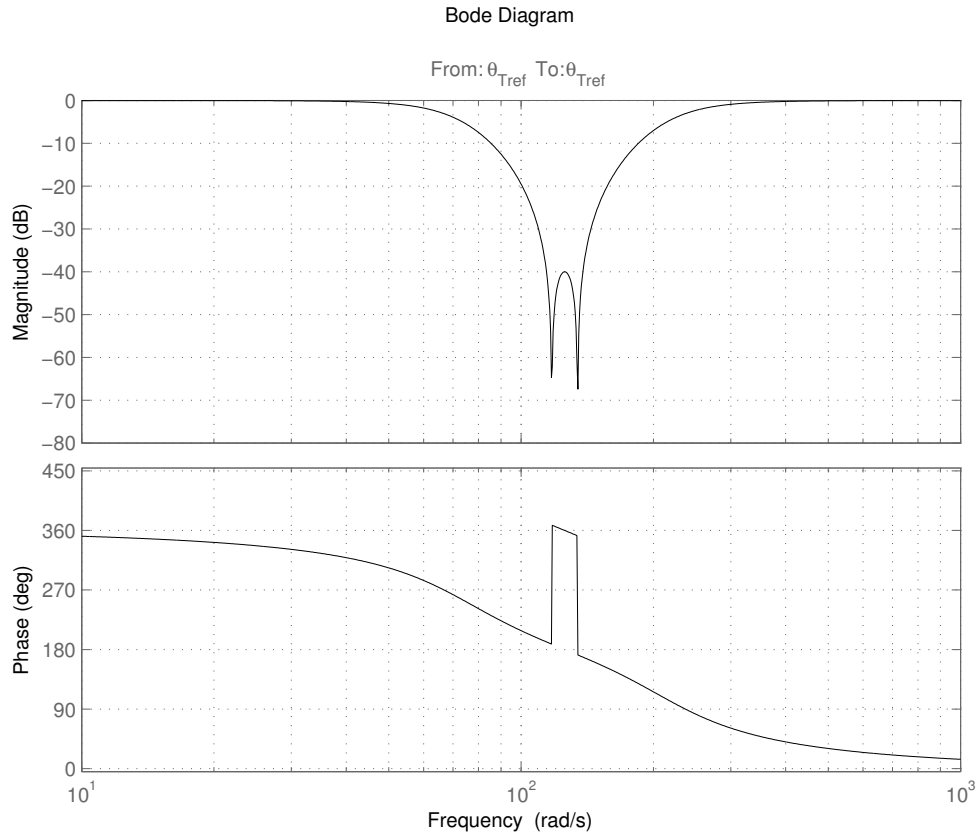


Figure 4.4: Bode Diagram of the Notch Filter

The Bode diagram of the filter is plotted on Figure 4.4. The phase loss brought by this notch filter is already  $-100^\circ$  at  $70 \text{ rad.s}^{-1}$  that may bring poorer performance even at low frequencies. A higher order notch filter could also be chosen to obtain a sharper band-stop.

Thanks to this filter, the actuator avoids exciting the first bending mode and bending oscillations will not generate parasitic actuations. The bode diagram of  $\frac{q_{83}(s)}{\theta_{Tref}(s)}$  is plotted on Figure 4.5. This shows clearly that the resonance peak of the first bending mode has been cut down by  $40 \text{ dB}$ .

Once the filter is plugged to the system input, a conventional pitch rate feedback with a proportional integral controller on the acceleration can be designed. The new feedback architecture is drawn on Figure 4.6.

### 4.3.2 Active Structural Damping

The notch filter is a simple solution to deal with vibrations but it does not remove them. Another way to overcome bending oscillations is to artificially augment the damping ratio of the bending mode. This is called active structural damping.

### 4.3. VIBRATIONS ALLEVIATION

---

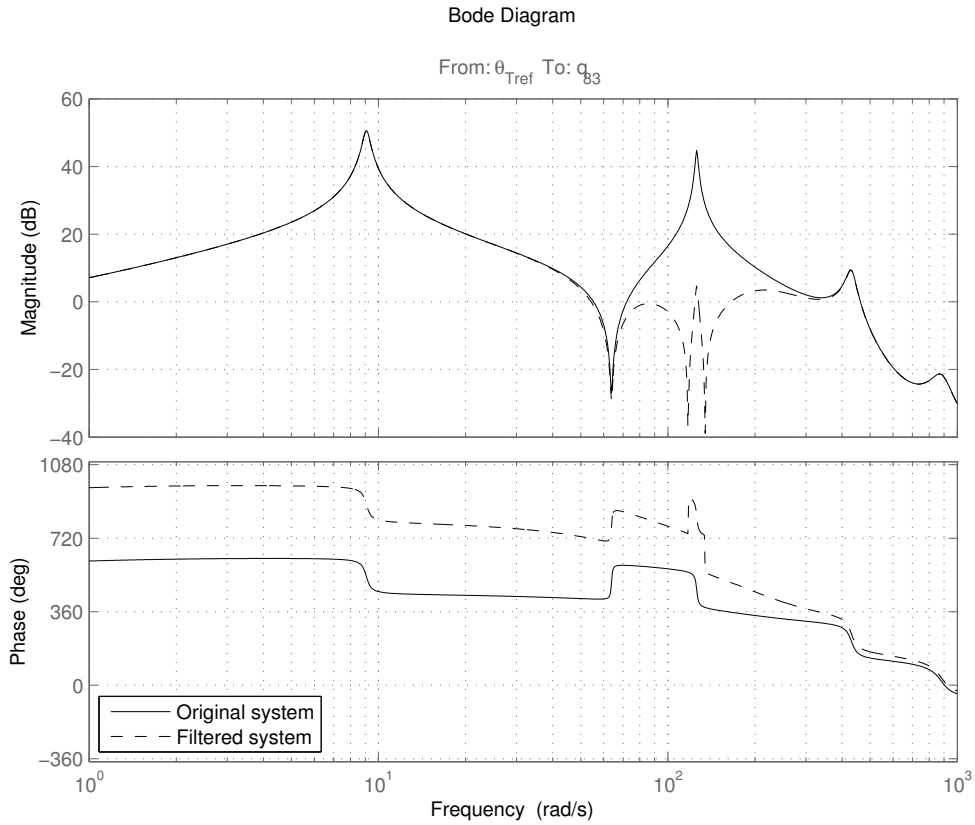


Figure 4.5: Bode Diagram of  $\frac{q_{83}(s)}{\theta_{Tref}(s)}$

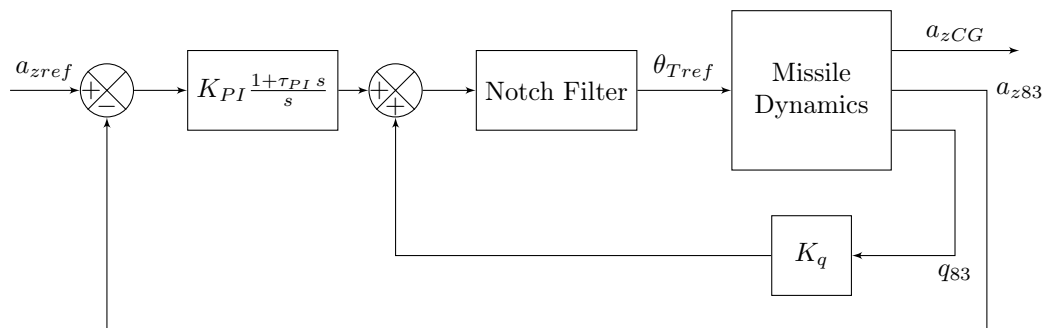


Figure 4.6: Closed-Loop with Notch Filter

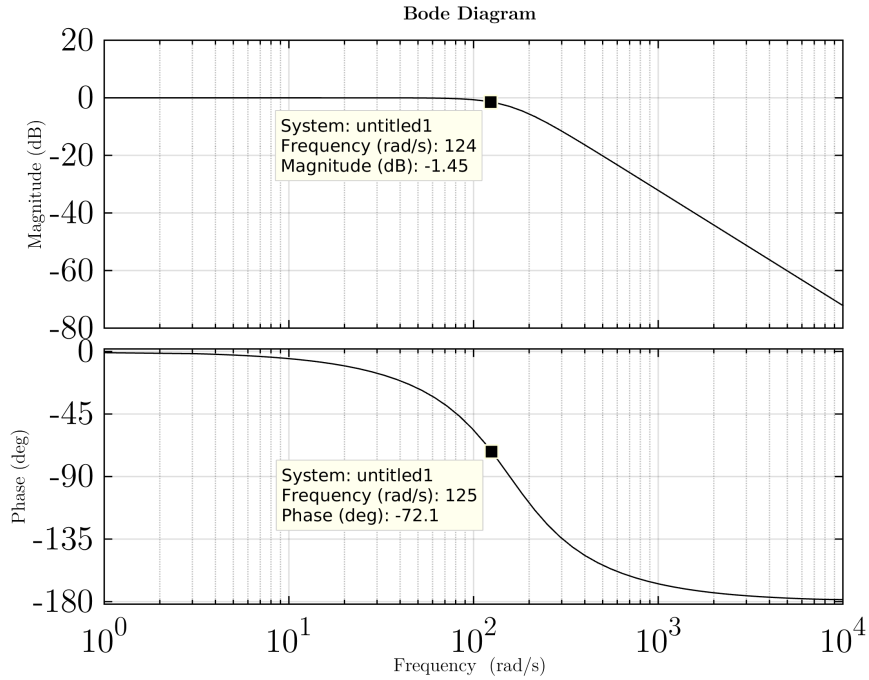


Figure 4.7: Bode Diagram of  $\frac{\theta_T(s)}{\theta_{Tref}(s)}$

#### 4.3.2.1 Requirements

The controller must generate a force that is opposite to the vibration speed to damp the bending oscillations. To do so, the controller can either use the thrust vectoring or the central fins. The natural frequency of the first mode is 20Hz. The bandwidth of the thrust vectoring is about 25Hz which is too low: at 20Hz, the thrust vectoring actuator has a phase loss of  $-70^\circ$  and a gain loss of  $-1.5\text{dB}$  as shown on Figure 4.7. This is very close to the cutoff frequency and the real behaviour of the actuator at this frequency is not accurately modeled.

The fins have a bandwidth of 50Hz that is more than the double of the bending mode frequency. The phase loss at 20Hz is only  $-34^\circ$  and the gain loss is  $-0.1\text{dB}$  as shown on Figure 4.8. Therefore this fast actuator is to be preferred for active damping of the first bending mode. Moreover, the fins are located in the middle where the flexure is important therefore they have an important controllability of the first bending mode. Also, at the first bending mode frequency, the fins deflection have very little influence on the slow rigid-body dynamics. Moreover, they are located close to the center of gravity so they do not create a big change in the angle of attack. The fins will be used to actively damp the bending vibrations.

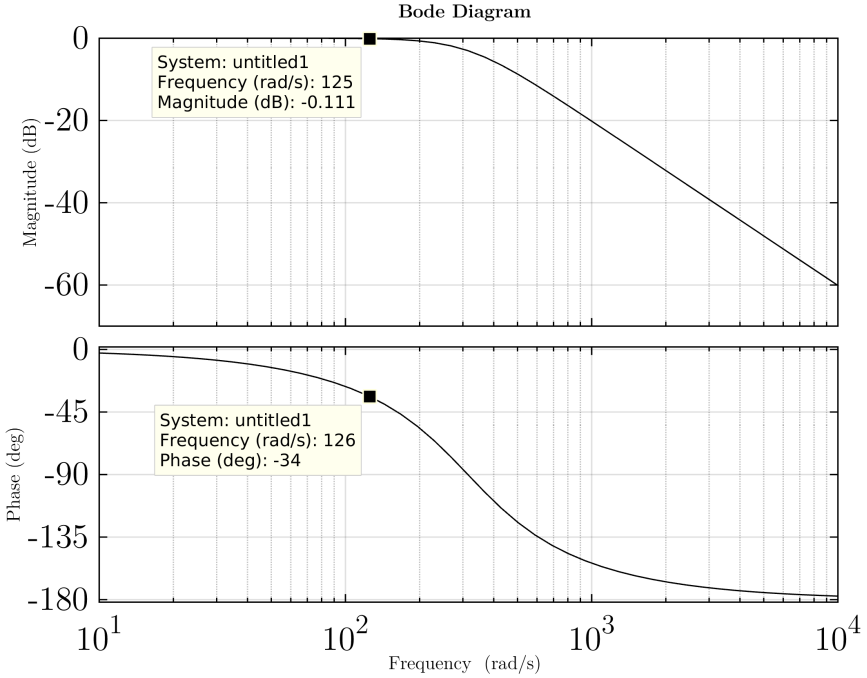


Figure 4.8: Bode Diagram of  $\frac{\delta_F(s)}{\delta_{Fref}(s)}$

#### 4.3.2.2 Strain Feedback

The strain gauge is a sensor that is usually not present on a missile airframe. With this extra sensor, it is possible to measure the local strain on the skin of the structure to infer on its flexure. This additional information can help to deal with bending oscillation. If only the first bending mode is considered, the transfer function of the fins deflection to the strain can be approximated to:

$$\frac{\varepsilon_{46}}{\delta_F}(s) = K_{\varepsilon/\delta_F} \frac{\omega_1^2}{s^2 + 2\zeta_1\omega_1 s + \omega_1^2}$$

To increase the term  $\zeta_1$  with a simple feedback, the strain measurement needs to be derivated as shown in the block diagram in Figure 4.9. The transfer function of the closed-loop would then be

$$\left( \frac{\varepsilon_{46}}{\delta_F} \right)_{CL}(s) = K_{\varepsilon/\delta_F} \frac{\omega_1^2}{s^2 + 2(\zeta_1 + \frac{1}{2}K_{\varepsilon/\delta_F}\omega_1 K_\varepsilon)\omega_1 s + \omega_1^2}$$

The feedback gain  $K_\varepsilon$  directly changes the damping ratio of the first bending mode without changing the static gain  $K_{\varepsilon/\delta_F}$  or the natural frequency  $\omega_1$ . However this feedback is non causal and a pole needs to be added. This artificial pole can be placed very fast to minimize its influence on the dynamics. The feedback

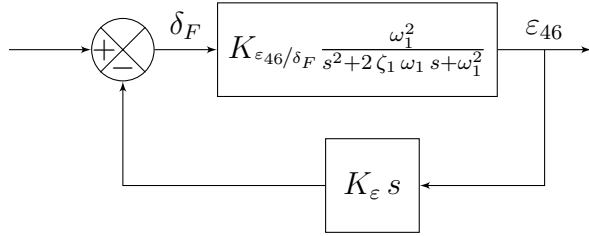


Figure 4.9: Block Diagram of Derivative Strain Feedback

transfer function would then be

$$K_\varepsilon \frac{s}{1 + s/\omega_{fast}}$$

This feedback loop would work if the fins actuator was very fast. This is not the case because even if its bandwidth is twice bigger than the bending mode natural frequency, the phase loss is non negligible as shown in 4.3.2.1.

Fortunately with this phase shift a simple proportional feedback will damp the bending oscillations. On Figure 4.10, a root locus has been plotted with the full dynamics of all 5 bending modes, flight dynamics and actuator dynamics. With a proportional feedback gain of 600, the damping ratio of the first bending mode has been increased by 10 to 12.5%. This gain is chosen to obtain a gain margin of 6dB and a phase margin of 30°.

With this first loop, the bode diagram of  $\frac{q_{83}}{\theta_{Tref}}(s)$  on Figure 4.11 shows that the first bending mode is clearly damped. The resonance peak at  $125 \text{ rad.s}^{-1}$  has been cut down thoroughly by 20 dB.

This active damping replaces the notch filter seen in 4.3.1 on page 64. The complete feedback architecture containing the strain feedback, the pitch rate loop and the proportional integrator corrector is on Figure 4.12.

This feedback architecture has some disadvantages though. The strain measured is not only coming from bending deformations. Some longitudinal or twisting modes may create local strains and propagate noise in the system. Moreover, without an appropriate band-pass filter, the static bending will create a static deflection of the fins and increase drag.

### 4.3.2.3 Gyroscope Feedback

Two gyroscopes can give information on the flexure. A gyroscope is placed at the rear and the other one is the gyroscope included in the sensor pack next to the nose. The problem with damping bending with gyroscopes is that they measure not only the local pitch rate of the bending but also the rigid-body pitch rate. Thus two of them are needed to subtract the rigid-body pitch rate. Indeed, a gyro at node  $i$  will measure  $q_i = q_{RB} + q_{FBi}$ . The subtraction of the signals coming from the two gyroscopes will give:

### 4.3. VIBRATIONS ALLEVIATION

---

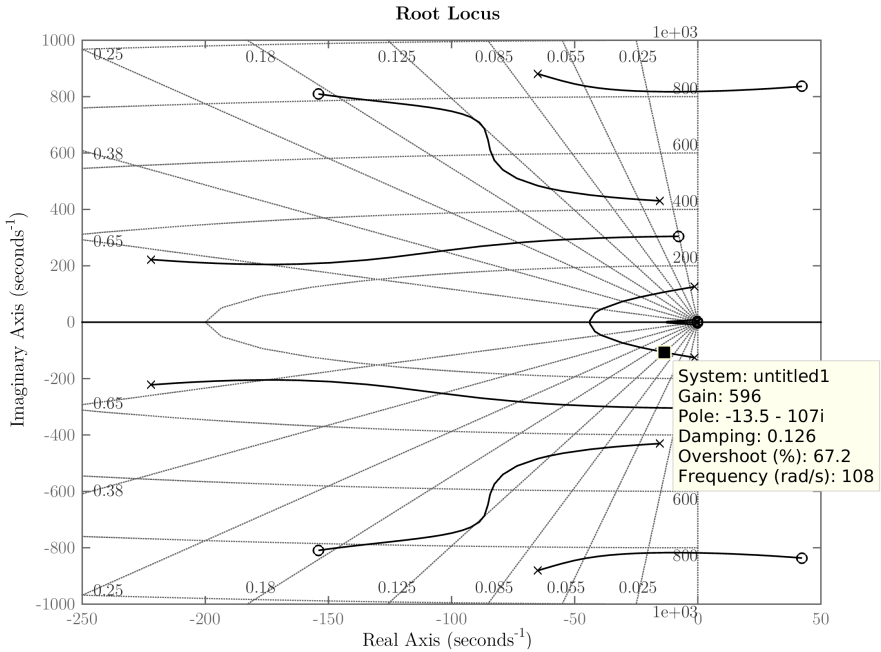


Figure 4.10: Root Locus of  $\frac{\varepsilon_{46}}{\delta_{Fref}}(s)$

$$q_{10} - q_{83} = q_{fb,10} - q_{fb,83} = \Delta q$$

If only the first bending mode is considered, the transfer function of the fins deflection  $\delta_F$  to the pitch rate difference  $\Delta q$  is

$$\frac{\Delta q}{\delta_F}(s) = K_{\Delta q/\delta_F} \frac{\omega_1^2 s}{s^2 + 2 \zeta_1 \omega_1 s + \omega_1^2}$$

thus with a simple proportional feedback gain  $K_{\Delta q}$  from  $\Delta q$  to  $\delta_F$  would modify the transfer function to

$$\left( \frac{\Delta q}{\delta_F} \right)_{CL}(s) = K_{\Delta q/\delta_F} \frac{\omega_1^2 s}{s^2 + 2 \left( \zeta_1 + \frac{1}{2} K_{\Delta q/\delta_F} \omega_1 K_{\Delta q} \right) \omega_1 s + \omega_1^2}$$

This feedback would damp the first bending mode without modifying the other parameters. Now considering the phase loss of the actuator of about  $30^\circ$ , the natural frequency of the first bending mode will change but damping is still possible. On Figure 4.13 the root locus of  $\frac{\Delta q}{\delta_{Fref}}(s)$  shows that a damping of 12% on the first bending mode can be achieved with a feedback gain  $K_{\Delta q} = 0.24$ .

The effect of this loop on the resonance peak of the first bending mode can be seen on Figure 4.14. The resonance peak is reduced by 20 dB.

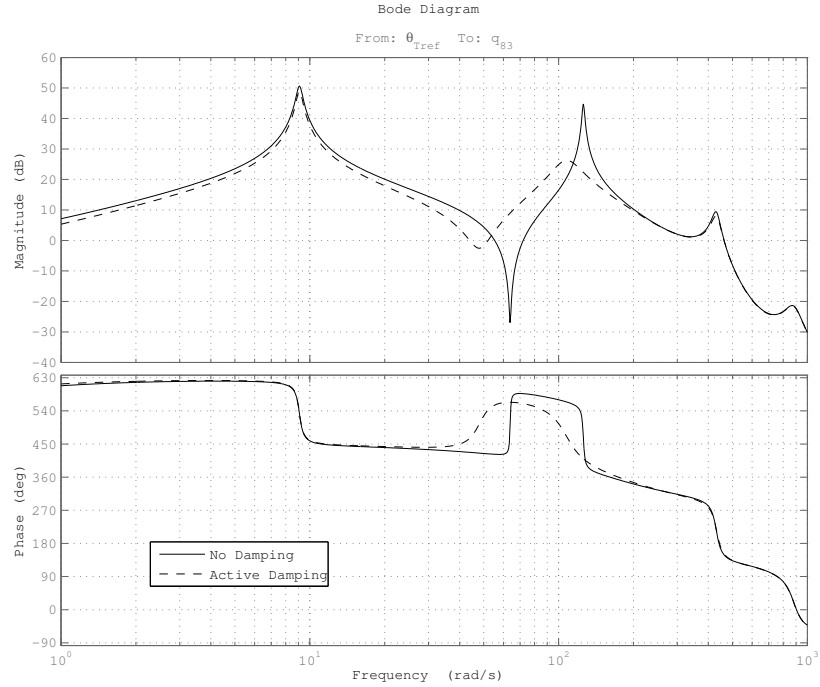


Figure 4.11: Bode of  $\frac{q_{83}}{\theta_{Tref}}(s)$  With and Without Strain Feedback

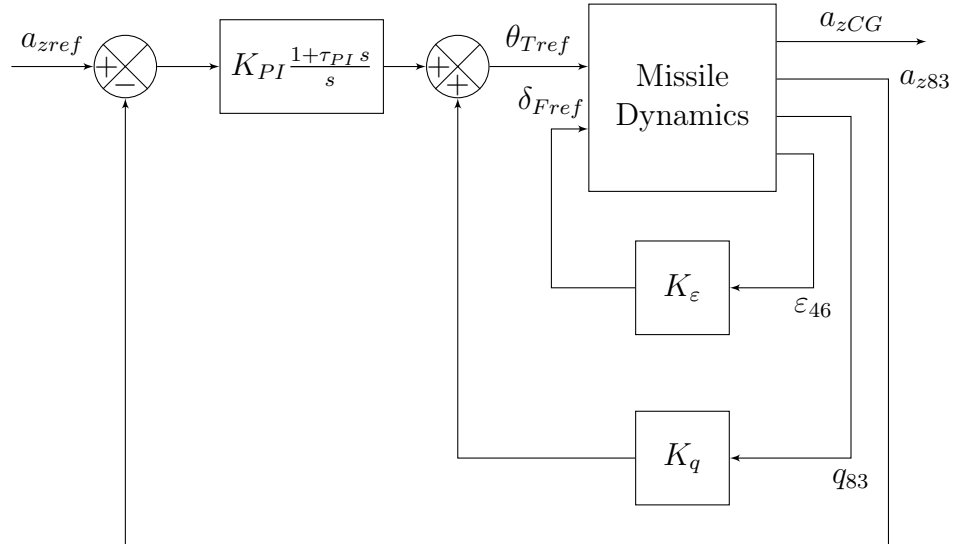


Figure 4.12: Feedback Architecture with Strain Gages

### 4.3. VIBRATIONS ALLEVIATION

---

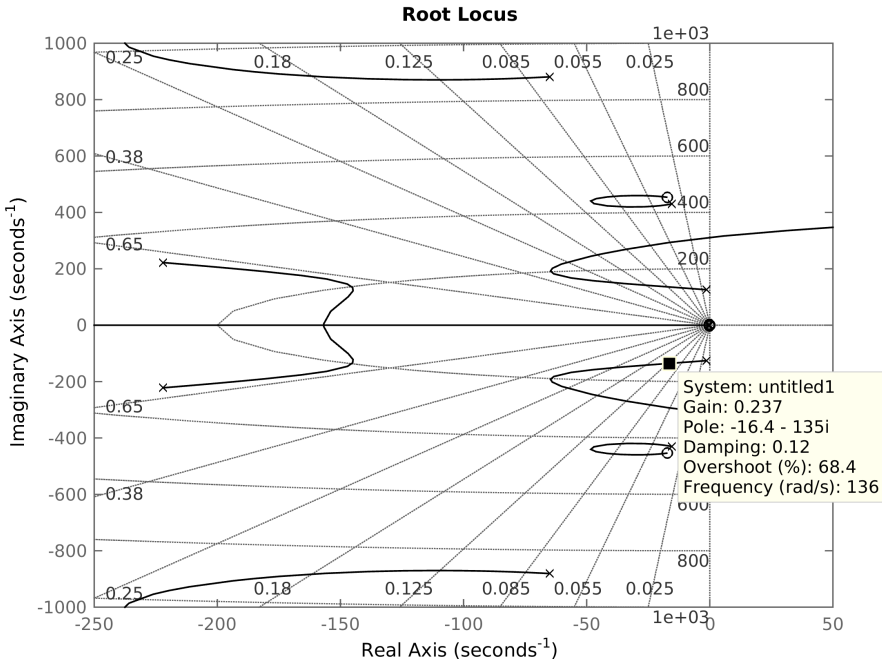


Figure 4.13: Root Locus of  $\frac{\Delta q}{\delta_{F_{ref}}}(s)$

To this damping loop are added the conventional feedbacks on the pitch rate and the lateral acceleration. The complete architecture in this case is draw on Figure 4.15.

This controller architecture has the disadvantage that the two gyroscopes must be similarly calibrated and synchronized to perform the subtraction correctly. The great advantage is the absence of fins deflection in static.

#### 4.3.2.4 Accelerometer Feedback

Using accelerometers for the feedback is more complicated than using gyroscopes. At node  $i$ , the accelerometer will measure  $a_{z,i} = a_{z,CG} + (x_{CG} - x_i) \dot{q} + a_{zi,fb}$ . There are three unknowns in this equality:  $a_{z,CG}$ ,  $\dot{q}$ , and  $a_{zi,fb}$  hence three uncorrelated accelerometers are needed to keep only the flexible body component. On the airframe, three accelerometers have been added at node 10, 53 and 92. Considering only the first bending mode, all the  $a_{zi,fb}$  are proportional to the first bending mode mean acceleration  $a_{z,m1}$ . A linear combination of these three measurements must be found so that it does not depend of  $a_{z,CG}$  and  $\dot{q}$ . Let  $(c_{10}, c_{53}, c_{92})$  be three coefficients so that

$$c_{10}a_{z,10} + c_{53}a_{z,53} + c_{92}a_{z,92} = c a_{z,m1}$$

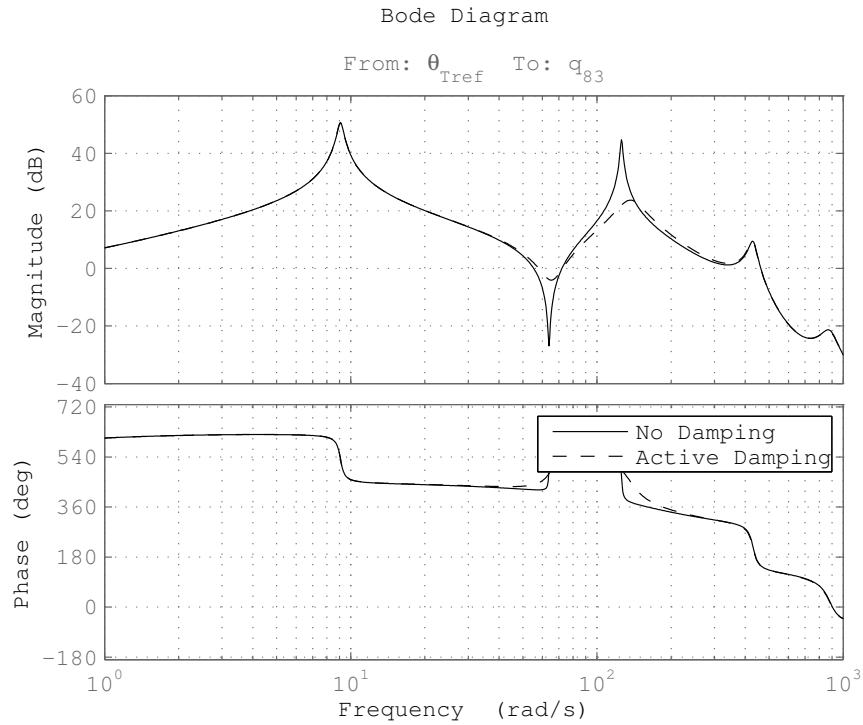


Figure 4.14: Bode of  $\frac{q_{83}}{\theta_{Tref}}(s)$  With and Without  $\Delta q$  Feedback

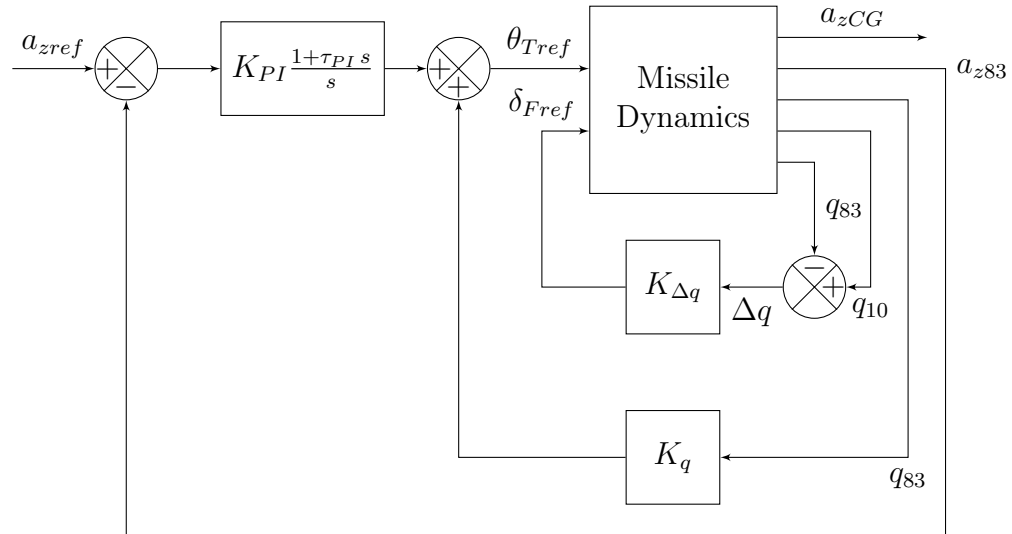


Figure 4.15: Feedback Architecture with Gyroscopes

where  $c$  is a non zero real number. Let say that  $c_{10} = 1$  to make the linear system of Cramer. In a matrix form, this gives

$$\begin{bmatrix} 1 & 1 & 1 \\ 9 & 52 & 91 \\ 1 & 0 & 0 \end{bmatrix} \begin{bmatrix} c_{10} \\ c_{53} \\ c_{92} \end{bmatrix} = \begin{bmatrix} 0 \\ 0 \\ 1 \end{bmatrix}$$

The solution is  $\begin{bmatrix} c_{10} \\ c_{53} \\ c_{92} \end{bmatrix} = \begin{bmatrix} 1 \\ -82/39 \\ 43/39 \end{bmatrix}$ . The linear combination  $c_{10}a_{z,10} + c_{53}a_{z,53} + c_{92}a_{z,92}$  will be called  $\sum a_z$ .

The transfer function of the fins deflection to this linear combination of accelerations is of the form

$$\frac{\sum a_z}{\delta_F}(s) = K_{\sum a_z/\delta_F} \frac{\omega_1^2 s^2}{s^2 + 2\zeta_1 \omega_1 s + \omega_1^2}$$

hence to damp the first bending mode, the feedback needs an integrator so that the resulting transfer function would be

$$\frac{\sum a_z}{\delta_F \text{ CL}}(s) = K_{\sum a_z/\delta_F} \frac{\omega_1^2 s^2}{s^2 + 2(\zeta_1 + K_{\sum a_z/\delta_F} \omega_1 K_{a_z}) \omega_1 s + \omega_1^2}$$

Like for the gyroscopes, the phase loss of the fins actuator will generate a change in the bending oscillation natural frequency. The root locus of  $\frac{1}{s} \frac{\sum a_z}{\delta_F}$  is plotted on Figure 4.16 and shows that the first bending mode can be damped to 12% with a gain  $K_{a_z}$  of 0.16.

A comparative Bode plot shows on Figure 4.17 the effect of such a damping architecture. Once again the resonance peak has been cut off.

The complete controller architecture is drawn in Figure 4.18.

Using accelerometers for structural damping might bring some problems because the accelerometers must be similarly calibrated and synchronized like the gyroscopes. The position of the center of gravity does not need to be known. Indeed when the linear equation system has been solved, the solution do not depend on the center of gravity location. The integration will reduce parasitic actuation of the fins due to noise at high frequency.

## 4.4 $H_\infty$ Fixed-Structure Tuning

Four controller architectures will be assessed. They all have in common the lateral acceleration control composed of a pitch rate feedback and a proportional integral controller on the lateral acceleration. The first architecture has a notch filter. The controller number 2 to 4 use active damping with respectively:

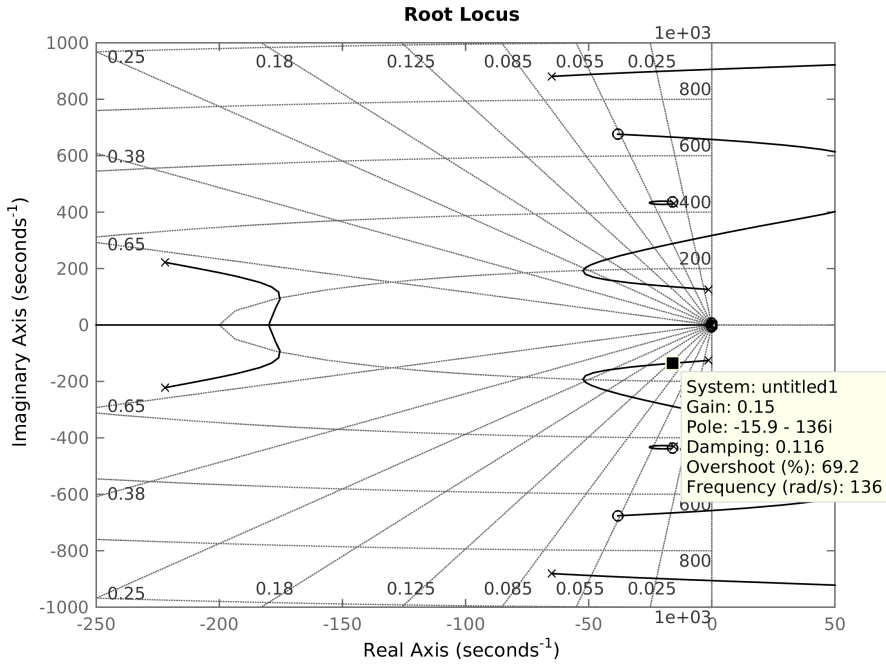


Figure 4.16: Root Locus of  $\frac{1}{s} \frac{\sum a_z}{\delta_{Fref}}(s)$

- the strain gauge feedback,
- the 2 gyroscopes feedback,
- the 3 accelerometers feedback.

These controllers will be respectively denoted “Notch”, “Strain”, “Gyro” and “Acc”.

These architectures will be tuned using the same criterion to eventually compare their performance. The method will use the  $H_\infty$ -tuning for fixed-structure controllers developed by P. Apkarian in [20].

Each architecture is put in a weighted form like on Figure 4.19. The input to the closed-loop system is the exogenous vector  $w$  which contains all the inputs like noises, perturbations or references. The output is the performance vector  $z$  containing all the performance indices that one will minimize. The diagonal matrices  $W_{in}$  and  $W_{out}$  are weights applied to  $w$  and  $z$  to define the requirements. The algorithm will tune the controller gains in order to make the system stable while minimizing  $\gamma$  such that

$$\|W_{out} H W_{in}\|_\infty < \gamma$$

The parameters subject to tuning are  $K_q$ ,  $K_{PI}$  and  $\tau_{PI}$ . The notch filter, the strain feedback, the gyroscopes feedback or the accelerometers feedback are not tunable. They are defined in 4.3 on page 63.

#### 4.4. $H_\infty$ FIXED-STRUCTURE TUNING

---

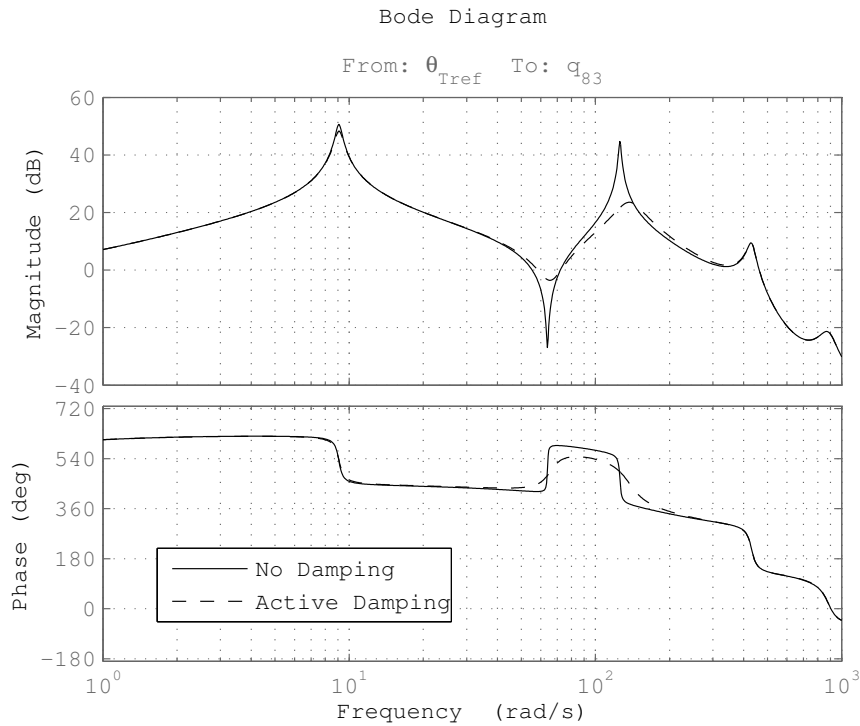


Figure 4.17: Bode of  $\frac{q_{83}}{\theta_{Tref}}(s)$  With and Without  $\sum a_z$  Feedback

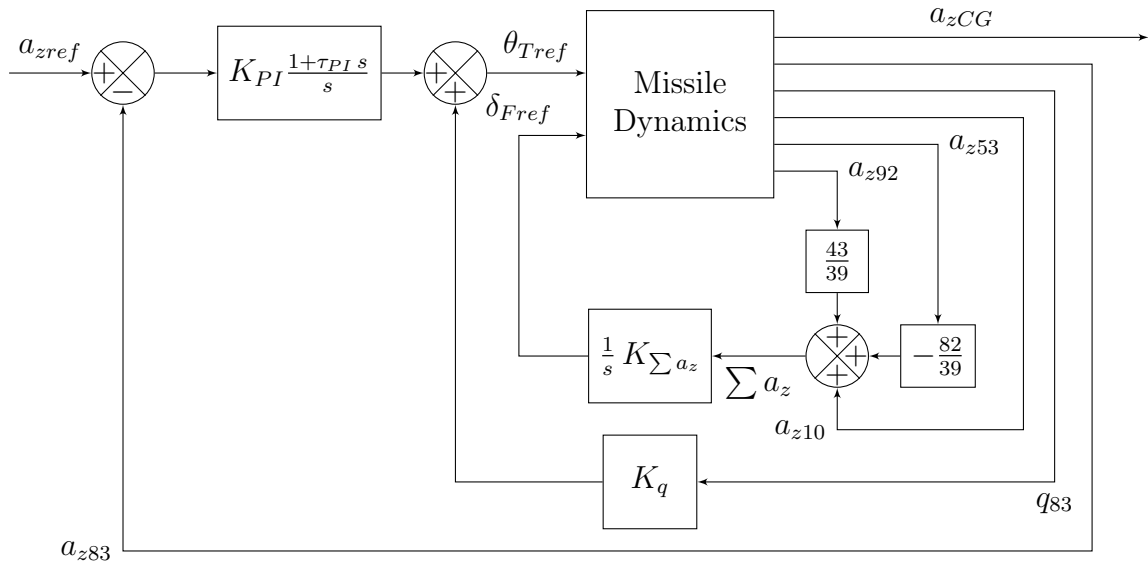


Figure 4.18: Feedback Architecture with Accelerometers

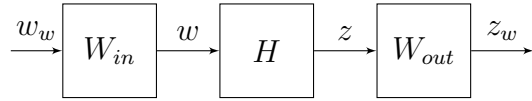


Figure 4.19: Weighted Form for  $H_\infty$ -tuning

The exogenous vector  $w$  only contains the reference lateral acceleration  $a_{zref}$ . The corresponding weight is set to 1. Thus, the other signals weights will be chosen according to a reference acceleration of  $1 \text{ m.s}^{-1}$ . Additional inputs are not needed, first of all because the tuning needs to be simple but also because other inputs like noise, actuators perturbations or gust perturbations are neglected. The sensors noise is very low compared to signals generated by vibrations. The fins actuator perturbations is assumed to be very few compared to the thrust vectoring perturbations which will not be considered for tuning but later for assessment. Finally, gusts have a speed which is negligible compared to the missile speed of Mach 2.

The performance vector  $z$  is composed of two signals: the lateral acceleration error  $a_{zref} - a_{zCG}$  and the thrust vectoring orientation  $\theta_T$ . It is obvious that the lateral acceleration error is needed in  $z$  to design a lateral acceleration controller. The thrust vectoring orientation  $\theta_T$  is added in  $z$  to limit the use of this actuator which has a rate limit, a deflection limit and second-order dynamics. The output weight matrix  $W_{out}$  is then

$$\begin{bmatrix} W_{err} & 0 \\ 0 & W_{\theta_T} \end{bmatrix}$$

$W_{err}$  is set to minimize the error at low frequency and bound it at high frequency for resonance reduction. The controller is equipped with an integrator so the error will tend to 0. An empirical tuning of this weight is

$$W_{err}(s) = \frac{5}{s} \left( \frac{s}{10} + 1 \right)$$

which will force the bandwidth to be 5 rad/s. And the maximum error will be 2 times the reference acceleration. The target shape of  $H_{a_{zref} \rightarrow (a_{zref} - a_{zCG})}(s)$  will be the inverse of  $W_{err}(s)$  and is plotted in Figure 4.20.

$W_{\theta_T}$  is chosen avoid using the actuator over its cutoff frequency. A simple way to do this is to chose

$$W_{\theta_T}(s) = 2 \cdot 10^{-3} \left( \frac{s}{\omega_T} \right)^2 \left( \frac{1}{1 + 10^{-5}s} \right)^2$$

where  $\omega_T$  is the thrust vectoring cutoff frequency of 25Hz (157 rad/s). The coefficient  $2 \cdot 10^{-3}$  is empirically set. To have a causal weight, two fast poles are added. Once again, the target shape of  $H_{a_{zref} \rightarrow \theta_T}(s)$  is  $1/W_{\theta_T}(s)$ . The rotation speed of

#### 4.4. $H_\infty$ FIXED-STRUCTURE TUNING

---

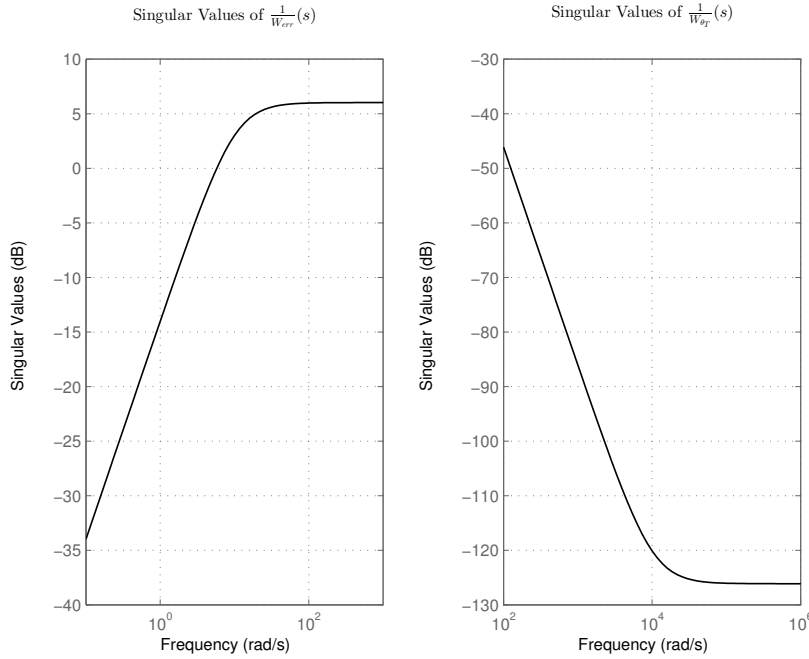


Figure 4.20: Singular Values of  $1/W_{err}(s)$

Controller	$K_q(s)$	$K_{PI}(\text{rad}\cdot\text{s}/m)$	$\tau_{PI}(s)$
Notch	$9.47 \cdot 10^{-2}$	$9.46 \cdot 10^{-3}$	0.171
Strain	$9.98 \cdot 10^{-2}$	$13.0 \cdot 10^{-3}$	0.122
Gyro	$8.40 \cdot 10^{-2}$	$9.11 \cdot 10^{-3}$	0.149
Acc	$8.38 \cdot 10^{-2}$	$9.05 \cdot 10^{-3}$	0.151

Table 4.1:  $H_\infty$ -tuned Controllers Parameters

the thrust vectoring must also be bounded. The system being linear, trying to minimize  $\theta_T$  will also minimise  $\dot{\theta}_T$ . The corresponding bound will be  $s/W_{\theta_T}$

The  $H_\infty$ -tuning yields parameters summarized in Table 4.1. The algorithm found a minimum  $\gamma$  between 1.01 and 1.04 for all of them.

These settings in Table 4.1 are very similar especially for the controllers alleviating vibrations. These controllers will be assessed and compared in the Section 4.5.

Parameter	Uncertainty
Thrust magnitude $T_0$	$\pm 10\%$
Center of gravity location $x_{CG}$	0 to $+ 10\%$
$i^{th}$ bending mode frequency $\omega_i$	$\pm 10\%$
$i^{th}$ bending mode damping ratio $\zeta_i$	$\pm 20\%$

Table 4.2: Parameters Uncertainty

## 4.5 Controllers Assessment and Comparison

### 4.5.1 Robustness to Uncertainty

The first criteria to assess is robustness to uncertainty. The  $H_\infty$  algorithm found stable solutions for the five architectures but they can turn unstable with some parameters variation.

The uncertainty has been defined considering the thrust, the center of gravity, the bending modes natural frequencies and their damping ratios as uncertain parameters. The thrust is generated by the rocket engine and is then very uncertain. The center of gravity moves along the flight because of the propellant combustion. Finally the bending modes natural frequency and especially damping are often poorly identified and they vary. These parameters uncertainties are summarized in Table 4.2. Other parameters could also be defined as uncertain like the actuators bandwidth, the modes shapes, the aerodynamic coefficients and so on but this should require a specific study.

To assess robustness, gain margin and phase margin are of little help for such a MIMO system. Each uncertain system is an infinite set of possible realization. A finite subset of systems is created from this uncertain system and their poles are plotted on Figure 4.21. The poles keep a reasonable margin with the imaginary axis. These closed-loop systems are robust to the designed uncertainty.

### 4.5.2 Tracking

The tracking performance of these 4 closed-loop is their ability to generate a lateral acceleration equal to the reference acceleration. Step responses give a good insight to assess the tracking performance. These responses are plotted on Figure 4.22.

Another index for tracking performance is the singular values of the transfer function from the reference acceleration  $a_{zref}$  and the error  $a_{zref} - a_{zCG}$  which is on Figure 4.23.

Looking at these too figures, the four different closed-loop architectures yield very similar tracking performance. The rise time from 10 to 90% following a step demand is between 0.214 and 0.227 s and the 2% settling time is between 0.400

## 4.5. CONTROLLERS ASSESSMENT AND COMPARISON

---

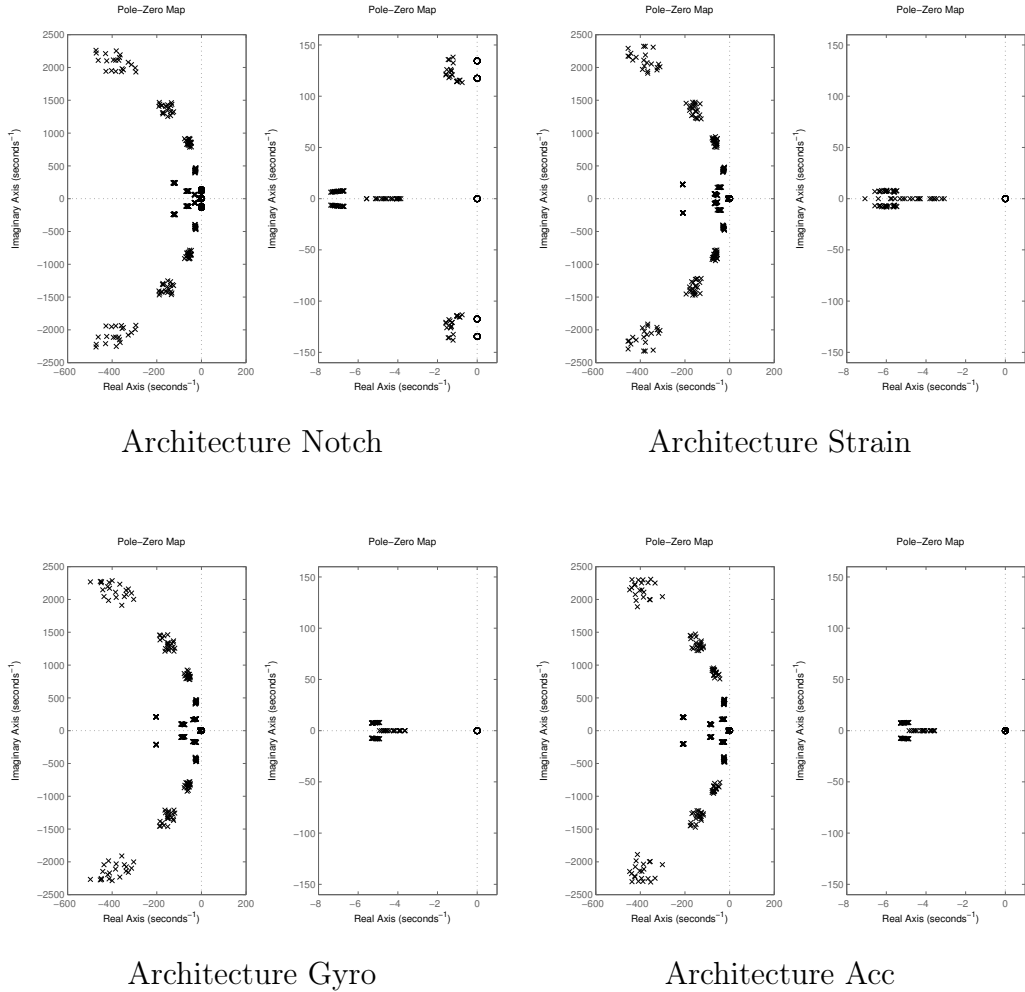
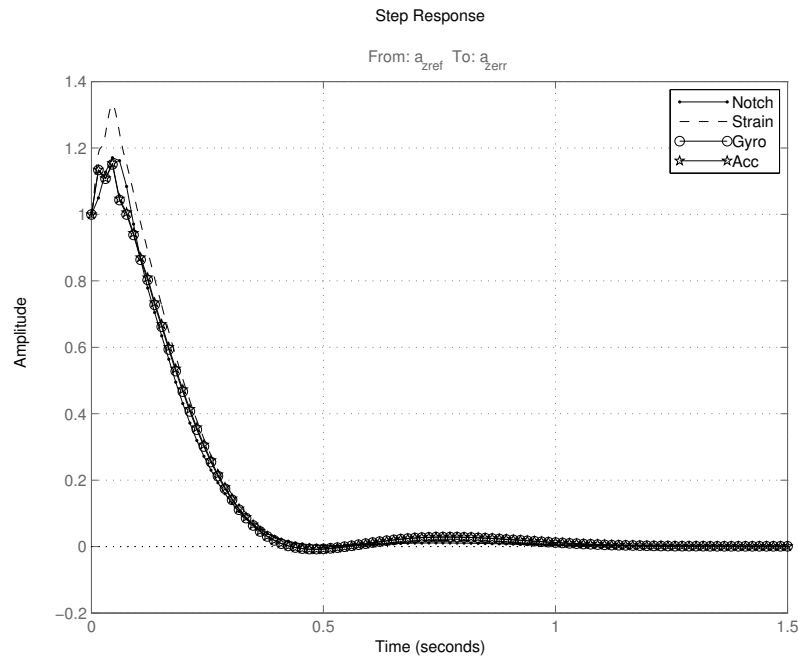
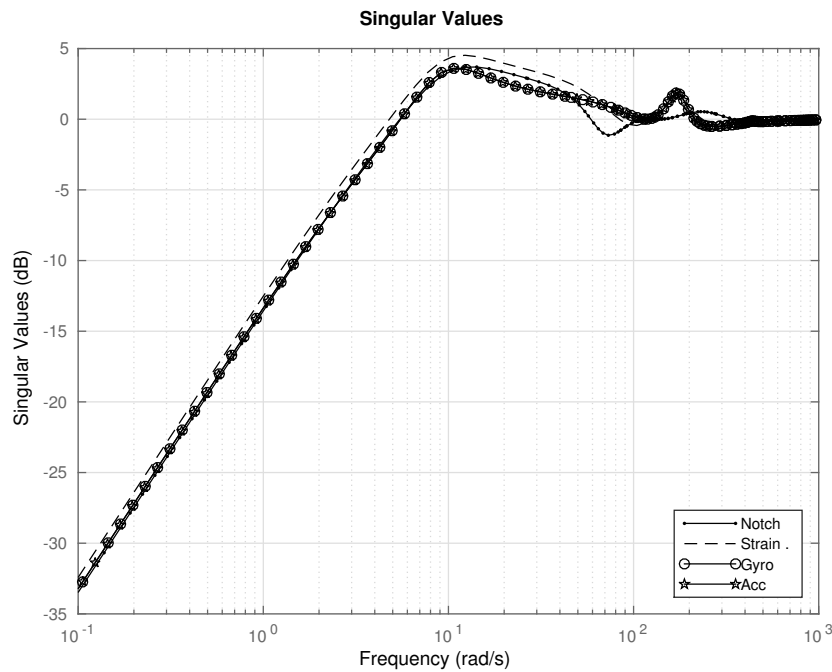
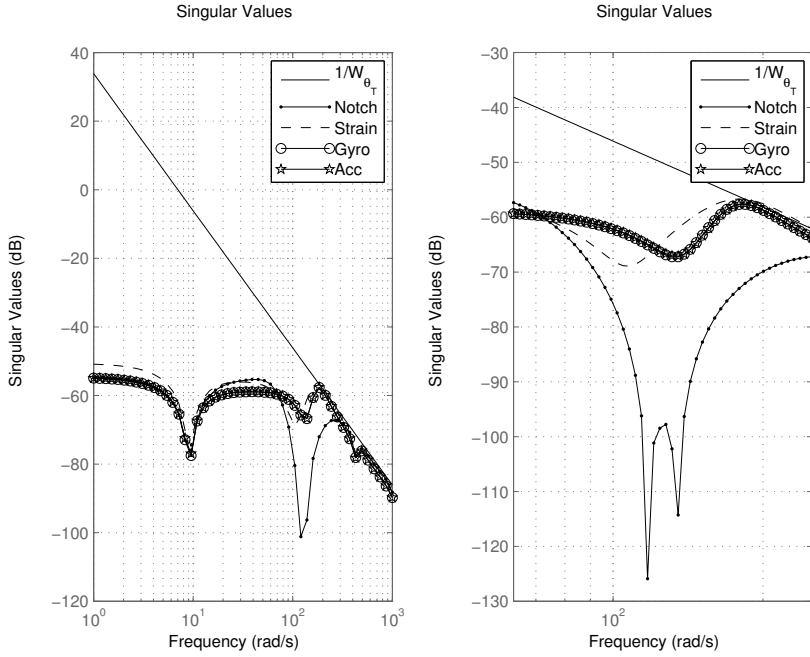


Figure 4.21: Poles of Closed Loop 1 to 4 Subject to Uncertainty


 Figure 4.22: Step Response of  $a_{zref}$  to  $(a_{zref} - a_{zCG})$ 

 Figure 4.23: Sigma Plot of  $a_{zref}$  to  $(a_{zref} - a_{zCG})$


 Figure 4.24: Singular Values of  $a_{zref}$  to  $\theta_T$ 

and  $0.406\text{ s}$ . The sigma plots provide information about tracking performance over all frequencies. The presence of an integrator in the loop gives makes the error converge to zero at low frequencies. The bandwidth at -3dB is between  $3.2$  and  $3.7\text{ rad.s}^{-1}$ .

### 4.5.3 Actuators Demand

The thrust nozzles cylinders and the fins actuators have second order dynamics and actuators demand must be limited at high frequency. These demands must also be limited over the whole range of frequencies to save energy and to avoid actuators heating and damage.

#### 4.5.3.1 Demand for Lateral Acceleration

The actuators demand following a lateral acceleration command must be appropriately bounded. The weight  $W_{\theta_T}$  ensures that the position and rate of the thrust vectoring stays bounded under a reasonable threshold. The thrust vectoring demand is plotted on Figure 4.24 with respect to frequency.

None of these four architectures cross the threshold imposed by  $1/W_{\theta_T}$ . The “Notch” architecture has a thorough stop-band around the 1st bending mode natural frequency of  $125\text{ rad/s}$ . The three active damping architectures keep a satisfactory margin. Similarly for the fins actuator, Figure 4.25 shows the fins deflection for the closed-loops performing active damping.

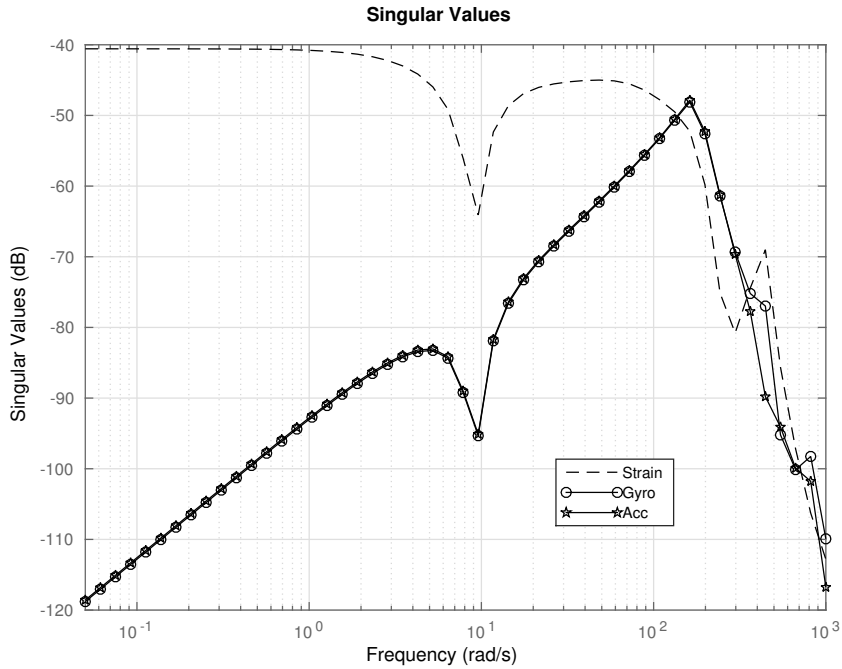


Figure 4.25: Singular Values of  $a_{zref}$  to  $\delta_F$

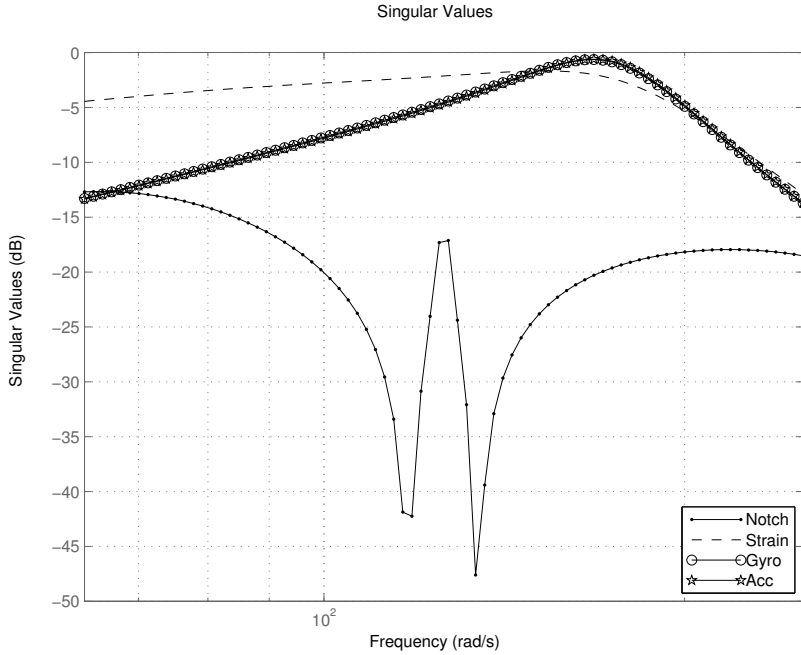
The “Strain” architecture generate greater commands on the fins deflection at frequencies under 100 rad/s compared to the “Gyro” and “Acc” architectures. These closed-loop do not generate fins deflection at high frequencies.

#### 4.5.3.2 Parasitic Effects

Bending vibrations are a source of parasitic actuations on the thrust vectoring. Indeed, the vibrations will generate parasitic signals in the sensors measurements then propagated through the controller and to the thrust vectoring. The bending vibrations are mostly generated by the rocket engine which thrust magnitude and orientation is very noisy. The parasitic actuations can be observed on the singular values from a perturbation on the thrust orientation to the actuated nozzles orientation on Figure 4.26. The “Notch” architecture suppresses this noise with the notch filter without removing the vibrations. The active damping architectures “Strain”, “Gyro” and “Acc” suppress the vibrations directly.

#### 4.5.4 Bending Reduction

In the previous section, it has been seen that an architecture with a notch filter or with active damping have similar tracking performance, and a good rocket engine noise rejection. The difference between them appears when it comes to dynamic bending reduction.


 Figure 4.26: Singular Values of  $\theta_{Tpert}$  to  $\theta_T$ 

#### 4.5.4.1 Vibrations Alleviation

The active damping architectures have the advantage of reducing bending vibrations. ASTER 30 sensors pack is equipped with several tracking and attitude control sensors. They are greatly sensitive to vibrations and filtering always brings delays. The active damping will thoroughly reduce vibrations and hence improve tracking and attitude control.

The rocket engine creating a noisy thrust is the main source of bending vibrations. The singular values of this propagation is shown on Figure 4.27 where  $\theta_{Tpert}$  is the noisy thrust deflection and  $a_{z83v}$  and  $q_{83v}$  are the vibration component of acceleration and pitch rate at sensors pack location. Indeed the first architecture “Notch” do nothing to reduce these vibrations whereas the other three “Strain”, “Gyro” and “Acc” cut them down strongly.

#### 4.5.4.2 Dynamic Stress Alleviation

By reducing bending oscillations, the active damping will also reduce stress due to dynamic deformations. The junction between the booster and the dart is located where the flexure due to the first bending mode is maximum. Therefore this link must be very stiff and resistant to flexure. With active damping, this link can be lightened and simplified. Figure 4.28 shows the strain reduction with active damping compared to non active damping next to the link. The source of vibrations is again the rocket engine thrust orientation noise.

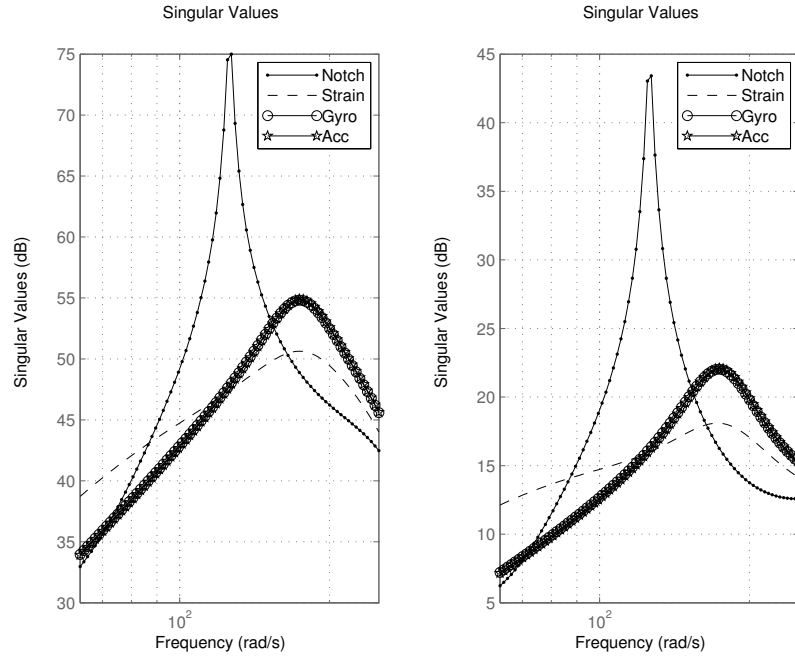


Figure 4.27: Singular Values of  $\theta_{Tpert}$  to  $a_{z83v}$  (left) and  $q_{83v}$  (right)

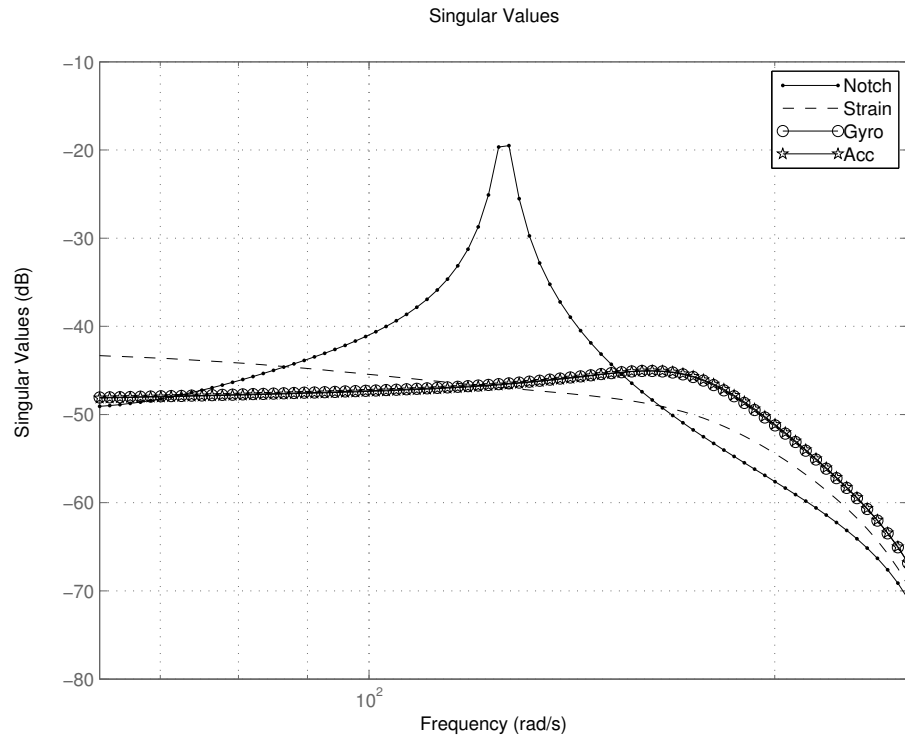


Figure 4.28: Singular Values of  $\theta_{Tpert}$  to  $\varepsilon_{46}$



# Chapter 5

## Results and Discussions

The thesis has investigated structural damping on a slender missile ASTER 30. A flight dynamics model has been derived coupled with a structural model. This flexible missile model is the foundation on which sensors have been placed at optimal locations for structural damping purposes. Several lateral acceleration controllers were created and assessed which three of them use active damping. These steps will be discussed recalling the assumptions made, the results obtained and their scope of validity.

**Flight Dynamics** The flight dynamics are based on a simple longitudinal model at Mach 2 and sea level. The aerodynamics modeling uses global linear aerodynamic coefficients that have been obtained from [2] and [18] with slight changes. Flight of slender bodies is generally highly nonlinear but for simplification purposes, it has been assumed linear. This might create inconsistencies at high angle of attack. The equations are therefore valid within very small variations from the trim state. However, the purpose of the study is to demonstrate the feasibility of active damping and not to accurately design a functional controller.

Only the SPPO is considered as a mode in this model. The reason for this is that slower dynamics like the phugoid have a time scale which belongs to navigation issue and not lateral acceleration generation. The SPPO natural frequency was calculated at ???Hz with a damping ratio of ??? which is realistic. The SPPO dynamics set a limit to the fastest response to generate lateral with the proposed feedback architecture.

**Actuators** ASTER 30 has two actuators to control the flight, thrust vectoring nozzles and fins. The transfer functions from the demanded angles of deflection of these actuators and the realised angles have been assumed to be of second order. This assumption might be a little extreme especially for the thrust vectoring which dynamic is very complex and non linear. Indeed the thrust magnitude is so intense that the nozzles might bend due to backlash.

---

**Structural Modeling** The missile has been modeled using a discretised method using point masses and massless beams. This structural stiffness of the beam has been estimated assuming that the missile skin is in carbon fibre and divided in two pipes of similar thickness but different diameters. The real structural composition of the missile is probably very different with anisotropic materials, variable thickness. The mass is not uniformly distributed as assumed. Of course knowing the exact mass distribution and structural stiffness, the model can be adapted to be more accurate. Also one assumption was that pure moments and rotational inertias are negligible which might be false especially at the fins location or about the missile warhead.

**Servo-aeroelastic Model** The final model of the missile takes account of the longitudinal flight dynamics, the actuators dynamics and the bending. Interactions between these three models are very limited since the structure deformation is only influenced by thrust vectoring and fins forces. The aerodynamics are supposed to bring no bending since the thrust is the main force. However, the source of vibrations is not important to be clearly identified as long as these vibrations are damped thoroughly. The controllers designed react to bending oscillations no matter where they come from. To model bending due to aerodynamics, it would have require to use data on local pressure coefficients all along the body which vary with angle of attack, pitch rate and are time varying. This would bring additional complexity that is not needed in this study.

On the other hand, the bending deformation is supposed to have no influence on the aerodynamics. Since the bending deflection is very limited, the shape of the missile does not change significantly and its flight characteristics remain unchanged.

**Sensors Placement** Additional sensors were placed all along the body. These sensors add information about the flexure of the missile to allow active damping. They were of three types: strain gauge, gyroscopes and accelerometers. Using the  $H_\infty$ -norm, an index has been defined to locate the best positions to place each sensor. It has been proved that one strain gauge is necessary but two gyroscopes and three accelerometers are need to have enough information on the missile bending. The optimal location for the strain gauge is in the middle of the missile. The gyroscopes must be placed at each extremity. Since a gyroscope is already present in the sensors pack, only one has been added on the tail. Finally, the accelerometers were placed at the tail, the middle and the nose. The accelerometer from the sensors pack of ASTER is located at an acceleration node of the first bending mode and has a very limited sensitivity of this state.

**Damping controllers** Three controllers have been designed with the measurements provided by the additional sensors. One uses the strain gauge, the second

Feedback Type	Tracking	Actuators Demand		Parasitic Actuation	Vibrations Damping	Stress Alleviation
		Nozzles	Fins			
Notch Filter	Correct	Limited	None	Limited	None	None
Strain Gauge Feedback	Correct	Limited	Medium	Limited	Increased	Increased
Gyrosopes Feedback	Correct	Limited	Low	Limited	Increased	Increased
Accelerometers Feedback	Correct	Limited	Low	Limited	Increased	Increased

Table 5.1: Summary of Controllers Performance

one uses the gyroscopes and the last one uses three accelerometers.

The first architecture is based on the phase loss of the fins actuator and can be faulty if the actuator is not properly modeled. Indeed if the actuator has a faster reaction time and the phase loss is close to  $0^\circ$ , the loop would increase the natural frequency of the bending mode and not damp it. The feedback uses the measurement from a single strain gauge. Since strain gauge are resistors, they are very sensitive to temperature and are not reliable. Moreover, they measure the local strain that can be due to other structural modes like twisting or longitudinal stretch and compression. The advantage is that they are very cost effective.

The second architecture requires the subtraction of two pitch rate measurements whereas the third one needs three accelerometers. The performance from both architectures is very similar however the gyroscopes feedback uses less the fins at low frequencies. The advantage of the accelerometers feedback is the use of an integrator that will minimize high frequency noise sent to the actuator. The use of gyroscopes must be preferred though because only one additional gyroscope is need whereas it is three for the accelerometers. Accelerometers also measure gravity and it must be removed using the attitude and gravity magnitude estimations which is a disadvantage compared to gyroscopes.

It has been shown that these three architectures actively damp bending oscillations generated by the rocket engine whereas the conventional architecture using a notch filter do not. Tracking performance is identical for all of the architectures tested. The criterion used to asses each controller are summarized in Table 5.1.



# Chapter 6

## Conclusions and Further Developments

### 6.1 Conclusions

Active structural damping on a tactical missile has been investigated. A linear time-invariant model of the flexible missile has been derived using classical flight dynamics coupled with a discretised dynamic Euler Bernoulli beam. To measure the missile flexure, additional sensors - a strain gauge, two gyroscopes and three accelerometers - have been placed at optimal locations on the airframe. Several active damping controllers have been designed and assessed according to multiples criterion. The feedback loop using gyroscopes being preferred for the robustness of these sensors, the low number required and its low control power consumption compared to other architectures.

Active structural damping is feasible on ASTER 30 for the first bending mode. The prior limiting factor being often the slow actuator dynamics. ASTER 30 slenderness makes the bending mode natural frequency low and the fins have a bandwidth large enough to perform active damping. The benefits of such a control are principally vibrations alleviation for the seeker leading to an enhanced tracking of the target.

### 6.2 Further Developments

From this study arises several possible further developments.

Only a limited number of sensors have been added on the airframe. However, some of these sensors are not only sensitive to the first bending mode but also to other bending modes, twisting modes, compression modes and so forth. Augmenting the number of sensors might reinforce confidence in the flexure prediction. Furthermore, the sensors have been placed at peaks of placement indices which might not be the best considering several sensors. For instance the accelerom-

## 6.2. FURTHER DEVELOPMENTS

---

eters must be three and have been placed at the three peaks of the placement index. Once placed, a linear combination of their signal has been done to remove rigid-body components. What can be done is finding the linear combination with respect to the position of each sensor named  $i, j, k$  then compute the placement index for the triple  $(i, j, k)$ . This will give a three dimensional array of placement indices and will find the optimal location for the three sensors.

With the additional sensors, estimation of the missile state can be reinforced using Kalman filtering. Moreover, the array of accelerometers provide information on CG acceleration but also on pitch rate acceleration. The pitch rate acceleration measurement can be used to anticipate on pitching moments.

The three architectures proposed use simple SISO loops and the feedback is generally a static gain. It might be useful to add a band-pass filter centered on the first bending mode frequency to avoid using the fins outside of this band. Indeed the strain gauge feedback and the accelerometers feedback use the fins even at frequencies that do not correspond to the bending oscillation. This would save control energy and diminish interactions between lateral acceleration control and active structural damping.

The study has been focused on bending but it could be enlarged to a 3D model to consider all structural modes such as twisting. The fins are able to generate lateral forces but also twisting moments to damp twisting modes.

Finally an approach can be tracking performance enhancing. The missile can be made more slender and the SPPO can be faster by augmenting the static margin. These two modifications would bring the bending natural frequency and short period frequency closer. A notch filter would be unusable in such a case. Thus, considering the flexible missile as a whole, an optimal controller could be designed to maximize lateral acceleration settling time.

# Appendix A

## Software Development - MATLAB

This appendix gives the preamble of all key m-files that were developed for this thesis. The full source code is available on ??. The units of all parameters are in International System of Units.

### A.1 Flexible Missile Modeling

Several m-files will generate the flexible missile model. These files call each other according to the tree in Figure A.1.

#### A.1.1 Servo-aeroelastic Model Generation

**Filename** `initMissileFullIO.m`

**Author** A. Verhaegen

**Description** This is the main file to generate the servo-aeroelastic model.

**Algorithm** This script will first initialize all structural and flight parameters with the function `loadModelEB`. The rigid-body model, the flexible-body model and the actuators dynamics are derived. Finally these models are fused in a simulink file at extracted to the MATLAB workspace.

**Inputs** None

**Outputs**

`missile` uncertain state-space system of the missile

**Calling** `loadModelEB`, `getRigidBodySS`, `getFlexibleBodySS`

**Called from** `main`

## A.1. FLEXIBLE MISSILE MODELING

---

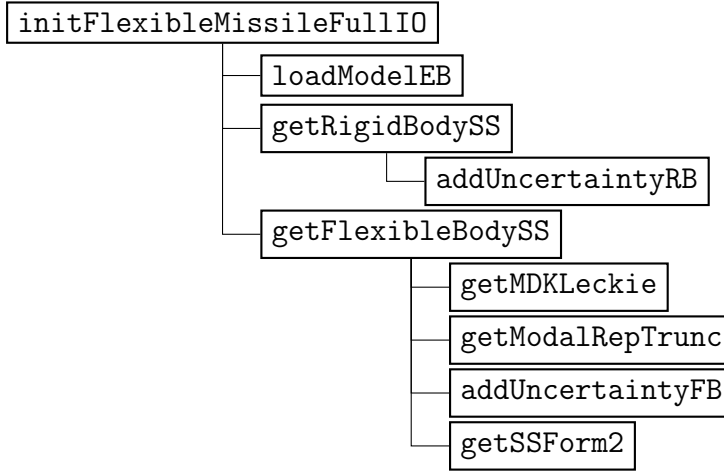


Figure A.1: Calling Tree - Flexible Missile Modeling

### A.1.2 Rigid-body State-space System Generation

**Filename** `getRigidBodySS.m`

**Author** A. Verhaegen

**Description** The function `getRigidBodySS` generates the rigid-body state-space system of a missile.

**Algorithm** The first step is to find the equilibrium. The algorithm defines symbolic variables to create the three equations of motion. An approximate solution of the trim is found and feeds the solver to find a numerical solution for the trim. Once this equilibrium is found the second step is to compute the state-space matrices A,B,C,D with uncertainty on  $T_0$  and  $x_{CG}$ .

#### Inputs

<code>S</code>	reference surface $S_{ref}$
<code>rho</code>	air density $\rho$
<code>CL0</code>	zero AoA lift coefficient $C_{L0}$
<code>CLA</code>	lift coefficient slope $C_{L\alpha}$
<code>CLd</code>	fins lift coefficient slope $C_{L\delta_F}$
<code>xFins</code>	position of the fins from the tail $x_F$
<code>xAE</code>	position of the aerodynamic center $x_{AC}$
<code>Cm0</code>	zero AoA pitching moment coefficient $C_{m0}$
<code>Cma</code>	pitching moment coefficient slope $C_{m\alpha}$
<code>Cmd</code>	fins pitching moment coefficient $C_{m\delta_F}$

$C_{D0}$	zero lift drag coefficient $C_{D0}$
$k_D$	drag coefficient slope $k_D$
$L_{ref}$	reference length $L_{ref}$
$V_0$	trim speed $V_0$
$\gamma_0$	trim flight path $\gamma_0$
$\dot{V}_0$	trim acceleration $\dot{V}_0$
$l$	beam element length $l$
$\mathbf{m}$	vector of nodes masses ( $m_i$ )
$\text{listAcc}$	indices of accelerometers (here 10, 53, 83 and 92)
$J_y$	rotational inertia at CG about y-axis $J_y$
$x_{CG}$	center of gravity position $x_{CG}$

## Outputs

<code>rigidBody</code>	uncertain SS system of the rigid-body
$\alpha_0$	trim AoA $\alpha_0$
$T_0$	trim thrust $T_0$
$\theta_{T0}$	trim thrust orientation $\theta_{T0}$

**Calling** `addUncertaintyRB`

**Called from** `initMissileFullIO`

### A.1.3 Flexible-body Modeling

**Filename** `getFlexibleBodySS.m`

**Author** A. Verhaegen

**Description** The function `getFlexibleBodySS` generates the flexible-body state-space system of a missile.

**Algorithm** The first step is to find the second order structural matrices  $M$ ,  $D$  and  $K$  using `getMDKLeckie`. Then the structural system is formulated under its modal form keeping only a few flexible-body modes with `getModalRepTrunc`. Finally after adding uncertainty on the natural frequencies and the damping ratios, the system is formulated under its state-space form 2 with `getSSForm2`.

## Inputs

$EI$	vector of bending stiffnesses ( $EI_i$ ) <sub>i</sub>
------	---

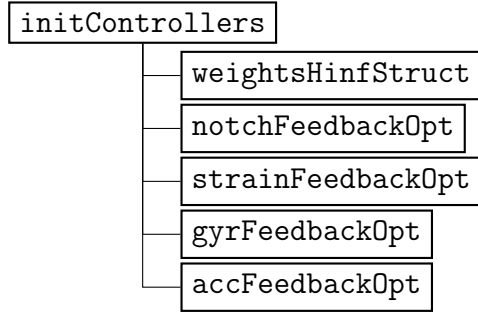


Figure A.2: Calling Tree - Control Design

<code>l</code>	beam element length $l$
<code>dm</code>	vector of nodes masses $(m_i)_i$
<code>Diam</code>	vector of diameters at nodes
<code>m</code>	total mass $m$
<code>xCG</code>	position of CG $x_{CG}$
<code>Jy</code>	rotational inertia $J_y$
<code>n_modes</code>	number of flexible modes kept (5 here)

### Outputs

<code>flexibleBody</code>	uncertain SS system of flexible body
<code>Vm</code>	transformation matrix of modal SS to nodal SS

Calling `getMDKLeckie`, `getModalRepTrunc`, `addUncertaintyFB`, `getSSForm2`

Called from `initMissileFullIO`

## A.2 Control Design

The controllers have been implemented in MATLAB with 6 m-files. They are summarized in Figure ??? by a calling tree.

### A.2.1 Controllers Initialisation

Filename `initControllers.m`

Author A. Verhaegen

**Description** The script `initControllers` creates four different closed-loop system for the flexible missile using the  $H_\infty$  structured tuning.

**Algorithm** After generating the frequency weights with `weightsHinfStruct`, this script will tune the four different latax controllers (“Notch”, “Strain”, “Gyro”, and “Acc”) with the  $H_\infty$  structured tuning in the m-files `notchFeedbackOpt`, `strainFeedbackOpt`, `gyrFeedbackOpt` and `accFeedbackOpt`.

### Inputs

`missile` uncertain state-space system of the missile

### Outputs

<code>notchCL</code>	closed-loop featured with a notch filter
<code>strainCL</code>	closed-loop using the strain measurement
<code>gyrCL</code>	closed-loop using the multiple gyroscopes
<code>accCL</code>	closed-loop using the multiple accelerometers

**Calling** `weightsHinfStruct`, `notchFeedbackOpt`, `strainFeedbackOpt`, `gyrFeedbackOpt`, `accFeedbackOpt`

Called from `main`

## A.2.2 $H_\infty$ Tuning

**Filenames** `notchFeedbackOpt.m`, `strainFeedbackOpt.m`, `gyrFeedbackOpt.m`, `accFeedbackOpt.m`

**Author** A. Verhaegen

**Description** These functions create a closed-loop system respectively for architectures “Notch”, “Strain”, “Gyro” and “Acc”.

**Algorithm** A tunable system is generated using Simulink. This system is weighted with the frequency weights generated with `weightsHinfStruct` and tuned with the  $H_\infty$  structured tuning method.

### Inputs

<code>Win</code>	input weights
<code>Wout</code>	output weights
<code>inputs</code>	input names
<code>outputs</code>	output names

### Outputs

## A.2. CONTROL DESIGN

---

**notchCL** closed-loop featured with a notch filter  
**strainCL** closed-loop using the strain measurement  
**gyrCL** closed-loop using the multiple gyroscopes  
**accCL** closed-loop using the multiple accelerometers

**Calling** None

**Called from** initControllers

# References

- [1] M. R. Waszak and S. Srinathkumar, *Design and experimental validation of a flutter suppression controller for the active flexible wing*, vol. 4381. National Aeronautics and Space Administration, Office of Management, Scientific and Technical Information Program, 1992.
- [2] D. Lesieurte, J. Love, M. Dillenius, and A. Blair Jr, “Recent applications and improvements to the engineering-level aerodynamic prediction software misl3,” in *Proceedings of the 40th AIAA Aerospace Sciences Meeting and Exhibit*, pp. 2002–0275, 2002.
- [3] J. M. Prentis and F. A. Leckie, *Mechanical vibrations: an introduction to matrix methods*. Longmans, 1963.
- [4] W. K. Gawronski, *Dynamics and control of structures: A modal approach*. Springer Science & Business Media, 2004.
- [5] I. Kourakis, *Structural systems and tuned mass dampers of super-tall buildings: case study of Taipei 101*. PhD thesis, Massachusetts Institute of Technology, 2007.
- [6] S. Joshi, P. Maghami, and A. Kelkar, “Dynamic dissipative compensator design for large space structures,” in *AIAA Guidance, Navigation and Control Conference, New Orleans, LA*, pp. 467–477, 1991.
- [7] L. Meirovitch and I. Tuzcu, “Control of flexible aircraft executing time-dependent maneuvers,” *Journal of guidance, control, and dynamics*, vol. 28, no. 6, pp. 1291–1300, 2005.
- [8] D. Alazard and J.-P. Chrétien, “Commande active des structures flexibles: applications spatiales et aéronautiques,” *Notes de cours SUPAERO*, 2000.
- [9] J.-N. Juang, “Applied system identification,” 1994.
- [10] F. W. Nesline Jr and M. L. Nesline, “Phase vs. gain stabilization of structural feedback oscillations in homing missile autopilots,” in *American Control Conference, 1985*, pp. 323–329, IEEE, 1985.

## REFERENCES

---

- [11] S. Laflamme, H. S. Saleem, B. K. Vasan, R. L. Geiger, D. Chen, M. R. Kessler, and K. Rajan, “Soft elastomeric capacitor network for strain sensing over large surfaces,” *Mechatronics, IEEE/ASME Transactions on*, vol. 18, no. 6, pp. 1647–1654, 2013.
- [12] V. Lugo, *Effects of boundary layer ingestion and thrust vectoring in distributed propulsion*. PhD thesis, MSc thesis, Cranfield, UK, 2010.
- [13] R. Knauber, “Thrust misalignments of fixed-nozzle solid rocket motors,” *Journal of spacecraft and rockets*, vol. 33, no. 6, pp. 794–799, 1996.
- [14] G. Selince, “Un nouveau concept de pilotage des missiles application aux sol-air,” tech. rep., Tech. rep., AGARD Lecture Series, 1984.
- [15] V. Viti, R. Neel, and J. A. Schetz, “Detailed flow physics of the supersonic jet interaction flow field,” *Physics of Fluids (1994-present)*, vol. 21, no. 4, p. 046101, 2009.
- [16] J.-P. e. a. Harcaut, “Considérations sur l'aérodynamique pour le pilotage et le guidage des engins tactiques,” 1998.
- [17] J.-L. Boiffier, *The dynamics of flight: the equations*, vol. 1. John Wiley & Sons, 1998.
- [18] E. L. Fleeman, *Tactical missile design*. Amer Inst of Aeronautics &, 2006.
- [19] M. El-Mikkawy and E.-D. Rahmo, “A new recursive algorithm for inverting general tridiagonal and anti-tridiagonal matrices,” *Applied Mathematics and Computation*, vol. 204, no. 1, pp. 368–372, 2008.
- [20] P. Apkarian and D. Noll, “Nonsmooth  $H_\infty$  synthesis,” *Automatic Control, IEEE Transactions on*, vol. 51, no. 1, pp. 71–86, 2006.